The Astrophysical Journal, 976:198 (30pp), 2024 December 1 https://doi.org/10.3847/1538-4357/ad8228

Whole-disk Sampling of Molecular Clouds in M83

Akihiko Hirota[1,2], Jin Koda[3], Fumi Egusa[4], Tsuyoshi Sawada[1,2], Kazushi Sakamoto[5], Mark Heyer[6], Amanda M Lee[3,6], Fumiya Maeda[4,7], Samuel Boissier[8], Daniela Calzetti[6], Bruce G. Elmegreen[9], Nanase Harada[2,10], Luis C. Ho[11,12], Masato I. N. Kobayashi[13], Nario Kuno[14,15], Barry F. Madore[16,17], Sergio Martín[1,18], Jennifer Donovan Meyer[19], Kazuyuki Muraoka[20], and Yoshimasa Watanabe[21]

[1] Joint ALMA Observatory, Alonso de Córdova 3107, Vitacura, Santiago 763-0355, Chile; Akihiko.Hirota@alma.cl
[2] National Astronomical Observatory of Japan, 2-21-1 Osawa, Mitaka, Tokyo 181-8588, Japan
[3] Department of Physics and Astronomy, Stony Brook University, Stony Brook, NY 11794-3800, USA
[4] Institute of Astronomy, Graduate School of Science, The University of Tokyo, 2-21-1 Osawa, Mitaka, Tokyo 181-0015, Japan
[5] Academia Sinica, Institute of Astronomy and Astrophysics, Taipei 10617, Taiwan
[6] Department of Astronomy, University of Massachusetts Amherst, 710 North Pleasant Street, Amherst, MA 01003, USA
[7] Research Center for Physics and Mathematics, Osaka Electro-Communication University, 18-8 Hatsucho, Neyagawa, 572-8530, Osaka, Japan
[8] Aix Marseille Univ., CNRS, CNES, Laboratoire d'Astrophysique de Marseille, Marseille, France
[9] Katonah, NY 10536, USA
[10] Department of Astronomy, School of Science, Graduate University for Advanced Studies (SOKENDAI), 2-21-1 Osawa, Mitaka, Tokyo, 181-1855, Japan
[11] Kavli Institute for Astronomy and Astrophysics, Peking University, Beijing 100871, People's Republic of China
[12] Department of Astronomy, School of Physics, Peking University, Beijing 100871, People's Republic of China
[13] Universität zu Köln, I. Physikalisches Institut, Zülpicher Str. 77, D-50937 Köln, Germany
[14] Division of Physics, Faculty of Pure and Applied Sciences, University of Tsukuba, 1-1-1 Tennodai, Tsukuba, Ibaraki 305-8571, Japan
[15] Tomonaga Center for the History of the Universe, University of Tsukuba, 1-1-1 Tennodai, Tsukuba, Ibaraki 305-8571, Japan
[16] The Observatories, Carnegie Institution for Science, 813 Santa Barbara Street, Pasadena, CA 91101, USA
[17] Department of Astronomy and Astrophysics, University of Chicago, 5640 S. Ellis Ave., Chicago, IL 60637, USA
[18] European Southern Observatory, Alonso de Córdova, 3107, Vitacura, Santiago 763-0355, Chile
[19] National Radio Astronomy Observatory, 520 Edgemont Road, Charlottesville, VA 22903, USA
[20] Department of Physics, Graduate School of Science, Osaka Metropolitan University, 1-1 Gakuen-cho, Naka-ku, Sakai, Osaka 599-8531, Japan
[21] Materials Science and Engineering, College of Engineering, Shibaura Institute of Technology, 3-7-5 Toyosu, Koto-ku, Tokyo 135-8548, Japan

Received 2024 February 16; revised 2024 September 16; accepted 2024 September 26; published 2024 November 22

Abstract

We present a catalog of clouds identified from the ^{12}CO (1–0) data of M83, which was observed using the Atacama Large Millimeter/submillimeter Array with a spatial resolution of ∼46 pc and a mass sensitivity of $\sim 10^4\,M_\odot$ (3σ). The almost full-disk coverage and high sensitivity of the data allowed us to sample 5724 molecular clouds with a median mass of $\sim 1.9 \times 10^5\,M_\odot$, which is comparable to the most frequently sampled mass of giant molecular clouds by surveys in the Milky Way (MW). About 60% of the total CO luminosity in M83's disk arises from clouds more massive than $10^6\,M_\odot$. Such massive clouds comprise 16% of the total clouds in number and tend to concentrate toward the arm, bar, and center, while smaller clouds are more prevalent in interarm regions. Most $>10^6\,M_\odot$ clouds have peak brightness temperatures $T_{\rm peak}$ above 2 K with the current resolution. Comparing the observed cloud properties with the scaling relations determined by P. M. Solomon et al. (1987, hereafter S87), $T_{\rm peak} > 2$ K clouds follow the relations, but $T_{\rm peak} < 2$ K clouds, which are dominant in number, deviate significantly. Without considering the effect of beam dilution, the deviations would suggest modestly high virial parameters (median $\alpha_{\rm vir} \sim 2.7$) and low surface mass densities (median $\Sigma \sim 22\,M_\odot\,{\rm pc}^{-2}$) for the entire cloud samples, which are similar to values found for the MW clouds by T. S. Rice et al. (2016) and M.-A Miville-Deschênes et al. (2017). However, once beam dilution is taken into account, the observed $\alpha_{\rm vir}$ and Σ for a majority of the clouds (mostly $T_{\rm peak} <2$ K) can be potentially explained with intrinsic Σ of $\sim 100\,M_\odot\,{\rm pc}^{-2}$ and $\alpha_{\rm vir}$ of ∼1, which are similar to the clouds of S87.

Unified Astronomy Thesaurus concepts: Giant molecular clouds (653); Spiral galaxies (1560); Millimeter astronomy (1061); CO line emission (262); Interstellar medium (847)

Materials only available in the online version of record: machine-readable table

1. Introduction

Molecular gas is directly associated with star formation in the nearby Universe. The bulk of H_2 mass resides in giant molecular clouds (GMCs), which are concentrations of molecular gas with a temperature of around 10 K, diameter of 10–100 pc, and mass of $10^{5-6}\,M_\odot$ (e.g., D. B. Sanders et al. 1985).[22] The efficiency of star formation in GMCs is determined by the complex interplay among many processes, including self-gravity, turbulence, stellar feedback, and magnetic fields, although the exact balance is still not certain. Characterizing GMCs' properties and their relations is vital in reaching a coherent understanding of star formation in galaxies.

The conventional view of GMCs was mainly established by the early CO studies of Galactic molecular clouds about four decades ago. At that time, GMCs were mainly identified as discrete emission features in the Galactic plane (e.g., D. B. Sanders et al. 1985). The early studies empirically established the scaling relations of cloud properties (R. B. Larson 1981; P. M. Solomon et al. 1987, hereafter S87) and also found a power-law GMC mass function (D. B. Sanders et al. 1985; N. Z. Scoville & D. B. Sanders 1987). In particular, the three relations determined by S87, namely, the scaling relations of line width and size $\Delta V \propto S^{\sim 0.5}$, virial mass and CO luminosity $M_{\rm vir} \propto L_{\rm CO}^{\sim 0.8}$, and volume density and size $\rho \propto S^{-1}$, are often used as a benchmark in most subsequent studies of GMCs. Assuming that clouds are approximately in virial equilibrium, the near-linear $M_{\rm vir}$–$L_{\rm CO}$ relation (second relation) yields a constant CO-to-H_2 conversion factor of $X_{\rm CO} \sim 2 \times 10^{20}$ cm $^{-2}$ (K km s $^{-1}$) $^{-1}$ for a typical Galactic GMC, which agrees with the "standard" conversion factor often adopted today in metal-rich environments (see A. D. Bolatto et al. 2013). Using the constant conversion factor, the third relation suggests that the surface mass densities of GMCs are nearly constant around 200 $M_\odot\,{\rm pc}^{-2}$, which is often taken as a typical surface density in GMCs.

Subsequent studies explored the cloud properties in diverse environments, including the outer Galaxy (M. H. Heyer et al. 2001), Galactic center (GC; T. Oka et al. 2001), and extragalactic environments (G. Engargiola et al. 2003; E. Rosolowsky & L. Blitz 2005; A. D. Bolatto et al. 2008; J. Donovan Meyer et al. 2013; D. Colombo et al. 2014; P. Freeman et al. 2017; A. Hirota et al. 2018; F. Maeda et al. 2020; E. Rosolowsky et al. 2021; K. Muraoka et al. 2023). Several studies revisited GMCs also in the inner Galactic disk with new ^{13}CO survey data (J. Roman-Duval et al. 2010) and with a more complete coverage albeit at lower spatial resolution (T. S. Rice et al. 2016, hereafter R16; M.-A. Miville-Deschênes et al. 2017, hereafter M17). Some confirmed the S87 relations in the inner Galactic disk (J. Roman-Duval et al. 2010) and in external galaxies (A. D. Bolatto et al. 2008), but others found deviations in two aspects.

First, despite the near-virial balance suggested for S87's clouds, recent studies report a variety of dynamical stability in clouds. In the GC (T. Oka et al. 2001) and outer Galactic disk (M. Heyer et al. 2009), many clouds appear unbound if the $X_{\rm CO}$ in the inner disk is applied. These analyses often adopt the virial parameter (F. Bertoldi & C. F. McKee 1992), the ratio of kinetic to gravitational energies of clouds, and find $\alpha_{\rm vir} \gg 1$–2 for the unbound clouds. Even in the inner Galactic disk, M17 suggests that only 15% of the clouds might be bound, although bound clouds account for 40% of the total molecular gas mass. In addition, recent extragalactic studies found a large scatter in $\alpha_{\rm vir}$ with an average value of ∼2 in disk regions (J. Sun et al. 2020b; E. Rosolowsky et al. 2021), which suggested a modestly gravitationally bound state, but not in the virial equilibrium. N. J. Evans et al. (2021) found that, in general, only 20%–40% of the cloud masses are bound by compiling cloud catalogs both in Galactic and extragalactic environments.

Second, the near-constant Σ of around 200 $M_\odot\,{\rm pc}^{-2}$ is also revisited by recent studies. Σ appears to show considerable variations, with a low median value of a few × 10 $M_\odot\,{\rm pc}^{-2}$ in the recent Galactic plane study (M17) and in the outer Galactic disk survey (M. H. Heyer et al. 2001) but high Σ, reaching up to 1000 $M_\odot\,{\rm pc}^{-2}$ or higher, in GCs (T. Oka et al. 2001; A. K. Leroy et al. 2015).

The large variations in $\alpha_{\rm vir}$ and Σ seen in recent studies, along with predictions from numerical simulations (C. L. Dobbs & J. E. Pringle 2013; R. J. Smith et al. 2020), potentially require a refinement of the view of GMCs: GMCs could be modestly bound by self-gravity and are relatively transient objects, which might be prone to be dispersed by large-scale shear motions and stellar feedback (see C. L. Dobbs et al. 2011; M. Chevance et al. 2023).

Extragalactic studies of molecular clouds provided essential contributions to this refinement of the view of molecular clouds. However, most extragalactic studies were limited by low spatial resolutions of >50–100 pc (i.e., larger than most of the Galactic GMC diameters; D. Colombo et al. 2014; A. Hirota et al. 2018), even in the recent PHANGS survey (E. Rosolowsky et al. 2021). These extragalactic "disk" surveys mostly achieved mass completeness limits of around $10^6\,M_\odot$ or more, while most of the inner Galactic disk surveys were made the completeness limit of 1–3 × $10^5\,M_\odot$ (e.g., D. B. Sanders et al. 1985; N. Z. Scoville & D. B. Sanders 1987; S87; J. Roman-Duval et al. 2010; R16; M17). To build a more accurate and comprehensive view, we need a higher sensitivity and resolution to characterize the cloud properties and distribution over a wide range of cloud masses and to elucidate their environmental dependence.

Recently, the full extent of the molecular disk of the nearby galaxy M83 was observed in ^{12}CO (1–0) using the Atacama Large Millimeter/submillimeter Array (ALMA; J. Koda et al. 2023). The mass sensitivity, ∼$10^4\,M_\odot$, is unprecedented for such a full-disk mapping of substantial spiral galaxies. M83 closely resembles the Milky Way (MW) in morphology (including the bar, spiral arms, and even interarm structures), as well as in its size, gas and stellar masses, and near solar metallicity (J. Koda et al. 2023). This study identifies molecular clouds from the ^{12}CO data to examine the cloud properties, distributions, scaling relations, and mass distributions.

We organize this paper as follows. In Section 2, we describe the data and procedure to catalog molecular clouds. In Section 3, we present their properties, scaling relations, and spatial distribution. We examine the cloud mass function in Section 4 and estimate the vertical cloud-to-cloud velocity dispersions in Section 5. In Section 6, we discuss the impact of beam dilution (beam filling factor) on the cloud parameters, in particular on $\alpha_{\rm vir}$ and Σ, and discuss its implications to our view of molecular clouds. In Section 7, we present the conclusions.

---

[22] The definition of GMC slightly varies from literature to literature, but D. B. Sanders et al. (1985) defined molecular clouds with a diameter larger than 22 pc and mass above $10^5\,M_\odot$ as GMCs. Nearby Galactic clouds with a mass of a few $10^4\,M_\odot$ are also often referred to as GMCs (e.g., C. J. Lada et al. 2010).

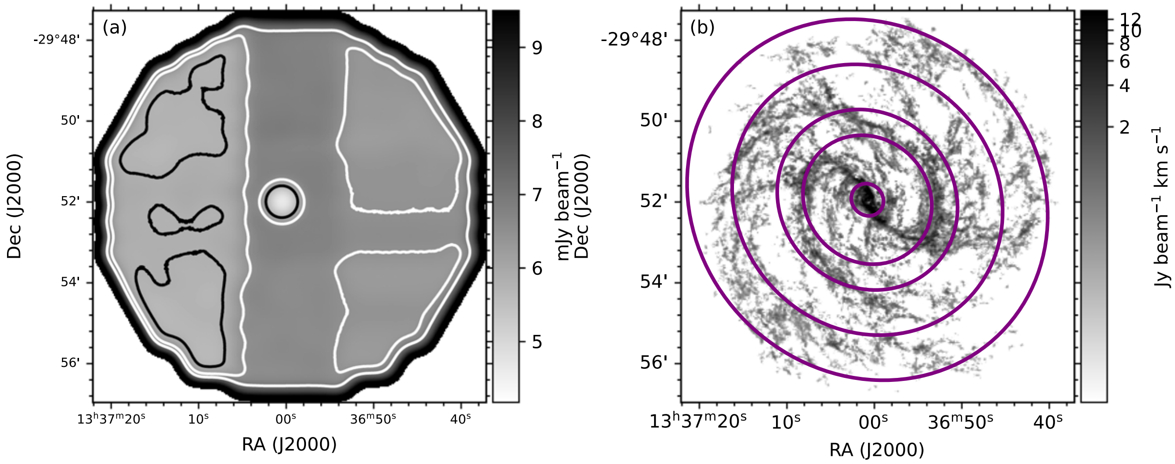

Figure 1. (a) rms noise map of the ^{12}CO (1–0) used here. The white lines indicate the rms map with the contour levels of 0.9σ and 1σ, where 1σ is the global median of the rms noise of 6.5 mJy beam^{-1} ($\sim$0.17 K), and the black line indicates the level of 1.1σ. (b) Integrated intensity map of ^{12}CO (1–) data used here. The cyan lines indicate the galactocentric radii of 25″ ($\sim$0.55 kpc), 100″ ($\sim$2.2 kpc), 140″ ($\sim$3.1 kpc), 210″ ($\sim$4.6 kpc), and 280″ ($\sim$6.1 kpc), respectively.

2. Molecular Cloud Identification

2.1. Data

We used the ^{12}CO ($J = 1$–0) mapping data of M83 observed with ALMA (project code 2017.1.00079.S; J. Koda et al. 2023). The observations used the main 12 m array and Atacama Compact Array, i.e., the 7 m short-baseline interferometric array and the Total-Power (TP) single-dish array, to recover the flux. The interferometric and single-dish data were calibrated separately. The calibration procedure is described in J. Koda et al. (2023). The calibrated TP array data were converted into interferometric visibilities using the TP2VIS software (J. Koda et al. 2019). Then, the 12 m, 7 m, and TP array visibilities were inverted onto the image plane and jointly deconvolved using the MIRIAD software package (R. J. Sault et al. 1995). We refer the readers to J. Koda et al. (2023) for further details on the data processing.

Three data cubes were prepared in J. Koda et al. (2023) with velocity resolutions of 1, 2, and 5 km s^{-1}, respectively. We here adopt the one with 1 km s^{-1} resolution. The restoring beam of the original data is a Gaussian with major and minor axes of $2\farcs09 \times 1\farcs68$ in FWHM, which corresponds to 45.6 pc $\times$ 36.7 pc at the assumed distance of M83 (4.5 Mpc; F. Thim et al. 2003). To avoid complexities associated with the noncircular beam, we smoothed the original data cube in spatial directions to achieve a circular beam with an FWHM size of $2\farcs1$, corresponding to $\sim$46 pc.

Figure 1(a) shows the two-dimensional map of the rms noise level. We adopted the following procedure to obtain a noise-free estimate of the noise distribution. First, we used MIRIAD's "mossen" command to generate a two-dimensional noise distribution expected from the integration time and system noise temperature assigned to visibilities. Next, the "expected" noise map produced by mossen was compared with the "measured" noise map, which we made by measuring rms noise along the velocity axis at each position in the data cube. The comparison confirmed that both maps are consistent regarding the relative spatial variation within each map but are discrepant in the absolute scaling by a few tens of percent. Therefore, as the final step, we scaled the "expected" map so that the median noise level matches that of the "measured" noise map. The median noise level across the observed field is 6.5 mJy per beam.

2.2. Cloud Identification

We here describe our procedures to identify molecular clouds in the ^{12}CO (1–0) data cube.

As a preparatory step, we constructed a signal mask to isolate voxels with significant detection. The mask was created by first identifying a set of regions that consist of voxels with signal-to-noise ratio (SNR) $\geqslant 4$, then discarding small regions whose spatial extents are less than 0.6 times the beam area or whose emissions are confined in a single 1 km s^{-1} channel along the velocity axis, and finally expanding the remaining regions to include the morphologically connected surrounding voxels with SNR $\geqslant 2$.

The masked data cube was decomposed into a set of independent closed surfaces using the `astrodendro` software package.[23] Although `astrodendro` identifies hierarchically nested sets of structures, we adopted only the structures at the finest spatial scales, commonly referred to as *leaves*. This is because the utilized spatial resolution, $\sim$46 pc at FWHM, is only a factor of 2 smaller than the typical height of the thin molecular gas disk (e.g., about 100 pc in FWHM for the MW disk; see M. Heyer & T. M. Dame 2015). As long as the disk height is similar between M83 and Milky Way and the size of the largest cloud is limited by the disk height, examining structures larger than individual leaves is unnecessary. Parameters for the cloud decomposition algorithm are configured such that only voxels with SNR > 2 are included in the analysis, and *leaf* candidates with SNR contrasts between their peak and edge-level <2 are discarded. In addition, to avoid picking up noise fluctuations as clouds, we discarded small leaves with the number of voxels less than $A_{\rm beam}/A_{\rm voxel}$, where $A_{\rm beam}$ and $A_{\rm voxel}$ are the area of the beam and a voxel.

The identified leaves generally trace the small regions around the peaks of molecular clouds, especially in crowded areas, because by nature of the algorithm, the leaves are defined such that they do not overlap each other. The `astrodendro` decomposition left about 80% of the CO emission unassigned to any leaves. The unassigned voxels to any seed structures are further segmented with the watershed algorithm, using the `scikit-image` software package (S. van der Walt et al. 2014).

---

[23] http://www.dendrograms.org

A total of 5724 leaves, which are expanded by the watershed segmentation, are accepted as molecular clouds. About 91% of the total CO luminosity within the mapped area was sampled as molecular clouds, as we will see later in Section 2.6.

2.3. Derivation of Cloud Properties

The physical properties of the identified clouds are calculated in a way similar to the one adopted in A. Hirota et al. (2018). A brief description is provided here.

2.3.1. Measured Properties

Each cloud's centroid position and velocity are measured as the intensity-weighted first moments. We record the maximum brightness temperature within the cloud as peak temperature $T_{\rm peak}$. The size parameters in two dimensions and velocity dispersion of each cloud are calculated as second moments and then extrapolated to the 0 K level with the procedure of E. Rosolowsky & A. Leroy (2006). Hereafter, we denote the extrapolated moment values as $\sigma_{\rm x,r}$, $\sigma_{\rm y,r}$, and $\sigma_{\rm v,r}$, where $\sigma_{\rm x,r} > \sigma_{\rm y,r}$. The CO luminosity for each cloud ($L_{\rm CO}$) is derived as a summation in each cloud boundary and extrapolated to 0 K level. We estimated the uncertainty in $\sigma_{\rm x,r}$, $\sigma_{\rm y,r}$, and $\sigma_{\rm v,r}$ by performing a bootstrap error estimation with 1000 trials.

2.3.2. Derived Properties

We derived the physical parameters of the clouds from the directly measured parameters presented above.

Effective radius. The effective radius of the cloud ($R_{\rm eff}$) is derived as

$$R_{\rm eff} = \frac{3.4}{\sqrt{\pi}}\sqrt{\sigma_{\rm x}\sigma_{\rm y}} \tag{1}$$

where $3.4/\sqrt{\pi}$ ($\sim$1.91) is an empirical factor that is determined by S87, and $\sigma_{\rm x}$ and $\sigma_{\rm y}$ are the deconvolved cloud sizes defined below. We note that, although this definition of $R_{\rm eff}$ is long used as common custom, some of the recent studies also define the cloud radius as half width half maximum, $R_{\rm HWHM} = 1.18\sqrt{\sigma_{\rm x}\sigma_{\rm y}}$ (E. Rosolowsky et al. 2021), and thus care is needed when comparing values.

The deconvolved sizes are obtained by subtracting the beam size in quadrature from the extrapolated cloud sizes of $\sigma_{\rm x,r}$ and $\sigma_{\rm y,r}$ as

$$\sigma_{\rm x} = \sqrt{\sigma_{\rm x,r}^2 - \theta_{\rm b}^2/(8\log 2)}, \tag{2}$$

$$\sigma_{\rm y} = \sqrt{\sigma_{\rm y,r}^2 - \theta_{\rm b}^2/(8\log 2)}, \tag{3}$$

where $\theta_{\rm b}$ is the FWHM resolution of the data ($2\overset{\prime\prime}{.}1$, $\sim$46 pc). Out of the 5724 clouds identified, 225 clouds have $\sigma_{\rm y,r}$ smaller than $\theta_{\rm b}/\sqrt{8\log 2}$. We marked them as "deconvolution-failed clouds" and assigned $\sigma_{\rm x,r}$ and $\sigma_{\rm y,r}$ as the upper limits on $\sigma_{\rm x}$ and $\sigma_{\rm y}$, respectively.

Velocity dispersion. The velocity dispersion of the cloud ($\sigma_{\rm v}$) is calculated by subtracting the instrumental velocity resolution from the extrapolated $\sigma_{\rm v,r}$ as

$$\sigma_{\rm v} = \sqrt{\sigma_{\rm v,r}^2 - (\Delta V_{\rm ch}/\sqrt{12})^2}, \tag{4}$$

where $\Delta V_{\rm ch}$ is the channel width of the data (1 km s^{-1}). The factor of $1/\sqrt{12}$ is the ratio of the second moment to the width for a boxcar profile.

Molecular gas mass. The molecular gas mass for each GMC ($M_{\rm cl}$) is calculated from $L_{\rm CO}$ by applying a CO-to-H$_2$ conversion factor of 2.0×10^{20} cm^{-2} (K km s^{-1})$^{-1}$ in combination with a correction factor of 1.36 that accounts for the contribution of Helium and other elements. (A. D. Bolatto et al. 2013):

$$\left(\frac{M_{\rm cl}}{M_\odot}\right) = \left(\frac{\alpha_{\rm CO}}{4.4 M_\odot/(\text{K km s}^{-1}\text{pc}^2)}\right)\left(\frac{L_{\rm CO}}{\text{K km s}^{-1}\text{pc}^2}\right), \tag{5}$$

where $\alpha_{\rm CO}$ is the mass-to-luminosity ratio. The $\alpha_{\rm CO}$ of 4.4 $M_\odot$ (K km s^{-1}pc^2) is often regarded as the "standard" value for GMCs in metal-rich environments, such as in M83's inner disk (F. Bresolin et al. 2016), and thus, the use of the "standard" conversion factor is justified as the first order approximation (A. D. Bolatto et al. 2013). We note that, however, A. M. Lee et al. (2024) suggested a kiloparsec-scale radial variation in $\alpha_{\rm CO}$, which is a factor of a few increase from the galactocentric radius of $\sim$2 kpc to $\sim$6 kpc. A. M. Lee et al. (2024) noted that the radial gradient of metallicity in the disk of M83 is insufficient to explain the observed variation in $\alpha_{\rm CO}$ as it can only produce a factor of $\sim$1.2 to $\sim$1.3 variations in $\alpha_{\rm CO}$ over the corresponding radial range by adopting the metallicity measurement of F. Bresolin et al. (2016) and the metallicity-dependent descriptions of $\alpha_{\rm CO}$ of C. D. Wilson (1995) and N. Arimoto et al. (1996). They suggested that the weak dependence of $\alpha_{\rm CO}$ on $L_{\rm CO}$, expected for gravitationally bound clouds with constant surface densities (S87; A. D. Bolatto et al. 2013), combined with the radial variation in the cloud mass function can provide a relative variation in $\alpha_{\rm CO}$ comparable to the observed variation.

Surface density. Average gas surface density of a cloud (Σ) is calculated as

$$\Sigma = M_{\rm cl}/(\pi R_{\rm eff}^2). \tag{6}$$

Virial mass. Following F. Bertoldi & C. F. McKee (1992), the virial mass is calculated as

$$M_{\rm vir} = \frac{1}{a_1}\frac{5R\sigma_{\rm v}^2}{G}, \tag{7}$$

where G is the gravitational constant, and a_1 is a geometrical factor that is $(1 - k/3)/(1 - 2k/5)$ for a power-law density distribution of $\rho(r) \propto r^{-k}$. We assumed k to be 1, following S87. Examinations of the nearby Galactic clouds suggest slightly larger values of k (e.g., 1.3–1.4; J. Kauffmann et al. 2010; M. Lombardi et al. 2010). As the dependence of the geometrical factor a_1 on k is small, we adopt $k = 1$ to keep consistency with previous studies.

Virial parameter. The virial parameter $\alpha_{\rm vir}$ is a ratio between the virial mass and gas mass and is a measure of the ratio of the kinetic to gravitational energy (F. Bertoldi & C. F. McKee 1992):

$$\alpha_{\rm vir} \equiv M_{\rm vir}/M_{\rm cl}. \tag{8}$$

Ignoring the support from external pressure and magnetic fields, a state of simple virial equilibrium is achieved when $\alpha_{\rm vir}$ is 1 or a factor of few around 1, considering the uncertainty in the assumed density profile and CO-to-H$_2$ conversion factor. Clouds are loosely bound when the equipartition between the kinetic and gravitational energy is achieved with $\alpha_{\rm vir} \sim 2$

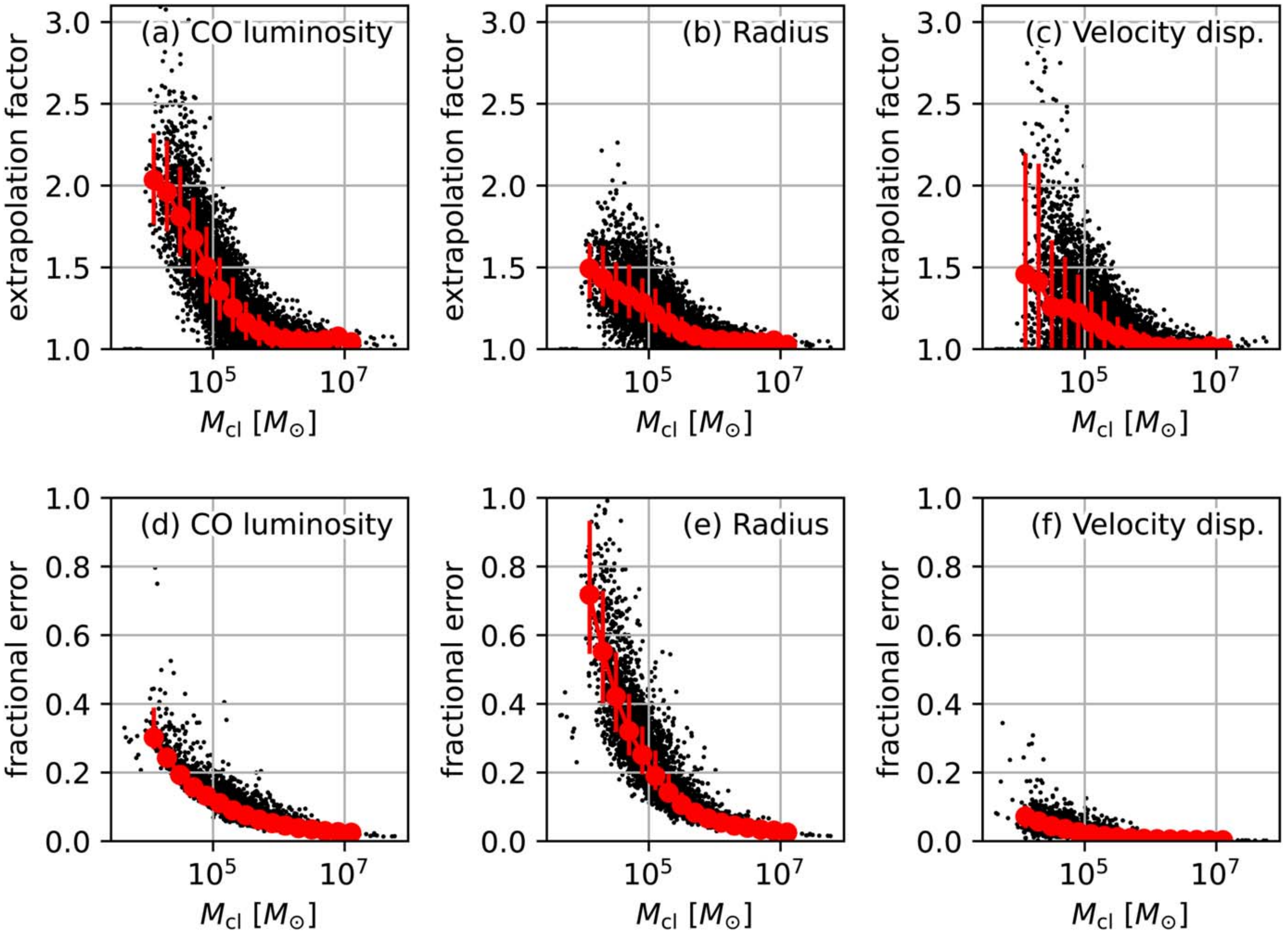

Figure 2. (a)–(c) Ratio of the extrapolated to unextrapolated values for $L_{\rm CO}$, $R_{\rm eff}$, and $\sigma_{\rm v}$, respectively, are shown as a function of the cloud mass. The red markers and error bars indicate the median and 16th-to-84th percentile ranges of each quantity at the binning masses. (d)–(f) Same as (a)–(c), but for fractional uncertainty for each quantity in (a)–(c) as a function of the cloud mass.

(R. B. Larson 1981; J. Ballesteros-Paredes et al. 2011). We note a general caveat on interpreting $\alpha_{\rm vir}$. As isolated clouds with simple geometry and density distribution are assumed, the observationally derived $\alpha_{\rm vir}$ has a limitation in characterizing the dynamical status of molecular clouds. Numerical simulations suggest that clouds could be either more bound (J. Ballesteros-Paredes et al. 2018; L. Ramírez-Galeano et al. 2022) or more unbound (S. A. Mao et al. 2020) than what the face value of $\alpha_{\rm vir}$ would suggest.

2.4. Extrapolation Factors and Measurement Uncertainties

The extrapolation to 0 K emission level made to basic cloud parameters (Section 2.3.1) is needed to correct for the underestimation of the parameters that would arise if the parameters are determined at a higher edge level (E. Rosolowsky & A. Leroy 2006). However, the extrapolation result becomes less reliable for a cloud that requires a higher correction factor. Thus, we expect clouds with higher correction factors to have higher measurement uncertainties assigned by the bootstrap estimate. We show the amount of correction and measurement uncertainties to the clouds here.

Figures 2(a)–(c) show the correction factor of the extrapolation, which is the ratio between the extrapolated to unextrapolated values for CO luminosity, radius, and the velocity dispersion of the clouds, plotted as functions of the cloud mass. The correction factors tend to increase toward lower cloud masses. At a mass of $2 \times 10^5\,M_\odot$, the medians of the correction factors are about 1.25, 1.16, and 1.12 for luminosity, radius, and velocity dispersion, respectively, and are modest. At the lowest-mass bin of $2 \times 10^4\,M_\odot$, the median factors are 1.96, 1.43, and 1.41, respectively.

Figures 2(d)–(f) show the measurement errors in CO luminosity, radius, and velocity dispersion expressed in the fractional form. Uncertainties in these basic three quantities are transferred to other advanced quantities following uncertainty propagation.

2.5. GMC Catalog

Table 1 lists the first several entries of the compiled catalog. The complete list shall be available as an electronic table. Each line in the catalog reports the parameter of an identified cloud, including the centroid position and receding velocity, $R_{\rm eff}$, the axial ratio ($\sigma_{\rm y}/\sigma_{\rm x}$) and position angle, $\sigma_{\rm v}$, $L_{\rm CO}$, $M_{\rm vir}$, and the binary flag that indicates whether the deconvolution failed for the cloud or not.

2.6. Fraction of CO Luminosity Sampled as GMC

Table 2 lists the total CO luminosity $L_{\rm CO}$ along with the fractional CO luminosities included within the signal mask

Table 1
Catalog of Clouds in M83

R.A. (1)	Decl. (2)	$V_{\rm LSR}$ (km s^{-1}) (3)	$T_{\rm peak}$ (K) (4)	$R_{\rm eff}$ (pc) (5)	σ_y/σ_x (6)	P.A. (deg) (7)	σ_v (km s^{-1}) (8)	$L_{\rm CO}$ (10^4 K km s^{-1} pc^2) (9)	$M_{\rm vir}$ (10^5 $M_\odot$) (10)	Deconv. Flag (11)
13:37:00.310	−29:51:52.41	542.6	17.39	66	0.51	−157	13	640	110	0
13:37:00.755	−29:52:07.75	510.9	16.68	86	0.78	−122	22	1300	420	0
13:37:00.400	−29:51:50.07	514.9	15.74	58	0.65	−149	7.0	320	30	0
13:37:00.435	−29:51:49.76	489.4	13.66	47	0.83	−167	9.3	300	43	0
13:37:00.762	−29:51:43.94	499.3	13.43	94	0.79	−150	16	1200	240	0
13:37:00.610	−29:51:54.27	481.9	12.91	57	0.52	−59	11	370	75	0
13:37:00.334	−29:51:58.93	564.5	12.32	74	0.68	−182	11	240	91	0

Note. Parameters of the identified cloud. Column (1): R.A. Column (2): decl. Column (3): centroid velocity. Column (4): peak brightness temperature. Column (5): effective radius. Column (6): ratio between the minor and major axes' lengths. Column (7): position angle of the major axis of the cloud, measured from the north. Column (8): velocity dispersion. Column (9): CO (1–0) luminosity. Column (10): virial mass. Column (11): flag indicating whether the deconvolution was successfully made (=0) or not (=1).

(This table is available in its entirety in machine-readable form in the online article.)

Table 2
Global CO Luminosity and GMC Mass in M83

Radial Range (kpc) (1)	$L_{\rm CO}$ (10^7 K km s^{-1} pc^2) (2)	$f^{\rm mask}$ (3)	$f^{\rm cl}$ (4)
All	82.7 ± 0.17	0.85	0.93 ± 0.05
0.00–0.55	12.6 ± 0.01	0.98	1.04 ± 0.03
0.55–2.18	18.6 ± 0.05	0.90	1.00 ± 0.05
2.18–3.05	17.7 ± 0.05	0.90	0.97 ± 0.05
3.05–4.58	17.3 ± 0.08	0.79	0.86 ± 0.05
4.58–6.11	14.4 ± 0.10	0.73	0.83 ± 0.06

Note. Column (1): radial range; locations of the boundary radii are shown in Figure 1(b). Column (2): CO luminosity. Column (3): fractional CO luminosity within the signal mask. Column (4): fractional CO luminosity sampled as clouds.

($f_{\rm mask}$) and sampled as molecular clouds ($f_{\rm cl}$). To indicate their overall radial trends, we list the values for five radial bins separated at galact-centric radii shown in Figure 1(b). The $f_{\rm mask}$ is highest in the innermost radial bin (∼97%) and decreases with increasing galact-centric radius to ∼68% in the outermost radial bin. This radially declining trend suggests that the contribution of lower-mass clouds to total mass becomes increasingly significant at larger galact-centric radii.

The extrapolation process recovers part of the emission removed by applying the signal mask. Reflecting this, $f_{\rm cl}$ is higher than $f_{\rm mask}$ in all the radii. However, in the central 550 pc, $f_{\rm cl}$ slightly exceeds 1 (1.04 ± 0.03), which indicates that the flux extrapolation is overcorrecting the cloud flux by a few percent. A radially declining trend of $f_{\rm cl}$ exists. It is nearly 100% within the central 3.1 kpc. It decreases radially down to ∼80% in the outermost radial bin, suggesting an increased fraction of clouds below the detection limit.

We estimate the detectable minimum cloud mass that is based on the observation and segmentation parameters. The cloud identification process (in Section 2.2) sets the peak SNR threshold as 4, which corresponds to a brightness temperature limit of ∼0.5 K. Assuming that the minimum cloud has an area equivalent to the beam area and that the cloud emission has a Gaussian profile with σ_v of 2 km s^{-1} and $T_{\rm peak}$ of 0.5 K, the mass of the cloud is $\alpha_{\rm CO}(2\pi)^{1/2}T_{\rm peak}\,\sigma_v\,(1.13\,\theta_b^2)$. With the assumed $\alpha_{\rm CO}$ of 4.4 $M_\odot$ / (K km s^{-1} pc^2) and θ_b of 46 pc, the expected minimum cloud mass would be $\sim 3 \times 10^4\,M_\odot$. We note that this value is for clouds that exist in isolated areas, and the mass completeness limit is elevated in crowded regions.

3. Results

3.1. Distribution of Cloud Properties

Figure 3 shows the distributions of the molecular cloud properties, including mass ($M_{\rm cl}$), peak temperature ($T_{\rm peak}$), velocity dispersion σ_v, radius ($R_{\rm eff}$), surface density (Σ), and virial parameter ($\alpha_{\rm vir}$). Each cloud property is displayed in unweighted and mass-weighted histograms. The top panels for each parameter show unweighted histograms for all the clouds (black line), clouds with masses above 10^6 $M_\odot$ (blue line), those with masses between 10^5 and 10^6 $M_\odot$ (green line), and those for which the deconvolution failed to determine their sizes (dashed line). The medians with 16th-to-84th percentile ranges for the first three categories are displayed using markers and horizontal error bars. The bottom panels for each parameter display the mass-weighted histogram with the mass-weighted medians and horizontal bars for the 16th and 84th percentiles. Table 3 lists the summary of the measurements.

3.1.1. Mass

Figure 3(a) shows the distribution of $M_{\rm cl}$. The unweighted median of $M_{\rm cl}$ for the entire sample is 1.9×10^5 $M_\odot$, which is close to the median cloud mass found in the inner Galactic disk found by existing surveys (e.g., $\sim 8 \times 10^4$ $M_\odot$, M17) and also close to the lower end of a conventional definition of GMC mass range (around 10^5 $M_\odot$, e.g., D. B. Sanders et al. 1985). The unweighted 16 percentile of cloud mass is 5×10^4 $M_\odot$ and agrees with the roughly expected minimum cloud mass of $\sim 3 \times 10^4$ $M_\odot$ (Section 2.6). This suggests that the present catalog samples the full range of GMCs in M83's disk, at least when they are well isolated in space or velocity.

Figure 3(a), when the top and bottom panels are compared, indicates that massive GMCs are a minority in number but occupy the dominant fraction of the total CO luminosity. About 50% of the molecular gas mass (or total CO luminosity) resides

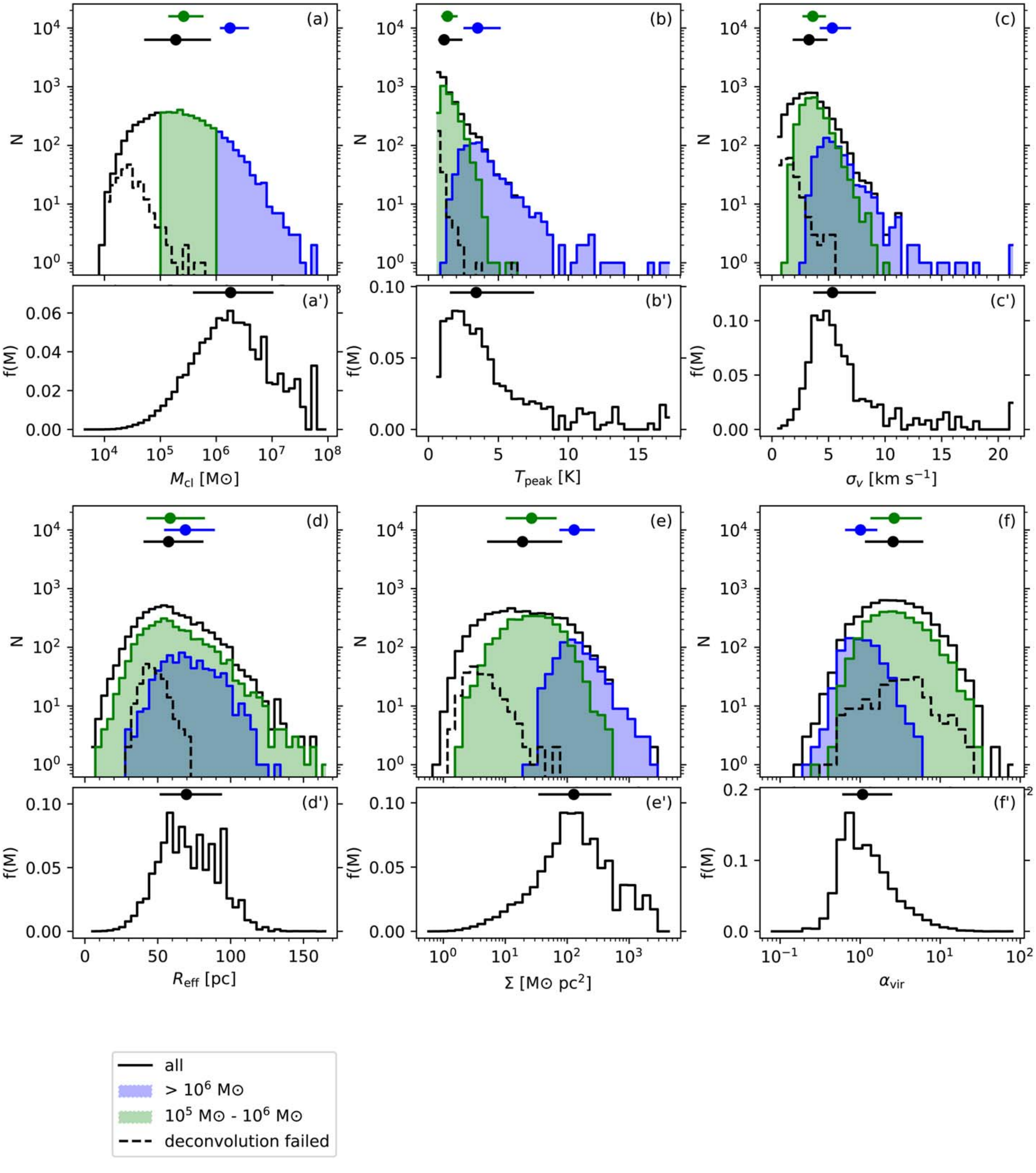

Figure 3. (a) Distribution of cloud mass $M_{\rm cl}$ in M83. In the upper panel, the black histogram shows the overall distribution. The blue solid, green solid, and black dashed histograms indicate the subsamples with $M_{\rm cl} > 10^6\ M_\odot$, $M_{\rm cl}$ in the range between 10^5 and $10^6\ M_\odot$, and with sizes that failed in the deconvolution (Section 2.3.2). In the same panel, the marker and horizontal line indicate the median and 16th-to-84th percentile range for all clouds (black), clouds with $>10^6\ M_\odot$ (blue), and clouds with 10^5–$10^6\ M_\odot$ (green). In the bottom panel, the mass-weighted histogram is shown. Note that, as the constant CO-to-H_2 conversion factor is adopted, it is equivalent to the luminosity-weighted histogram. The marker and horizontal line indicate the median and percentiles as the upper panel. (b)–(g) Same as (a), but for peak temperature $T_{\rm peak}$, velocity dispersion $\sigma_{\rm v}$, effective radius $R_{\rm eff}$, surface density Σ, and virial parameter $\alpha_{\rm vir}$, respectively.

in GMCs with $M_{\rm cl} > 10^6\ M\odot$, although such massive GMCs consist of less than 16% in number. Therefore, the small number of massive clouds contain the major fraction of the total gas mass in M83. This trend is similar to the inner Galactic disk (S87; M17). We will discuss the cloud mass spectrum in Section 4.

Table 3
Cloud Property Distribution Summary

(1)	$T_{\rm peak}$ (K) (2)	$\sigma_{\rm v}$ (km s^{-1}) (3)	$R_{\rm eff}$ (pc) (4)	$M_{\rm cl}$ (10^5) (5)	Σ ($M_\odot$ pc^{-2}) (6)	$\alpha_{\rm vir}$ (7)	$N_{\rm cl}$ (8)
	Unweighted percentiles						
All	$1.1^{2.4}_{0.7}$	$3.3^{4.9}_{1.8}$	59^{86}_{41}	$1.9^{8.1}_{0.51}$	$22^{100}_{5.8}$	$3.0^{7.0}_{1.0}$	5724
$>10^6$ $M_\odot$	$3.5^{5.2}_{2.5}$	$5.3^{7.0}_{4.2}$	69^{89}_{54}	18^{38}_{12}	130^{280}_{75}	$1.0^{2.0}_{0.6}$	734
$>10^5$ $\mathrm{M}_\odot$	$1.4^{2.1}_{0.91}$	$3.6^{4.8}_{2.7}$	59^{83}_{42}	$2.6^{5.9}_{1.4}$	$27^{68}_{10.0}$	$3.0^{6.0}_{1.0}$	3124
	Weighted percentiles						
All	$3.4^{7.6}_{1.5}$	$5.4^{9.2}_{3.6}$	70^{94}_{51}	$18^{110}_{3.8}$	130^{520}_{35}	$1.0^{3.0}_{0.6}$	5724
$>10^6$ $M_\odot$	$4.7^{9.3}_{3.0}$	$6.5^{11}_{4.8}$	78^{96}_{58}	37^{160}_{15}	230^{870}_{99}	$0.8^{1.0}_{0.5}$	734
$>10^5$ $M_\odot$	$1.7^{2.5}_{1.1}$	$3.9^{5.1}_{3.0}$	59^{81}_{43}	$4.6^{8.0}_{2.1}$	42^{88}_{16}	$2.0^{4.0}_{1.0}$	3124

Note. Median and 16th-to-84th percentile range of the cloud properties. Column (1): radial range. Column (2): peak brightness temperature. Column (3): velocity dispersion. Column (4): effective radius. Column (5): mass. Column (6): surface density. Column (7): virial parameter. Column (8): number of clouds.

3.1.2. Peak Temperature

Figure 3(b) shows that $T_{\rm peak}$ has a tail toward the higher end with a maximum value of ∼15 K. The unweighted and mass-weighted median values among all the GMCs are 1.3 and 3.4 K, respectively, having more than a factor of 2 difference. On the contrary, the difference is smaller for massive clouds with $M_{\rm cl} > 10^6\ M_\odot$ (3.5 and 4.7 K). Again, this is because the small number of massive clouds determines the mass-weighted average properties of the GMC population in M83.

We note that, in previous extragalactic GMC studies, median $T_{\rm peak}$ in the sampled clouds is often around 3 K, specifically 3.0 K in M51 (D. Colombo et al. 2014) and 3.3 K in M83 (A. Hirota et al. 2018), and is higher than our median $T_{\rm peak}$ of 1.3 K. This is due to low sensitivities in the previous studies, which were made with similar spatial resolutions comparable to that in this study (∼46 pc). In the previous studies, the most frequent cloud masses were $10^6\ M_\odot$ or higher. This work detects abundant clouds with smaller masses by sampling clouds with the minimum $T_{\rm peak}$ of ∼0.5 K.

3.1.3. Velocity Dispersion and Radius

Figures 3(c)–(d) show the distribution of $\sigma_{\rm v}$ and $R_{\rm eff}$, respectively. The two quantities show different tendencies concerning the classification by $M_{\rm cl}$. The $\sigma_{\rm v}$ values tend to be higher for more massive clouds, but such a trend is less evident for $R_{\rm eff}$.

The distribution of $\sigma_{\rm v}$ has a skewed tail toward the higher end, extending over 20 km s^{-1}. The unweighted and mass-weighted median values of $\sigma_{\rm v}$ are 3.3 and 5.3 km s^{-1}, respectively. The 16 percentile of $\sigma_{\rm v}$ is 1.8 km s^{-1} and is well above the instrumental resolution of 0.3 km s^{-1} (Section 2.3.2). Hence, the measured $\sigma_{\rm v}$ should be almost unaffected by the instrumental resolution.

In contrast to $\sigma_{\rm v}$, the mass dependence is not clear for $R_{\rm eff}$. The unweighted median $R_{\rm eff}$ is 59 pc, and the maximum $R_{\rm eff}$ is ∼100 pc. There are 225 clouds with failure in the deconvolution for $R_{\rm eff}$ since their predeconvolution sizes are less than the spatial resolution (Section 2.3.2). Figure 3 shows that such deconvolution-failed clouds mostly have $M_{\rm cl}$ smaller than $10^5\ M_\odot$.

In this study, the dynamic range in $R_{\rm eff}$ is limited, with only a factor of 2 difference between the 16th and 84th percentiles (41 and 86 pc). The 84th percentile of 86 pc is easily acceptable as the most significant cloud size should be limited by the thickness of the molecular gas disk, which is estimated to be of an order of 100 pc in local disk galaxies. For example, the FWHM thickness of the molecular gas disk of the MW is ∼100 pc (M. Heyer & T. M. Dame 2015). On the other hand, the 16th percentile of 41 pc needs consideration because $R_{\rm eff}$ is deconvolved, and typical GMCs in the MW have smaller sizes. Most of the recent cloud identification algorithms have a known tendency to find structures with sizes a few times the instrumental resolution (G. L. Verschuur 1993; A. Hughes et al. 2013), and the $R_{\rm eff}$ distribution suggests that the same tendency also applies here.

The bootstrap error estimation made in Section 2.3.1 indicates the measured $R_{\rm eff}$ is more uncertain than $\sigma_{\rm v}$, which would indicate that the resolution is more marginal in the spatial directions than the velocity direction. As we identified clouds from the masked data cube, in which all the valid voxels are positive (>2σ), the cloud radii tend to be overestimated rather than underestimated due to the measurement uncertainty. The relatively large 16th percentile of $R_{\rm eff}$, 41 pc, could also be a consequence of the overestimation of radius in small clouds. Therefore, even if the beam deconvolution is made to $R_{\rm eff}$, there might still remain uncertainties on the beam filling factor. Further discussion about this point will be made in Section 6.

3.1.4. Surface Density

Figure 3(e) shows the distribution of Σ. The unweighted and mass-weighted median values are 22 $M_\odot\,{\rm pc}^{-2}$ and 128 $M_\odot\,{\rm pc}^{-2}$, respectively; the mass-weighted median is skewed toward massive clouds. This mass-weighted median is close to the median Σ for clouds with $M > 10^6\ M_\odot$ (130 $M_\odot\,{\rm pc}^{-2}$). This alignment suggests a trend that massive GMCs account for the majority of the molecular gas mass in M83.

We note that the previous extragalactic studies in molecular-rich gas disks with shallower mass sensitivities found median Σ similar to that for $M_{\rm cl} > 10^6\ M_\odot$ clouds in M83 (e.g., 177 $M_\odot\,{\rm pc}^{-2}$ in M51; D. Colombo et al. 2014; 106 $M_\odot\,{\rm pc}^{-2}$ in M83, A. Hirota et al. 2018; also 170 $M_\odot$ ${\rm pc}^{-2}$ in M83, P. Freeman et al. 2017; 100^{+160}_{-60} $M_\odot\,{\rm pc}^{-2}$ in 10 galaxies covered by the PHANGS program, E. Rosolowsky et al. 2021).

The unweighted median Σ of 22 $M_\odot\,{\rm pc}^{-2}$ is below the median value by S87 and is close to that among the inner Galactic clouds by M17 (31.6 $M_\odot\,{\rm pc}^{-2}$; see also Appendix D). However, we will discuss that our median aligns better with the high value of S87 after a beam dilution correction (see Section 6).

3.1.5. Virial Parameter

Figure 3(f) shows distribution of $\alpha_{\rm vir}$. With an assumption of negligible support from magnetic fields and confinement by external pressure, $\alpha_{\rm vir} \sim 1$ indicates the virial equipartition, and $\alpha_{\rm vir} \sim 2$ indicates the equipartition between kinetic and gravitational energies (loosely gravitationally bound). The unweighted median $\alpha_{\rm vir}$ is ~2.4, which is similar to the ones found in some of the recent extragalactic cloud surveys. For example, J. Sun et al. (2020b) found the median $\alpha_{\rm vir}$ of 2.7 from 70 galaxies included in the ALMA-PHANGS program. Recent Galactic cloud catalogs also report higher $\alpha_{\rm vir}$ than ~1, which is suggested from S87's data by assuming a constant $\alpha_{\rm CO}$ of 4.4 $M_\odot$ / (K km s^{-1} pc^2). Using the same $\alpha_{\rm CO}$, the clouds sampled by R16 indicate a median $\alpha_{\rm vir}$ of 2.3 for the entire Galactic disk, although it lowers to ~1.5 if the inner Galactic disk clouds are concerned (Appendix D). Even higher median $\alpha_{\rm vir}$ of ~7 and ~11 are found in the inner and outer Galactic disk by M17 (see also N. J. Evans et al. 2021).

Mass-weighted mean $\alpha_{\rm vir}$ is close to 1; thus, massive GMCs appear more gravitationally bound than less massive ones at first glance. We show in Appendix C that $\alpha_{\rm vir}$ of the M83 clouds tends to vary as $\propto M_{\rm cl}^{-0.5}$. A similar tendency is also seen in previous cloud studies made in different environments (M. H. Heyer et al. 2001; M17; N. J. Evans et al. 2021; also see Figure 2 of M. Chevance et al. 2023). We argue in Appendix C that the limited spatial resolution could be forming the trend in the sampled M83 clouds.

3.2. Scaling Relations

The scaling relations of cloud properties were empirically established by the early studies of Galactic clouds (R. B. Larson 1981; S87). In particular, the following relations are collectively referred to as Larson's relationships and more qualitatively determined by S87: molecular clouds (i) have a power-law relation between their velocity dispersions $\sigma_{\rm v}$ and radius $R_{\rm eff}$,

$$\sigma_{\rm v} = C R_{\rm eff}^{0.5}, \tag{9}$$

with a scaling coefficient C of 0.72 km s^{-1} pc$^{-1/2}$, (ii) have a near-linear scaling between virial mass and CO luminosity, and (iii) have a constant surface density of ~200 $M_\odot$ pc^{-2} (S87).

These three relationships are interdependent on each other (M. Heyer et al. 2009; J. Ballesteros-Paredes et al. 2011): by equating the two estimations of cloud mass based on luminosity ($\pi R_{\rm eff}^2 \Sigma$) and virial equations ($M_{\rm vir}/\alpha_{\rm vir}$), we have

$$C = \sigma_{\rm v}/\sqrt{R_{\rm eff}} = \left(\frac{2}{9}\alpha_{\rm vir} G \pi \Sigma\right)^{1/2}. \tag{10}$$

Therefore, $\propto R_{\rm eff}^{1/2}$ scaling of $\sigma_{\rm v}$ (first relationship) is derived when $\alpha_{\rm vir}$ and Σ are constant, which are derived from the second and third relationships. M. Heyer et al. (2009) also pointed out that the coefficient C varies among clouds sampled in more diverse environments than those in S87, and it scales as $\Sigma^{1/2}$ as expected by Equation (10). J. Ballesteros-Paredes et al. (2011) discussed the same dependence in the context of freefall collapse (see also R. B. Larson 1981).

Larson's relations (the S87's relations) are often taken as reference relations to compare cloud properties among various environments (e.g., A. D. Bolatto et al. 2008; A. Hughes et al. 2013). In an inner portion of M83, A. Hirota et al. (2018) sampled clouds from ^{12}CO (1–0) data observed with ALMA and found that GMCs in the disk region show similar characteristics as S87's clouds with median $\alpha_{\rm vir}$ and Σ of ~1 and ~100 $M_\odot$ pc^{-2}, respectively. The new data surpass this previous study in sensitivity, although the spatial resolutions are similar: most clouds have $T_{\rm peak} > 2$ K in A. Hirota et al. (2018), while median $T_{\rm peak}$ is about 1 K in this study. In what follows, we show clouds with $T_{\rm peak} > 2$ K and <2 K as separate subsets and show that the $T_{\rm peak} > 2$ K clouds mostly agree with S87's relations, while the $T_{\rm peak} < 2$ K clouds do not and are more aligned with more recent Galactic clouds surveys (see Appendix D). Later in Section 6, we will show that the majority of the $T_{\rm peak} < 2$ K clouds are likely affected by beam dilution and discuss that they could also follow S87's relations when the effect of dilution (i.e., beam filling factor) is corrected.

We note one caveat about the scaling relations. The near-constant Σ of ~200 $M_\odot$ pc^{-2} in S87's clouds is a consequence of the selection effect, resulting from the high-intensity thresholds adopted by S87 for identifying cloud peaks (M. Lombardi et al. 2010). Recent studies of Galactic molecular clouds report a wider range of Σ, in particular with a lower median Σ (e.g., R16; M17; D. Colombo et al. 2019), which resembles low Σ values found for the $T_{\rm peak} < 2$ K sample of clouds in M83. A comparison of the M83 clouds with the catalogs of R16 and M17 is presented in Appendix D.

3.2.1. Line-width–Size Relation

Figure 4(a) shows the relationship between $\sigma_{\rm v}$ and $R_{\rm eff}$ for the clouds in M83. The line-width–size relation of S87, Equation (9), $C = 0.72$ km s^{-1} pc$^{-1/2}$, is also shown with the black dashed line for reference.

Any sign of a correlation is hardly seen for $\sigma_{\rm v}$–$R_{\rm eff}$ relation with the entire sample of M83 clouds with a low Spearman's rank correlation coefficient of ~0.3. The absence of the correlation is often seen in other extragalactic GMC studies (e.g., A. Hughes et al. 2013).

Another point to note is that most samples have $\sigma_{\rm v}$ significantly lower than expected from S87's relation. Clouds with low $T_{\rm peak}$ mostly drive the downward deviation as the 20% level contour of the distribution density of the clouds with $T_{\rm peak} < 2$ K is located below the line of S87's relation. On the other hand, at least some of the clouds with $T_{\rm peak} > 2$ K are compatible with S87's relation, as indicated by the location of its distribution density contour.

As a further reference, we plot the median $\sigma_{\rm v}$ values derived for the binned cloud radii for the clouds with $T_{\rm peak} > 2$ K and <2 K with red and purple markers, respectively. The running-median values exhibit a clear separation by $T_{\rm peak}$. While the median $\sigma_{\rm v}$ for >2 K clouds is located close to S87's relation of $\sigma_{\rm v} \propto C R_{\rm eff}^{1/2}$ with C of 0.72 km s^{-1} pc$^{-1/2}$, that for <2 K clouds follows the one with C half of S87's value, i.e., 0.36 km s^{-1} pc$^{-1/2}$.

The alignment of >2 K clouds with S87's relation suggests that luminous clouds in M83 might share the same characteristics as the Galactic clouds sampled by S87. In the early study of S87, the Galactic clouds were identified by high-intensity detection thresholds, so the S87's relation would represent the properties of discrete GMCs with high Σ. Therefore, the

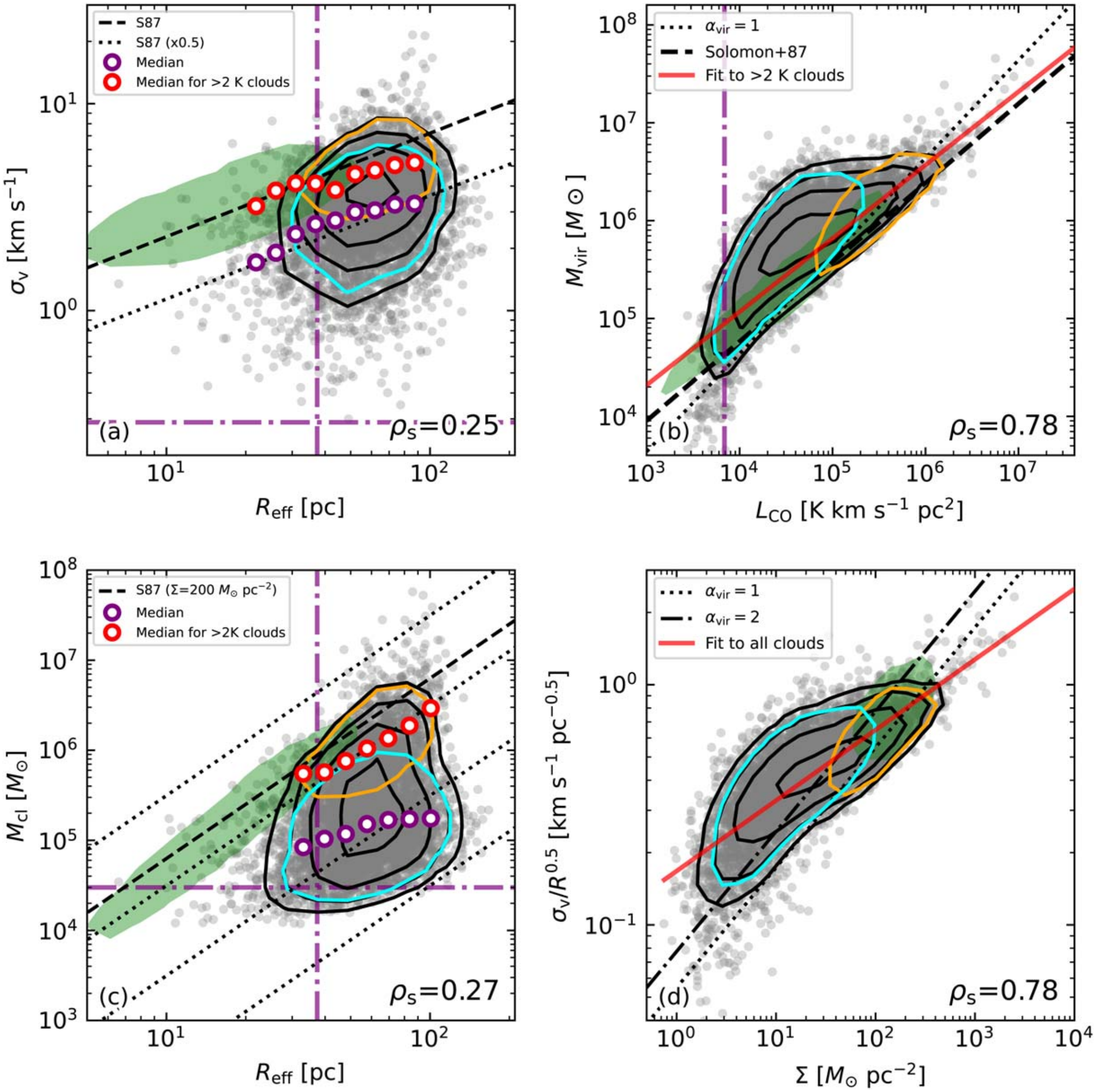

Figure 4. Scaling relations of cloud properties. In each plot, the raw data points for the M83 clouds are shown with the gray markers, and the data density is displayed with the black contour lines at 10%, 20%, 40%, and 80% levels of the maximum density, respectively. In the bottom-right corner of the plot, Spearman's rank correlation coefficient is noted. Orange and cyan contour lines indicate the distribution of $T_{\rm peak} > 2$ K and <2 K clouds, respectively, at the 20% density level. The green-shaded region indicates the distribution density of the Galactic clouds of S87 at a 20% level. Where appropriate, the resolution limits for $\sigma_{\rm v}$ of $1/\sqrt{12}$ km s^{-1} and $R_{\rm eff}$ of ∼37 pc ($=1.91 \times \theta_{\rm b}/\sqrt{8\log 2}$)) and the luminosity limit of ∼6900 K km s^{-1} pc^2, which corresponds to the expected minimum mass of $\sim 3 \times 10^4\ M_\odot$ (Section 2.6), are shown with the purple dashed–dotted line in each plot. (a) $\sigma_{\rm v}$–$R_{\rm eff}$ relationship. The black dashed line indicates the $\sigma_{\rm v}$–$R_{\rm eff}$ relation of S87, which is Equation (9) with $C = 0.72$ km s^{-1} pc$^{-1/2}$. The dotted line is the one with C half of S87's value. The purple open markers indicate the median $\sigma_{\rm v}$ derived at the binned $R_{\rm eff}$, and the red open marker running median for $T_{\rm peak} > 2$ K clouds. (b) $M_{\rm vir}$–$L_{\rm CO}$ relationship. The dashed line indicates the relation of S87 ($M_{\rm vir} \propto L_{\rm CO}^{0.81}$), and dotted line is $\alpha_{\rm vir} = 1$. The red line indicates the fit to the M83 clouds with $T_{\rm peak} > 2$ K (Equation (11)). (c) $M_{\rm cl}$–$R_{\rm eff}$ relationship. The dotted lines indicate the lines for Σ of 1, 10, 100, and 1000 $M_\odot$ pc^{-2}, respectively. The dashed line indicates $\Sigma = 200\ M_\odot$ pc^{-2}, implied from S87's scaling relations. As in (a), the running median for all the samples and >2 K clouds are shown with red and purple markers. (d) $\sigma_{\rm v}/R_{\rm eff}^{1/2}$–Σ relationship. The red line indicates the fit to all M83 clouds (Equation (12)). The lines of $\alpha_{\rm vir}$ of 1 and 2 are shown with the dotted and dashed–dotted lines, respectively.

luminous clouds in M83 might have properties similar to the dense GMCs in the MW. Again, we note that these clouds are the dominant contributor to the total CO luminosity of the galaxy.

3.2.2. Virial Mass–CO Luminosity Relation

Figure 4(b) shows the relationship between the $M_{\rm vir}$ and $L_{\rm CO}$. The dashed line on the figure indicates the case for the simple virial equilibrium, $\alpha_{\rm vir} = 1$, with the "standard" CO-to-H$_2$ conversion factor of 2.0×10^{20} cm^{-2} / (K km s^{-1}).

As a whole, both quantities are well correlated to each other with Spearman's correlation coefficient of ∼0.8. In particular, the >2 K clouds exhibit a tight correlation, located within a factor of 3 variation to $\alpha_{\rm vir}$ of 1. The <2 K clouds also show a correlation but are located upward of the line of $\alpha_{\rm vir} = 1$. Such upward deviation is often interpreted as the supervirial state of clouds or the variation in the CO-to-H$_2$ conversion factor.

The Galactic clouds of S87 exhibit a narrow range of distribution on the plot, with the fitted result of $M_{\rm vir}(M_\odot) = 43$ $[L_{\rm CO}({\rm K\ km\ s^{-1}pc^2})]^{0.81}$ after adjusting for the adopted distance

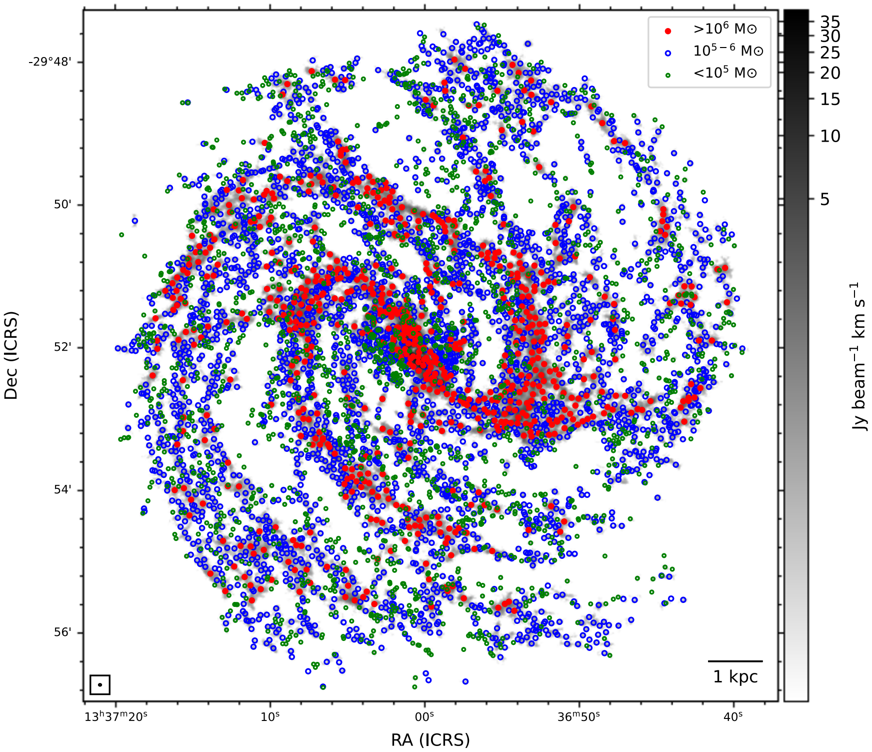

Figure 5. Distribution of the identified clouds overlaid on the CO map. Clouds with masses over $10^6\ M_\odot$, between $10^5\ M_\odot$ and $10^6\ M_\odot$, and below $10^5\ M_\odot$ are indicated with red-filled, blue open, and green open markers, respectively.

to the GC (S87; see also A. D. Bolatto et al. 2013). The $T_{\rm peak} > 2$ K clouds mostly align with S87's reference relation. The least-square fitting to >2 K clouds yields

$$M_{\rm vir}(M_\odot) = (114 \pm 5)[L_{\rm CO}({\rm K\ km\ s^{-1}pc^2})]^{0.75 \pm 0.02}, \qquad (11)$$

which has an index similar to S87's relation.

3.2.3. Mass–Size Relation

Figure 4(c) shows the relationship between $M_{\rm cl}$ and $R_{\rm eff}$. The lines for $\Sigma = 1$, 10, 100, and 1000 $M_\odot\,{\rm pc}^{-2}$ are drawn for reference with dotted lines. The Galactic clouds of S87 lie close to a constant Σ line of 200 $M_\odot\,{\rm pc}^{-2}$.

In contrast to the narrow range of Σ seen in S87's MW clouds, the measured properties of the M83 clouds exhibit a wide range of Σ, reaching about 3 orders of magnitude on the plot. The wide range is similar to the Galactic clouds sampled by M17 (see their Figure 7(a)). The correlation coefficient is low for the entire sample (∼0.3). Still, the >2 K clouds are centered around the constant Σ of 100 $M_\odot\,{\rm pc}^{-2}$. Taking the running median of $M_{\rm cl}$ for >2 K and <2 K clouds as was made in $\sigma_{\rm v}$–$R_{\rm eff}$ relation, it is apparent that the > 2 K clouds are distributed close to the line of constant $\Sigma = 100\ M_\odot\,{\rm pc}^{-2}$. For the <2 K clouds, the slope of the median mass values is shallower than those of the constant Σ lines, suggesting a trend that (apparently) larger clouds have smaller Σ.

3.2.4. Normalized Velocity Dispersion–Surface Density Relationship

Figure 4(d) shows the relationship between the normalization coefficient of the line-width–size relation $C\,(=\sigma_{\rm v}/R_{\rm eff}^{1/2})$ and Σ. As in Equation (10), C is proportional to $\Sigma^{1/2}$ for clouds dominated by self-gravity if $\alpha_{\rm vir}$ is approximately constant. The dashed and dotted lines show the expected behaviors for $\alpha_{\rm vir}$ of 1 and 2, corresponding to the gravitational virial equilibrium and freefall collapse, respectively.

A high correlation coefficient of ∼0.8 is obtained, but this is trivially expected because the scaling between C and $\Sigma^{1/2}$ is mathematically equivalent to the $M_{\rm vir}$–$L_{\rm CO}$ scaling (Section 3.2.2).

If all the clouds are strongly governed by self-gravity, we would expect all the data points to be clustered around the lines of $\alpha_{\rm vir} = 1$ and 2. However, we see upward deviations from these lines toward lower Σ, mainly driven by the clouds with $T_{\rm peak} < 2$ K. To characterize the deviation, a least-square fitting to the entire sample is made:

$$\sigma_{\rm v}\,({\rm km\ s^{-1}})/\sqrt{R_{\rm eff}\,({\rm pc})} = (0.16 \pm 0.01)[\Sigma(M_\odot\ {\rm pc^{-2}})]^{0.30 \pm 0.01}. \qquad (12)$$

This index, ∼0.30, is shallower than the 0.5 for clouds governed by self-gravity (Equation (10)).

The clouds with $T_{\rm peak} > 2$ K and $T_{\rm peak} < 2$ K make a clear separation on the plot. The >2 K clouds are mostly clustered around the line of $\alpha_{\rm vir} = 1$ and over a factor of a few range around $\Sigma \sim 100\ M_\odot\,{\rm pc}^{-2}$. On the other hand, the <2 K clouds are distributed systematically in the area of $\alpha_{\rm vir} > 1$ (the 20% density level barely crosses the line of $\alpha_{\rm vir} = 1$). Their Σ values are lower. The shallow index of ∼0.3 of the $\sigma_{\rm v}/\sqrt{R}$–Σ relation is driven by the larger $\alpha_{\rm vir}$ in the clouds with $T_{\rm peak} < 2$ K. We will discuss the impact of beam dilution on $\alpha_{\rm vir}$ and Σ in Section 6 and also show that the beam dilution also explains the shallow index of ∼0.3 in Appendix B.

3.3. Spatial Distribution of the Clouds

Figure 5 shows the distribution of the identified clouds, categorized into three groups by mass: $<10^5$, 10^{5-6}, and $>10^6\ M_\odot$, respectively. Massive clouds over $10^6\ M_\odot$ are

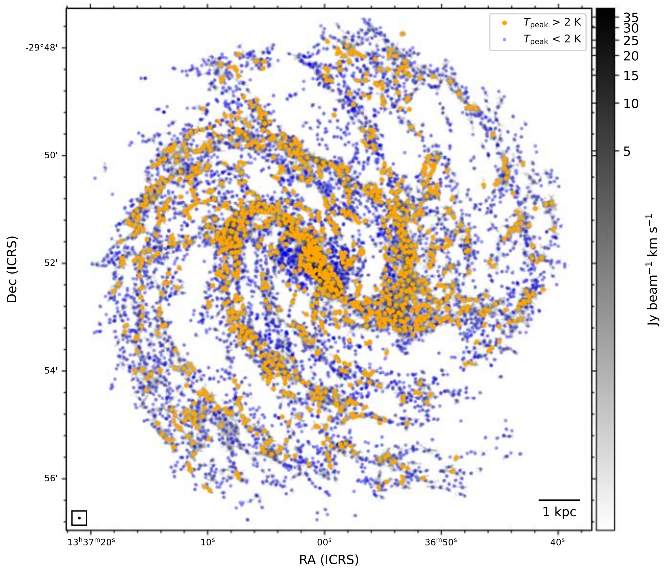

Figure 6. Same as Figure 5, but clouds are classified with a $T_{\rm peak}$ threshold of 2 K. Clouds with $T_{\rm peak} > 2$ K and <2 K are indicated with orange and blue markers, respectively.

strongly concentrated around bright galactic structures, namely, the GC, bar, and spiral arms. On the contrary, smaller clouds (below $10^6\ M_\odot$) prevail over the wider area, residing both in arm and interarm regions. This confirms the similar trends reported in other galaxies (e.g., J. Koda et al. 2009; D. Colombo et al. 2014).

Figure 6 also shows the distribution of the clouds but categorized with $T_{\rm peak} > 2$ K and <2 K. As $M_{\rm cl}$ and $T_{\rm peak}$ are correlated, Figures 5 and 6 resemble each other. High-$T_{\rm peak}$ clouds (>2 K) are often found within bright galactic structures, as were for the massive clouds. In the previous subsection, we saw that the properties of the >2 K clouds mostly agree with the relations of S87. The observation that >2 K clouds are found within or around larger-scale structures, such as bar, arm, and spurs, suggests that the galactic structures play an important role in assembling the massive, bright clouds that share similar properties as S87's sample.

3.3.1. Spiral Arm Locations Traced by Molecular Clouds

Figure 7(a) plots the clouds on the $\log R_{\rm gal}-\phi$ plane. As seen above, the massive clouds (> $10^6\ M_\odot$) highlight the locations of the spiral arms. We identify sequences of the massive clouds on the $\log R_{\rm gal}-\phi$ plane and linearly fit the sequences (i.e., logarithmic spiral arms with constant pitch angles). The fit results are shown in the plot.

Figure 7(b) displays the fitted logarithmic spiral structures in a two-dimensional map and the distribution of clouds with masses above $10^6\ M_\odot$. The identified structures are tied to the following knowledge. In the inner part of M83, the two main spiral arms extend from both ends of the bar. The eastern main arm is displayed with the blue line, and on the trailing side of it, a narrower molecular ridge runs parallel, shown as the yellow line. This narrow ridge is seen as a dust lane at optical wavelengths (see also R. J. Rand et al. 1999) but has weaker CO emission compared to the main arm (A. Hirota et al. 2018). At first glance, the western spiral arm appears to have a long extension from the western end of the bar toward the eastern side, but it has two changes in pitch angle on the $\log R_{\rm gal}-\phi$ plane. Therefore, it is divided into three segments, shown with the orange, green, and purple lines. In the outermost part, the eastern arm appears as "a bundle of narrower filaments or ripples" on the CO image (J. Koda et al. 2023)—the purple, brown, and red lines correspond to such molecular filaments. Although the outermost western spiral segment is less defined than the inner main spirals, we tentatively identified a logarithmic spiral shown as the pink line. Further discussion on the spiral structures in the CO image is also available in J. Koda et al. (2023; see Figure 11).

We define a region mask using the fitted arm positions for the analyses in the following sections (Figure 7(c)). In this mask, each of the logarithmic spiral arm regions has a width of 40″ (~880 pc), and the bar region has an ellipse with major and minor axis lengths of 86″ and 32″ respectively, with a position angle of 225°. The central region is defined as $R_{\rm gal} < 16''$ (~350 pc). The mask contains a majority of massive or bright clouds. Out of 734 clouds with $>10^6\ M_\odot$ in M83, 498 clouds reside in the arm/bar/center mask. The total mass of $>10^6\ M_\odot$ clouds is $\sim 2.2 \times 10^9\ M_\odot$, and about 80% of the mass is included in the mask.

4. Cloud Mass Function

The mass distribution of GMCs is characterized by a mass function of a power-law form, i.e., $dN/dM \propto M^{\gamma}$. The early GMC surveys in the inner Galactic disk consistently found the index γ of around −1.5 (D. B. Sanders et al. 1985; S87; J. P. Williams & C. F. McKee 1997; E. Rosolowsky 2005). Subsequent studies in other environments also found γ mainly in the range of −1.5 to −2.5 (M. H. Heyer et al. 2001; D. Colombo et al. 2014), but even steeper relations' (more negative) values of γ are also found in some environments (e.g., G. Engargiola et al. 2003; Y. Fukui et al. 2008). For a power-law distribution, $\gamma > -2$ means that a small number of massive clouds carry most of the total cloud mass, like the GMC mass distribution in the Galactic disk. In contrast, $\gamma < -2$ means that most cloud mass resides in the smaller mass end.

At the higher end of the mass distribution, the deficit of massive clouds is also often seen: in the Galactic disk, clouds more massive than a few $10^6\ M_\odot$ are frequently underpopulated with respect to the power-law relation (J. P. Williams & C. F. McKee 1997). Some previous studies reported γ steeper (smaller) than −2, but this might be a consequence of fitting cloud mass distributions above such an upper limit mass (E. Rosolowsky 2005).

4.1. Functional Forms

We fit the cloud mass distribution in two forms. The first form is a power law, restricted by the upper mass limit $M_{\rm lim}$ as

$$\frac{dN}{dM} \propto \left(\frac{M_{\rm cl}}{M_{\rm lim}}\right)^{\gamma_{\rm PL}}, \quad M_{\rm cl} < M_{\rm lim}. \tag{13}$$

The form is conventionally applied to the cloud mass distributions (e.g., J. P. Williams & C. F. McKee 1997; E. Rosolowsky 2005; D. Colombo et al. 2014). It can be written in the integral form as follows:

$$N(>M) = N_{\rm u,PL}\left[\left(\frac{M_{\rm cl}}{M_{\rm lim}}\right)^{\gamma_{\rm PL}+1} - 1\right], \tag{14}$$

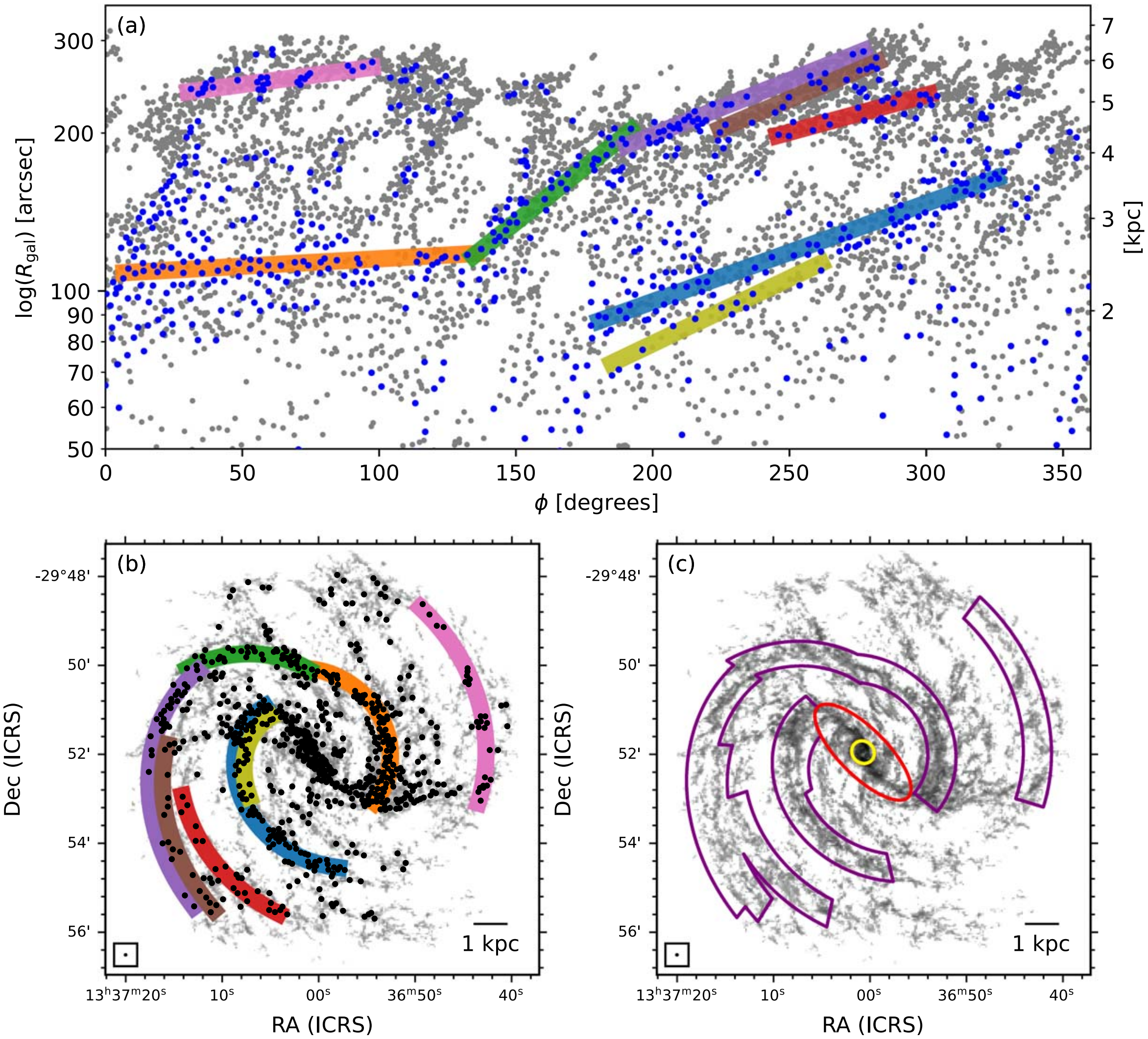

Figure 7. (a) Spatial distribution of the clouds on $\log R-\phi$ plot. Blue and gray markers indicate the locations of the clouds with masses above and below $10^6\ M_\odot$. The thick lines indicate the logarithmic spiral fitting to the selected clouds. (b) CO map overlaid with the logarithmic spiral arms indicated in (a). Black markers indicate the clouds with masses above $10^6\ M_\odot$. (c) Same as (b), but overlaid with the regional mask created here. The arms, the bar, and the central regions are indicated with purple, red, and yellow lines, respectively.

where $N_{\rm u,PL}$ is the number of clouds more massive than $2^{1/(\gamma_{\rm PL}+1)}M_{\rm lim}$, which we denote as $M_{\rm u,PL}$. We call $M_{\rm u,PL}$ the cutoff mass for the restricted power-law form because the deviation from a power law becomes obvious above $M_{\rm u,PL}$.

The second form combines the power-law distribution with an exponential cutoff, which is often called a Schechter-like function:

$$\frac{dN}{dM} \propto \left(\frac{M}{M_{\rm u,exp}}\right)^{\gamma_{\rm exp}} \exp\left(-\frac{M}{M_{\rm u,exp}}\right), \qquad (15)$$

where $\gamma_{\rm exp}$ is the index of a power-law distribution, and $M_{\rm u,exp}$ is the cutoff mass limit above which the distribution is suppressed with respect to the power law. Fitting the cloud mass distribution with this Schechter-like form would help test the connection between the mass spectra of GMCs and stellar clusters as the cluster mass distributions are often characterized with this form (e.g., J. M. D. Kruijssen 2014; A. Adamo et al. 2015). However, the application of this form to molecular cloud distributions is limited in recent studies (P. Freeman et al. 2017; E. Rosolowsky et al. 2021).

4.2. Cloud Mass Spectra

Figure 8 shows the cloud mass distributions for (a) all GMCs and (b)–(f) those in five radial bins. The latter is defined with the boundaries at 25″ (∼0.55 kpc), 100″ (∼2.2 kpc), 140″ (∼3.1 kpc), and 210″ (∼4.6 kpc), respectively, which are shown in Figure 1(b). They are to examine the radial and environmental variation of the cloud mass distribution: the first three bins mainly cover the central region, bar, and two main spiral arms, respectively, and the last two bins divide the outer galactic disk into two.

All the histograms show declines below around $2 \times 10^5\ M_\odot$, suggesting that cloud sampling is incomplete below that mass. As discussed in Section 2.6, our mass sensitivity in cloud identification is $\sim 3 \times 10^4\ M_\odot$ for a cloud in isolation. The difference would be attributed to the blending of cloud emissions. For a cloud to be detected above the high background surface density $\Sigma_{\rm bg}$ (e.g., in spiral arms), its mass has to exceed $\Sigma_{\rm bg}\, A_{\rm beam}$ with $A_{\rm beam}$ as beam area. For example, in most spiral arms, the typical $\Sigma_{\rm bg}$ is $100\ M_\odot\ {\rm pc}^{-2}$. Therefore, the minimum detectable mass in the arms cannot go below $\sim 2 \times 10^5\ M_\odot$ with the current resolution of ∼46 pc. Hereafter,

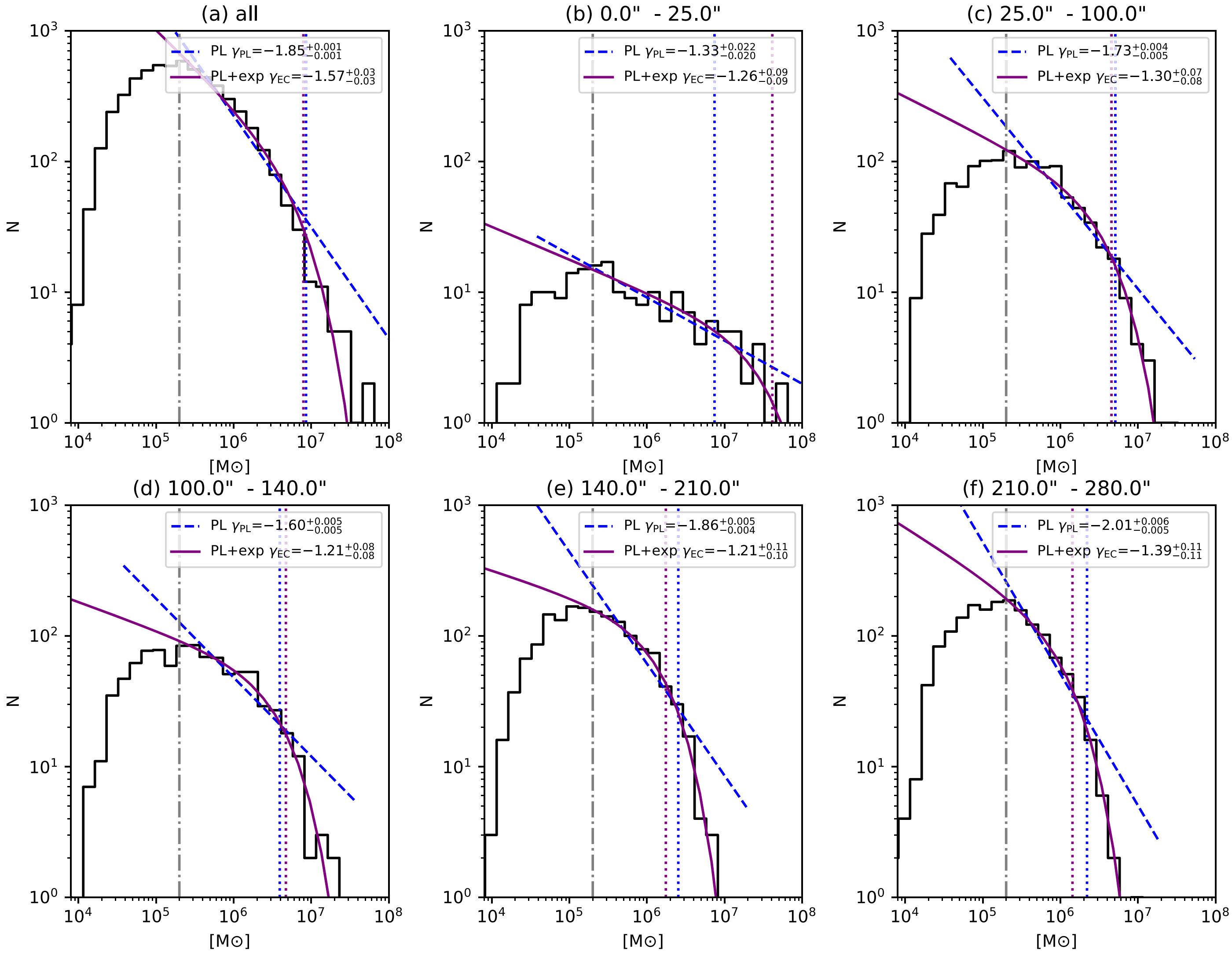

Figure 8. (a) Mass distribution for the molecular clouds in M83 displayed in the differential. The mass bins are configured with a width of 0.15 dex. The blue dashed line is the fit with a conventional form (Equation (14)), and the purple solid line indicates the fit with a Schechter-like form (Equation (15)). The vertical dashed–dotted line indicates the lower-mass limit used for fitting the data ($2 \times 10^5\ M_\odot$). The blue and purple dotted lines indicate the upper cutoff masses, $M_{\rm u,PL}$ and $M_{\rm u,exp}$, respectively, determined by fitting the data. (b)–(f) Same as (a), but for the radial range of $R_{\rm gal} = 0''$–$25''$, $25''$–$100''$, $100''$–$140''$, $140''$–$210''$, and $210''$–$280''$, respectively.

we regard $2 \times 10^5\ M_\odot$ as the effective completeness limit. This is a conservative limit in the disk region because the limit should be smaller in the interarm regions. However, the mass limit is higher in the central region because $\Sigma_{\rm bg}$ reaches nearly $1000\ M_\odot\ {\rm pc}^{-2}$ or higher there (J. Koda et al. 2023).

We fit only the clouds with $>2 \times 10^5\ M_\odot$ (above the completeness limit) with the two forms. We fitted the power-law form using the cumulative mass distribution function and least-square minimization against the integral form (Equation (14)). For the Schechter-like form (Equation (15)), we sample the likelihood using the `emcee` software library, which implements a Markov Chain Monte Carlo method (D. Foreman-Mackey et al. 2013). The prior distribution is configured such that the probability distribution of $\gamma_{\rm exp}$ is uniform between −5 and 0 and that $M_{\rm u,exp}$ is also uniform between $10^5\ M_\odot$ and $10^9\ M_\odot$ in the logarithmic space. Table 4 reports the fitted parameters and p-values calculated with the two-sample Kolmogorov–Smirnov test (K-S test) for both forms with the null hypothesis that the fitted and observed cumulative mass distributions are drawn from the same distribution.

Figure 8(a) shows the mass distribution for all the clouds. The power-law fit gives $\gamma_{\rm PL} \sim -1.85$, which is comparable to the indices found in the inner Galactic disk (e.g., −1.6 to −1.8; J. P. Williams & C. F. McKee 1997). The Schechter-like form yields an index $\gamma_{\rm exp}$ of ~ -1.57, which is shallower than $\gamma_{\rm PL}$ but is still comparable to the Galactic values. Both forms suggest the existence of upper cutoff masses with similar values, namely, $M_{\rm u,PL}$ of $\sim 8.6 \times 10^6\ M_\odot$ and $M_{\rm u,exp}$ of $\sim 8.0 \times 10^6\ M_\odot$, respectively.

Figure 8(b) is for the innermost radial bin of $R_{\rm gal} < 25''$ (∼550 pc). The fitted indices are shallow: $\gamma_{\rm PL} \sim -1.33$ and $\gamma_{\rm exp} \sim -1.26$. Due to the elevated background $\Sigma_{\rm bg}$, the shallow index is likely an artifact caused by the heavy blending of cloud emissions.

Figures 8(c)–(f) show the cloud mass distributions beyond $R_{\rm gal} \sim 550$ pc. Within the four radial bins, $\gamma_{\rm PL}$ varies within the range of ∼−1.7 to ∼−2.0 with a tendency of steeper index

Table 4
Mass Function Parameters

Range (kpc) (1)	$\gamma_{\rm PL}$ (2)	$N_{\rm u,PL}$ (3)	$M_{\rm u,PL}$ ($10^6\ M_\odot$) (4)	p-value (5)	$g_{\rm xp}$ (6)	$M_{\rm u,exp}$ ($10^6\ M_\odot$) (7)	p-value (8)
0.0–0.5	$-1.33^{+0.02}_{-0.02}$	$6.9^{+0.6}_{-0.7}$	$7.41^{+0.14}_{-0.37}$	1.00	$-1.26^{+0.09}_{-0.09}$	$46.29^{+38.51}_{-15.64}$	1.00
0.5–2.2	$-1.73^{+0.00}_{-0.00}$	$25.3^{+0.5}_{-0.5}$	$5.10^{+\ -0.06}_{-\ -0.07}$	0.10	$-1.30^{+0.07}_{-0.08}$	$4.52^{+1.00}_{-0.73}$	0.44
2.2–3.1	$-1.60^{+0.01}_{-0.01}$	$30.8^{+0.6}_{-0.5}$	$3.93^{+\ -0.02}_{-\ -0.02}$	0.46	$-1.21^{+0.08}_{-0.08}$	$4.69^{+1.02}_{-0.81}$	1.00
3.1–4.6	$-1.86^{+0.00}_{-0.01}$	$40.4^{+0.7}_{-0.7}$	$2.53^{+\ -0.02}_{-\ -0.02}$	0.33	$-1.21^{+0.11}_{-0.10}$	$1.79^{+0.34}_{-0.26}$	0.99
4.6–6.1	$-2.01^{+0.01}_{-0.01}$	$33.8^{+0.8}_{-0.8}$	$2.20^{+\ -0.03}_{-\ -0.03}$	0.27	$-1.39^{+0.11}_{-0.11}$	$1.45^{+0.31}_{-0.23}$	1.00
all	$-1.85^{+0.00}_{-0.00}$	$52.3^{+0.4}_{-0.4}$	$8.58^{+\ -0.06}_{-\ -0.06}$	0.00	$-1.57^{+0.03}_{-0.03}$	$7.93^{+1.15}_{-0.85}$	0.21

Note. Mass function parameters. Column (1): radial range. Columns (2)–(4): mass function parameters determined by the fitting with restricted power law, namely, power-law index $\gamma_{\rm PL}$, number of clouds at high-mass end $N_{\rm u,PL}$, and upper cutoff mass $M_{\rm u,PL}$. Column (5): K-S test p-value for the restricted power-law fitting. Columns (6) and (7): parameters determined by the fitting with the Schechter-like form, namely, index $g_{\rm xp}$ and upper cutoff mass $M_{\rm u,exp}$. Column (8): K-S test p-value for the Schechter-like form fitting.

toward the outer radius. On the contrary, the Schechter-like form results in more minor variations in $g_{\rm xp}$, ranging from -1.2 to -1.4, with no notable radial trend. In terms of the upper cutoff mass, both forms are again consistent. As we will comment later in Section 4.3, the Schechter-like form tends to characterize the variation in mass spectra by a change in $M_{\rm u,exp}$ rather than in $g_{\rm xp}$. Both $M_{\rm lim}$ and $M_{\rm u,exp}$ exhibit a factor of 3 declines with increasing galactocentric radii.

Figure 9 compares the upper cutoff mass determined from the fittings, $M_{\rm u,PL}$ and $M_{\rm u,exp}$, with the radial distribution of the individual cloud masses. This plot also shows the luminosity-weighted mean cloud mass in radial bins with a width of 12″. This luminosity-weighted mean mass declines radially, except for a slight secondary peak around $R_{\rm gal} = 100''$ where the main two spiral arms reside. The radially declining trend of the luminosity-weighted mean generally agrees with the variation of $M_{\rm u,PL}$ and $M_{\rm u,exp}$ derived from the fittings. The alignment would be reasonable as the slopes of the fitted mass functions in Figure 8 are mostly shallower than -2, and thus, most of the CO luminosity (and mass) should be concentrated around the upper cutoff mass.

4.3. Comparison of the Fitted Results between the Two Forms

Because of the discrepancies between $\gamma_{\rm PL}$ and $g_{\rm xp}$, one would wonder which of the two forms, namely, the restricted power-law form or Schechter-like form, provides a better characterization of the cloud mass distributions. The p-values of the K-S test in Table 4 are inconclusive. By taking the significance level of p-value as 0.05, the K-S test accepts almost all the cases except the restricted power-law form applied to all samples. The values of $g_{\rm xp}$ are shallow in most radial ranges with a slight variation (-1.2 to -1.4). The shallow and limited variation in $g_{\rm xp}$ might be due to the limited dynamic range in the fitting—there is only about an order of magnitude variation between $M_{\rm u,exp}$ and the adopted completeness limit of $2 \times 10^5\ M_\odot$. The exponential term induces a decline even below $M_{\rm u,exp}$ to some extent, further limiting the range available to fit as a power law. The determination of $g_{\rm xp}$ might become reliable only if higher resolution data becomes available to overcome the crowding effect to lower the mass completeness limit (see also E. Rosolowsky et al. 2021). As the K-S test gives no clear preference and as we suspect the fitted values $g_{\rm xp}$ might be biased, we consider $\gamma_{\rm PL}$ to be preferable to $g_{\rm xp}$, at least with the available data.

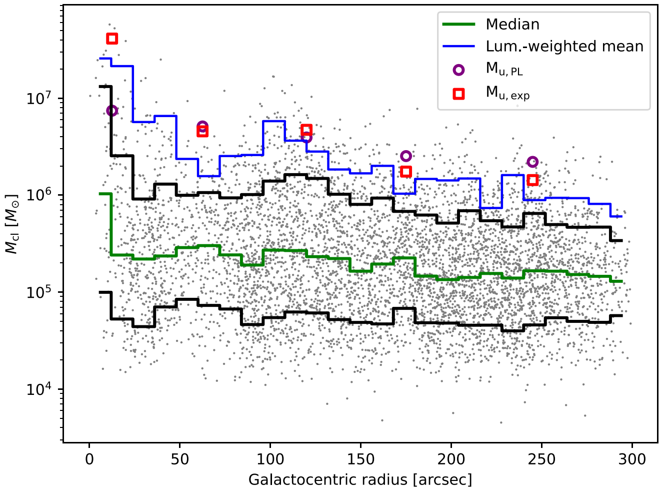

Figure 9. Cloud masses as a function of galactocentric radius, indicated with the gray dots. The green line indicates the median values at the radial bins with 12″ averaging widths. The blue line is the luminosity-weighted mean of the cloud masses calculated at the same bins. Black lines indicate the 16th and 84th percentile values at the same bins. Purple circle and red square markers indicate the estimated upper limits on cloud mass from the fittings of mass distributions, i.e., $2^{1/(g_{\rm PL}+1)}\ M_{\rm lim}$ and $M_{\rm u,exp}$, respectively, determined for five radial ranges listed in Table 4.

4.4. Possible Origins of the Radial Variation of Mass Spectra

The power-law fitting shows a radially steepening of $\gamma_{\rm PL}$ from -1.3 to -2.0 and a decrease of $M_{\rm u,PL}$, indicating a relative deficit of massive clouds toward the outer disk. The trends agree with other studies in M83 with shallower sensitivities (P. Freeman et al. 2017; A. Hirota et al. 2018) and also in different environments (e.g., D. Colombo et al. 2014). Several mechanisms might explain the radial trends in $\gamma_{\rm PL}$ and $M_{\rm u,PL}$. First, given that M83 has many bubble structures in infrared, H I, and CO, which likely influence and drive the evolution of molecular clouds, S.-i. Inutsuka et al. (2015) and M. I. N. Kobayashi et al. (2017) provide semianalytical calculations to describe the time evolution of molecular cloud mass functions regulated by multiple episodes of bubble expansions, which drive molecular cloud formation via shock compression of atomic gas. The idea would explain the steeper $\gamma_{\rm PL}$ in the outer disk as the slower cloud formation because the supernovae, which drive bubble expansions, are less frequent there. M. I. N. Kobayashi et al. (2017) also suggested the formation of massive clouds comparable to $M_{\rm u,PL}$ requires about 100 Myr by solving the time evolution, which agrees with the timescale predicted from the CO morphology of M83 (J. Koda et al. 2023). Second, the underpopulation of massive clouds above $M_{\rm u,PL}$ might also be due to a lower molecular fraction in massive clouds—B. G. Elmegreen (1989) provides that self-shielding decreases approximately as $\propto M^{-0.5}$ for virialized clouds, and therefore, CO line observations might trace only the core regions in most massive clouds. As there is a radial decrease of per-cloud molecular fraction in the MW (B. G. Elmegreen & D. M. Elmegreen 1987), it would be intriguing to compare molecular clouds with massive HI clouds in M83.

5. Cloud-to-cloud Velocity Dispersion

The vertical cloud-to-cloud velocity dispersion of a gaseous disk is a parameter that reflects the stability of the disk. Despite its importance, the measurements of the cloud-to-cloud velocity dispersion of molecular gas are still limited. In the MW, A. A. Stark (1984) found that the cloud-to-cloud velocity dispersion within the Galactic plane weakly depends on cloud mass, with 6.6 and 9.0 km s^{-1} for cloud masses of $10^{4-5.5}\,M_\odot$ and $10^{2-4}\,M_\odot$, respectively. However, the estimation from the MW data involves an assumption of the isotropy of velocity dispersion.

Extragalactic observations of nearly face-on galaxies permit estimation of the vertical cloud-to-cloud velocity dispersion. Previous measurements were performed at subkiloparsec-scale resolutions, which blend several GMCs within resolution elements; they found dispersions of 6–9 km s^{-1} when an individual spectrum of each pointing is analyzed (F. Combes & J.-F. Becquaert 1997; C. D. Wilson et al. 2011; K. M. Mogotsi et al. 2016) and about 12–14 km s^{-1} when the spectra at multiple pointings are stacked (A. Caldú-Primo et al. 2013; A. Caldú-Primo & A. Schruba 2016). With the new cloud catalog and low inclination angle of M83, we can make a more direct estimation of the vertical cloud-to-cloud velocity dispersion.

5.1. Method to Estimate Vertical Velocity Dispersion of Clouds

We adopt a method similar to the one used by S. Hernandez et al. (2019) to estimate the vertical velocity dispersion of stellar clusters. The line-of-sight velocity $v_{\rm LOS}$ of a cloud rotating in the disk is written as

$$v_{\rm LOS} = v_{\rm sys} + (v_{\rm rot} + v_{\rm phi})\cos\phi\sin i + v_{\rm R}\sin\phi\sin i + v_{\rm z}\cos i, \tag{16}$$

where $v_{\rm sys}$, $v_{\rm rot}$, $v_{\rm phi}$, $v_{\rm R}$, $v_{\rm z}$, ϕ, and i are the systemic recession velocity, the circular rotational velocity expected from the galactic rotation curve, in-plane azimuthal and radial noncircular velocities that are mostly governed by streaming motions, vertical motion velocity, the angle from the major axis, and the inclination angle. We subtract the contributions of assumed $v_{\rm sys}$ and $v_{\rm rot}$ from $v_{\rm LOS}$ for each cloud. Then, the residual velocity $v_{\rm res}$ is left with the contributions from $v_{\rm z}$ and streaming motions as

$$v_{\rm res} = v_{\rm z}\cos i + v_{\rm phi}\cos\phi\sin i + v_{\rm R}\sin\phi\sin i. \tag{17}$$

As long as the contributions from the in-plane noncircular motions, i.e., the last two terms in this equation, are negligible, we can estimate the cloud-to-cloud velocity dispersion, $<v_{\rm z}>$, as the dispersion of $v_{\rm res}/\cos i$ among a sample of clouds.

We adopt $v_{\rm sys}$ of 511 km s^{-1} and i of 24° (J. Koda et al. 2023). For $v_{\rm rot}$, we use the rotation curve of A. Hirota et al. (2014), which is obtained by subtracting the rotational velocities estimated from the stellar mass distribution using the Two Micron All Sky Survey Large Galaxy Atlas image (T. H. Jarrett et al. 2003) with an assumption of the maximum disk contribution.

5.2. Vertical Cloud-to-cloud Velocity Dispersion

Figure 10(a) shows $v_{\rm res}$ as a function of galactocentric radius $R_{\rm gal}$ for the M83 clouds. The clouds with masses below and above $5\times10^5\,M_\odot$ are plotted separately with gray and cyan markers, respectively. The radial bins are configured with a width and increment of 24″ and 12″, up to 288″. The 16th, 50th, and 84th percentiles of $v_{\rm res}$ are plotted for each radial bin.

The absolute $|v_{\rm res}|$ values are elevated within the inner 100″ (∼2.2 kpc) of M83, where the stellar bar resides. Although $|v_{\rm res}|$ includes the contributions from the in-plane noncircular motions and vertical velocity dispersion (Equation (17)), the $v_{\rm phi}$ and $v_{\rm R}$ terms appear to be negligible except in the bar, which induces large noncircular streaming motions. Outside the bar, the 16th and 84th percentiles of $v_{\rm res}$ are within the range of $|v_{\rm res}| < 10$ km s^{-1}, suggesting only a modest impact of the arm-induced streaming motions. This suggestion agrees with R. P. J. Tilanus & R. J. Allen (1993), who found a modest streaming motion of about 15 km s^{-1} in the plane of M83.

Figure 10(b) shows the radial distribution of estimated cloud-to-cloud velocity dispersions, $<v_{\rm z}>$ for clouds above (cyan) and below (black) $5\times10^5\,M_\odot$. Except for the inner bar region ($R_{\rm gal} < 100''$; ∼2.2 kpc) where the impact of streaming motion is not negligible, we consider the data points to be the fair representatives of $<v_{\rm z}>$ based on the small variation in the scatters of $v_{\rm res}$ at $R_{\rm gal} > 100''$. At $R_{\rm gal} > 100''$, $<v_{\rm z}>$ is found to be almost constant around 8.3 km s^{-1} for $>5\times10^5\,M_\odot$ clouds and 11 km s^{-1} for $<5\times10^5\,M_\odot$ clouds.

We performed Levene's test at each radial bin to see the statistical significances of the differences in $v_{\rm res}$ between $>5\times10^5\,M_\odot$ and $<5\times10^5\,M_\odot$ clouds (Figure 10(c)). The test's null hypothesis is that the underlying $v_{\rm res}$ distribution is the same in both groups, i.e., the vertical velocity dispersion is the same. We discard the null hypothesis if the p-value of the test is below 0.05. The resultant p-values are far below the adopted significance level of 0.05 in most of the bins beyond $R_{\rm gal} > 100''$, suggesting that the mass dependence of $<v_{\rm z}>$ is significant there.

5.2.1. Assessment of the Impact of Streaming Motions on the Estimated Vertical Cloud-to-cloud Velocity Dispersion

A caveat of the $<v_{\rm z}>$ estimation made here is that the impact of in-plane noncircular motion is just neglected. As massive clouds are concentrated toward spiral structures (Section 3.3), one might suspect they are more susceptible to streaming motions. To eliminate this possibility, we show the spatial distribution of $v_{\rm res}$ for individual clouds in Figure 10(d). The

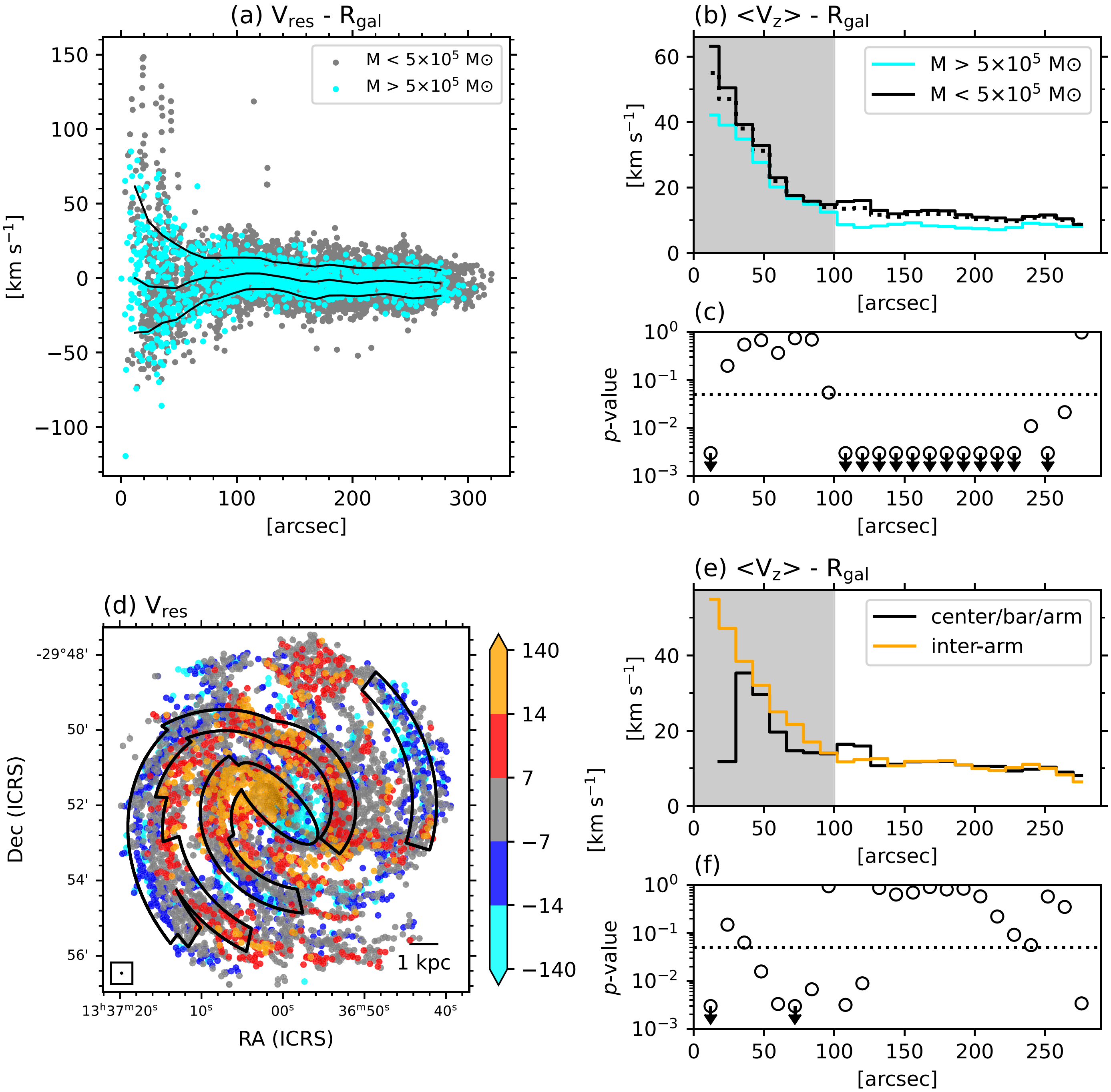

Figure 10. (a) Cloud's residual velocity $v_{\rm res}$ as a function of galactocentric radius $R_{\rm gal}$. The gray and cyan markers indicate the clouds for mass below and above $5 \times 10^5\ M_\odot$. The black lines indicate the 16th, 50th, and 84th percentiles of $v_{\rm res}$ derived within binned $R_{\rm gal}$ of 24″ width, spaced by every 12″. (b) Estimated vertical velocity dispersion $<v_z>$ derived within the same binned $R_{\rm gal}$ as (a). Black and cyan solid lines indicate $<v_z>$ for the clouds below and above $5 \times 10^5\ M_\odot$. The dashed line indicates $<v_z>$ for the whole cloud masses. As $v_{\rm res}$ is severely affected by noncircular motions in the inner disk fo M83, $R_{\rm gal} < 100''$ is shaded. (c) p-values derived for the binned $R_{\rm gal}$ calculated with Levene's test, which indicate the statistical significance of the difference of $<v_z>$ between clouds with mass below and above $5 \times 10^5\ M_\odot$. The p-values below 3×10^{-3} are indicated as upper limits with the arrow markers. The dotted horizon line indicates the adopted threshold of 0.05. (d) Spatial distribution of $v_{\rm res}$, compared with the regional mask. (e) Same as (b), but comparing the difference between center/bar/arm and interarm regions shown with black and orange lines. (f) Same as (c), but comparing the difference between center/bar/arm and interarm regions.

marker colors show the elevation of $|v_{\rm res}|$ around spiral arms. The locations of the galactic structures identified in Section 3.3 are also shown for comparison.

Streaming motions around the bar and spiral arms are coherent and should show ordered patterns in this figure. While such coherent motions appear limited, there are still some signatures. For example, across the eastern, outermost armlike feature from the trailing to leading side, $v_{\rm res}$ changes from positive (red markers) to negative (blue markers).

Figure 10(e) is similar to Figure 10(b), but plots the radial variation of $<v_z>$ for clouds in the center/bar/arm region and the interarm regions using the spatial mask shown in Figure 10(d). Except for the innermost two radial bins, the dispersions within the bar/spiral arms and interarm regions are similar to each other. The p-values obtained with Levene's test (Figure 10(f)) also support their similarity. We here conclude that the arm-streaming motions have less impact on $v_{\rm res}$ than the mass dependence of the vertical cloud-to-cloud velocity dispersion at $R_{\rm gal} > 2.2$ kpc.

5.2.2. Comparison with Previous Studies

We identify a weak mass dependence of $<v_z>$, with $\sim$8.3 km s^{-1} and $\sim$11 km s^{-1} for clouds above and below $5 \times 10^5\,M_\odot$ at $R_{\rm gal}$ beyond 2.2 kpc. The former is close to the values found in other extragalactic studies at kiloparsec-scale resolutions (F. Combes & J.-F. Becquaert 1997; K. M. Mogotsi et al. 2016). The consistency with our study at $\sim$46 pc resolution may be because massive clouds occupy the dominant fraction of CO luminosity and also because our radial bin has a wide width of 24″ ($\sim$520 pc).

The smaller vertical velocity dispersion in more massive clouds ($>5 \times 10^5\,M_\odot$) is similar to the tendency for clouds in the solar neighborhood (A. A. Stark 1984). Massive clouds are scarce in the interarm regions, and thus, the reduced $v_{\rm res}$ dispersion in massive clouds suggests that clouds in spiral arms are likely more settled near the galactic plane than those in interarm regions. Such a trend is also observed in the Galactic plane (A. A. Stark & Y. Lee 2005) as the reduced scale height of clouds near the spiral arm.

6. Discussion

We identified 5724 molecular clouds from the ^{12}CO (1–0) data of M83 with a spatial resolution of $\sim$46 pc, and found a median $\alpha_{\rm vir}$ of 2.7 (Section 3.1) and a median Σ of $\sim$20 $M_\odot$ pc^{-2} assuming a Galactic CO-to-H2 conversion factor of 2.0×10^{20} cm^{-2} (K km s^{-1})$^{-1}$. Some of the recent cloud studies suggest that most molecular clouds are at most loosely bound by self-gravity, with $\alpha_{\rm vir}$ a factor of a few higher than 1 (M. H. Heyer et al. 2001; C. L. Dobbs et al. 2011; M17; J. Sun et al. 2020b; N. J. Evans et al. 2021) and also have a wide range of variation in Σ (M. H. Heyer et al. 2001; M17; C. J. Lada & T. M. Dame 2020; J. Sun et al. 2020b). At first glance, the median $\alpha_{\rm vir}$ and Σ agree with these recent results and suggestions. However, we take a step back to consider the possible impact of insufficient spatial resolution on the measured cloud properties. This assessment is needed because, while the median of the sampled cloud masses is $\sim 1.9 \times 10^5\,M_\odot$, the utilized $\sim$46 pc spatial resolution is larger than the sizes of the Galactic GMCs at a similar mass (e.g., $\sim$20 pc; D. B. Sanders et al. 1985).

We organize the discussion as follows. In Section 6.1, we discuss how the $\sim$46 pc beam affects cloud properties, in particular $\alpha_{\rm vir}$ and Σ, via a variation in the area-filling factor of clouds. Next, in Section 6.2, we argue the possible range of the area-filling factor and intrinsic cloud properties considering the sensitivity of the observational data. In Section 6.3, we discuss the implications of this section.

6.1. Impact of Sampling Clouds with a Relatively Large Beam

We consider the relations between intrinsic and observed parameters of the clouds affected by the effects of a limited resolution. When clouds are sampled with marginal resolution and SNR, measured cloud sizes could be overestimated even when the beam deconvolution (Section 2.3.1) is made (E. Rosolowsky & A. Leroy 2006). This overestimation would arise as a consequence of the SNR thresholding imposed during the cloud identification process, as only positive value pixels are included in cloud masks, and thus, the presence of noise tends to bias the measured cloud sizes toward larger values. For a cloud located in a crowded region, blending of emissions from the surrounding material also leads to the overestimation of cloud sizes. The observed distribution of $R_{\rm eff}$ appears to imply the sign of the overestimation of radii, as over 80% of the clouds have $R_{\rm eff}$ larger than 40 pc (Section 3.1.3), which is approximately the resolution limit.[24] The velocity dispersion $\sigma_{\rm v}$ could be similarly affected by the resolution bias, but the observed values of $\sigma_{\rm v}$ are well above the resolution limit Section 3.1.3, suggesting $\sigma_{\rm v}$ is less affected. Therefore, we consider that the resolution bias mostly affects $R_{\rm eff}$ for the M83 catalog. This is also supported by the bootstrap error estimation made in Section 2.3.1, which indicates significantly larger fractional uncertainties on $R_{\rm eff}$ than $\sigma_{\rm v}$.

From the nature of the data considered here, we assume that the beam dilution affects the observed cloud radius $R_{\rm eff}$ such that it overestimates the intrinsic radius R_0, but does not affect the velocity dispersion $\sigma_{\rm v}$. We also assume that cloud mass $M_{\rm cl}$ is unaffected. When observing a cloud with a larger beam, the cloud emission is diluted, and thus, the observed brightness temperature is lowered, but the luminosity, and hence cloud mass $M_{\rm cl}$, should be preserved to the first order.

Under the assumed simplified configuration, the relation between the observed and intrinsic radii is

$$R_{\rm eff} = f^{-1/2} R_0, \tag{18}$$

where f is the area-filling factor, the intrinsic-to-observed area ratio. By definition, f is $\leqslant 1$.

The cloud surface mass density Σ is affected by the beam dilution as it is dependent on $R_{\rm eff}$. The relation between the intrinsic Σ_0 and the observed Σ is

$$\Sigma = f\,\Sigma_0. \tag{19}$$

The virial parameter $\alpha_{\rm vir}$ depends on $R_{\rm eff}$ as $\alpha_{\rm vir} \propto R_{\rm eff}\sigma_{\rm v}^2$. Denoting the intrinsic value of $\alpha_{\rm vir}$ as $\alpha_{\rm vir,0}$, from Equations (7), (8), and (18), the relation between $\alpha_{\rm vir}$ and $\alpha_{\rm vir,0}$ is

$$\alpha_{\rm vir} = \alpha_{\rm vir,0} f^{-1/2}. \tag{20}$$

As f is $\leqslant 1$ by definition, $\alpha_{\rm vir}$ is elevated as $f^{-1/2}$. For example, suppose a bound cloud with $R_0 = 10$ pc and $\alpha_{\rm vir,0} = 1$. With a spatial resolution of $\sim$46 pc, f is $\sim$0.1, and thus, the observed $\alpha_{\rm vir}$ is elevated to $\sim$3.1, which would apparently indicate that the cloud is unbound even though its intrinsic $\alpha_{\rm vir,0}$ is 1.

Figure 11 shows the relationship between the observed $\alpha_{\rm vir}$ and Σ for the M83 clouds. The plot exhibits a solid declining trend of $\alpha_{\rm vir}$ toward higher Σ. This decline is consistent with the trend expected by a variation in f made by the beam dilution. We rewrite Equation (20) by casting Equation (19) to eliminate f:

$$\alpha_{\rm vir} = \alpha_{\rm vir,0}(\Sigma/\Sigma_0)^{-1/2}, \tag{21}$$

where $\Sigma \leqslant \Sigma_0$. If clouds share a combination Σ_0 and $\alpha_{\rm vir,0}$ similar to each other, their observed $\alpha_{\rm vir}$ should decrease as $\propto \Sigma^{-1/2}$. The dashed lines in Figure 11 show the expected variation of the observed $\alpha_{\rm vir}$ for clouds in a simple virial equilibrium ($\alpha_{\rm vir,0} = 1$) with three different Σ_0 of 40, 160, and 640 $M_\odot$ pc^{-2}. Most clouds are distributed along these lines, and moreover, over half of the clouds are located within a factor of

---

[24] As $R_{\rm eff}$ relates to rms cloud size σ_r as $R_{\rm eff} = 1.91\sigma_r$, the beam size $\theta_{\rm b}$ of 46 pc corresponds to $\sim$37 pc ($=1.91 \times \theta_{\rm b} / \sqrt{8 \log 2}$).

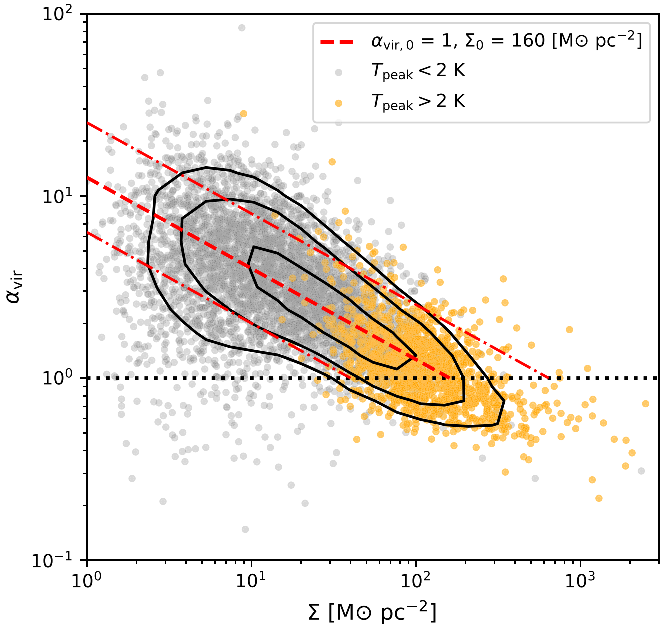

Figure 11. $\alpha_{\rm vir}$–Σ relationship for the clouds in M83. The contour lines indicate the density distribution of the data points at the levels of 0.2, 0.4, and 0.8, respectively. As in Section 3.2, the clouds with $T_{\rm peak} > 2$ K and <2 K are indicated with orange and gray markers, respectively. The black horizontal dotted line indicates $\alpha_{\rm vir}$ of 1. The red dashed line indicates the case in which the clouds are affected by the beam dilution, and they uniformly have the intrinsic $\alpha_{\rm vir,0}$ of 1 and Σ_0 of 160 $M_\odot$ pc^{-2}, and the two red dotted–dashed lines indicate the same but for a factor of 4 variations around it.

4 variations around $\Sigma_0 = 160\ M_\odot$ pc^{-2}. Notably, 160 $M_\odot$ pc^{-2} is close to the average surface density of 200 $M_\odot$ pc^{-2} implied from Larson's relations (S87; M. Heyer & T. M. Dame 2015).

A caveat is that the formulation made here is based on a crude approximation that the resolution effect mostly affects $R_{\rm eff}$, but not $\sigma_{\rm v}$ and $M_{\rm cl}$. In Appendix A, we verify this approximation with a source injection test.

The cloud distribution on the $\alpha_{\rm vir}$–Σ plane suggests that the intrinsic virial parameter and surface density may be more uniform than the observed $\alpha_{\rm vir}$ and Σ apparently tell. This also suggests the need to consider the effect of the beam dilution when interpreting the observed variations in $\alpha_{\rm vir}$ and Σ.

6.2. Distribution of Filling-factor and Intrinsic Cloud Properties

In the previous subsection, we showed that the observed spread of the virial parameter and surface mass density can be explained, at least partly, by the beam dilution. Their intrinsic $\alpha_{\rm vir,0}$ and Σ_0 are potentially more uniform than they appear from $\alpha_{\rm vir}$ and Σ. Here, we discuss the potential fraction of the clouds compatible with this possibility and estimate the distribution of intrinsic cloud properties. We address these questions by first defining a criterion to select clouds for which the discussion on the beam dilution effect is applicable in Section 6.2.1, and following in Section 6.2.2, we discuss the intrinsic cloud properties after the correction for *f*.

6.2.1. Criterion to Select Clouds for Filling-factor Estimation

In the previous subsection, we discussed the *f*-dependence of the observed cloud properties. Here, we crudely estimate *f* for each cloud by comparing the observed $\alpha_{\rm vir}$ with an assumed value of $\alpha_{\rm vir,0}$ using Equation (20). This procedure should apply only to clouds with a simple/single structure that can be approximated with a single temperature when observed at the current resolution and thus are describable with a single *f*.

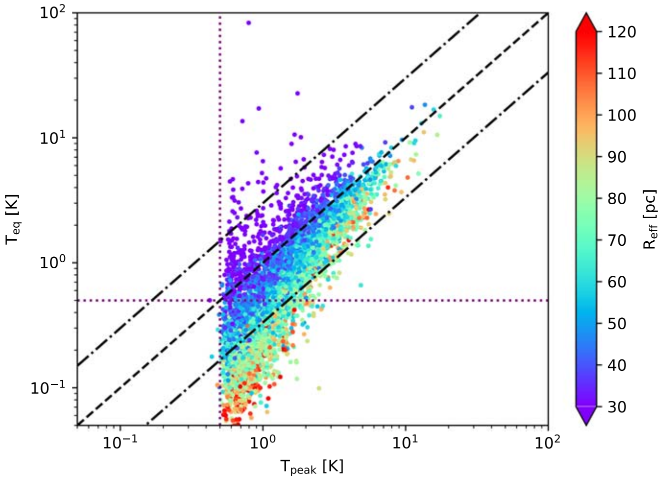

Figure 12. Equivalent peak temperature $T_{\rm eq}$, derived with Equation (22) as a function of peak temperature $T_{\rm peak}$ for the M83 clouds. Marker colors are coded to represent $R_{\rm eff}$. The dashed line indicates $T_{\rm eq} = T_{\rm peak}$, and the dashed–dotted lines indicate a factor of 3 variations. The vertical dotted line indicates $T_{\rm peak} = 0.5$ K, roughly the detection threshold of the clouds. The horizontal dotted line indicates the $T_{\rm eq}$ threshold of 0.5 K, adopted for selecting clouds for *f* estimation.

To select such clouds, we define a peak-equivalent temperature, or simply equivalent temperature, $T_{\rm eq}$. By using the cloud's CO luminosity $L_{\rm CO}$ and assuming a Gaussian spectral profile:

$$T_{\rm eq} = L_{\rm CO}/[\sqrt{2\pi}\,\sigma_{\rm v}(\pi R_{\rm eff}^2)]. \tag{22}$$

Note that if the line profile of a cloud is a single Gaussian (i.e., if the cloud's observed emission has a simple structure characterized by a single temperature), then $T_{\rm eq} \sim T_{\rm peak}$. As we adopted the 4σ detection threshold of $T_{\rm peak} \gtrsim 0.5$ K (Section 2.2), clouds that agree with the single-component approximation should have $T_{\rm eq} > 0.5$ K. Therefore, we adopt $T_{\rm eq} > 0.5$ K as a criterion to select clouds to estimate *f*.

We plot $T_{\rm eq}$ versus $T_{\rm peak}$ in Figure 12 with $R_{\rm eff}$ color-coded. Smaller clouds are closer to the line of $T_{\rm eq} = T_{\rm peak}$, and larger clouds deviate downward toward $T_{\rm eq} < T_{\rm peak}$. This trend is expected because smaller clouds are more likely to have a simple appearance when convolved by the beam The plot indicates that the clouds with $T_{\rm eq} > 0.5$ K mostly have $T_{\rm eq} \sim T_{\rm peak}$, although with modest deviations of up to a factor of 3, hinting that our criterion indeed selects the clouds that can be approximated with a single temperature under the current resolution.

6.2.2. Estimation of Intrinsic Cloud Properties

We estimate *f* for each cloud by casting an assumed value of $\alpha_{\rm vir,0}$ into Equation (20). We adopt two values of $\alpha_{\rm vir,0}$, 1 (virialized clouds) and 2 (loosely gravitationally bound clouds). If a cloud's $\alpha_{\rm vir}$ is less than the assumed $\alpha_{\rm vir,0}$, then *f* is capped at 1. Although this procedure allows us to derive *f* for all the clouds in M83, we regard the derived values of *f* to be "valid" only for clouds with $T_{\rm eq} > 0.5$ K, i.e., clouds that are compatible with the single-component approximation. The *f* values for clouds with $T_{\rm eq} < 0.5$ K are presented just for reference. We also note the derivation of *f* involves the assumptions of a constant CO-to-H_2 conversion factor and dominance of H_2 in the cloud masses.

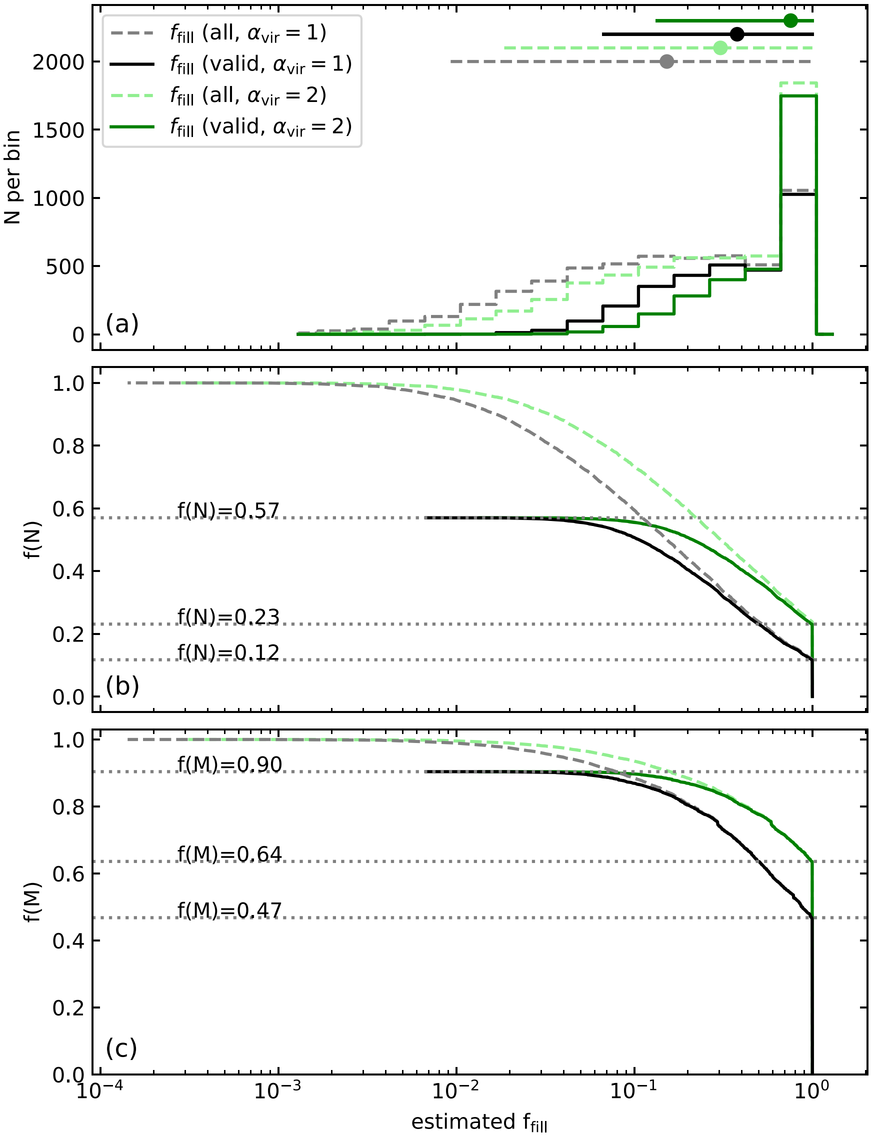

Figure 13. (a) Number distribution of the estimated area-filling factor f for the clouds in M83. The black and green lines show the distribution of f by assuming $\alpha_{\rm vir,0}$ of 1 and 2 for clouds that provide "valid" estimates, i.e., the clouds that satisfy the $T_{\rm eq} > 0.5$ K condition. The dashed gray and light green lines are the same as the black and green lines but for all the cloud samples. For each category shown here, the 16th-to-84th percentile range and 50th percentile are indicated with the horizontal line and the filled-circle marker, respectively. (b) Cumulative number distribution of the estimated f for the clouds. The colors and styles of the lines are the same as in (a). The dotted horizontal lines indicate the fraction number of clouds with "valid" estimates of f; about 12% (23%) of the clouds have $f = 1$ for the case of $\alpha_{\rm vir,0}$ of 1 (2), and about 56% of the clouds have "valid" estimate of f. (c) Same as (b), but showing as a cumulative fractional mass distribution.

Figure 13(a) shows the distribution of f. The solid lines indicate the "valid" f values derived from the clouds compatible with the single-component approximation by assuming $\alpha_{\rm vir,0} = 1$ (black) and 2 (green), respectively. As for the reference, the dashed lines indicate f for all clouds, which include "invalid" values derived from the clouds incompatible with the single-component approximation. Although the distribution of "valid" f extends down to ~0.01, it is chiefly between 0.1 and 1, as the 16th percentile is ~0.07 (~0.13) for $\alpha_{\rm vir,0}$ of 1 (2).

The minimum value of $f \sim 0.1$ is seemingly consistent with the detection limit of the clouds. For example, if we suppose a typical cloud with an intrinsic brightness temperature of 8 K, the observed peak brightness temperature would be 0.5 K if f is 0.1.[25] As our cloud-finding procedure adopted 0.5 K as the detection limit, it is consistent that the lower limit of the estimated f is around 0.1.

Figure 13(b) is the same as Figure 13(a) but shows in the cumulative number form. On the plot, the fractional number of clouds with $f = 1$ for a particular value of $\alpha_{\rm vir,0}$ indicates the fractional number of clouds with their observed $\alpha_{\rm vir}$ less than the adopted $\alpha_{\rm vir,0}$; about 12% (24%) of the clouds indicate $f = 1$ with $\alpha_{\rm vir,0}$ of 1 (2). Therefore, if the area-filling factor were not considered, we would be led to the conclusion that only a small number of clouds, less than about 20%, are gravitationally bound. However, contrary to this small fractional number, a majority of clouds (~57%) are compatible with the single-component approximation as $T_{\rm eq} > 0.5$ K. We saw that the f values estimated for such clouds by assuming $\alpha_{\rm vir,0}$ of 1 (or 2) are consistent with the sensitivity limit of the observation; therefore, we deduce that more than half of the clouds in number are potentially bound, i.e., $\alpha_{\rm vir,0} < 2$ if we accept a variation in f.

---

[25] In most parts within Taurus molecular cloud, which is one of the most well-studied molecular clouds, the intrinsic temperature is estimated to be between 6 and 12 (K P. F. Goldsmith et al. 2008).

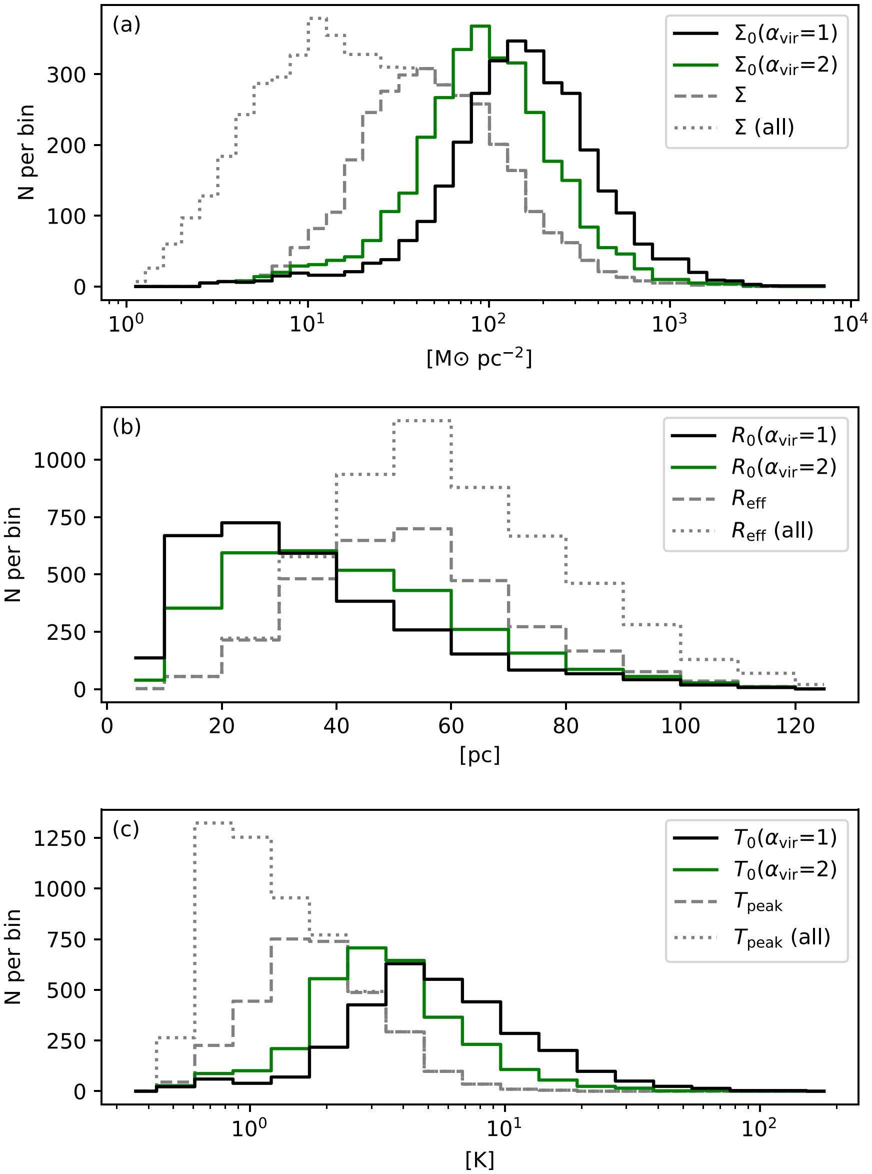

Figure 14. (a) Number distribution of cloud surface densities. The black and green lines indicate the estimated intrinsic Σ_0 by assuming $\alpha_{\rm vir,0}$ of 1 and 2 for clouds that provide "valid" estimates, i.e., the clouds that satisfy the $T_{\rm eq} > 0.5$ K condition. The dashed line indicates the observed (uncorrected) Σ for clouds that satisfy the condition of $T_{\rm eq} > 0.5$ K, and the dotted line is the same for all the clouds. (b) Same as (a), but for cloud radii, showing the intrinsic R_0 and the observed $R_{\rm eff}$. (c) Same as (a), but for cloud peak temperatures, showing the estimated intrinsic T_0 and the observed $T_{\rm peak}$.

The increase of the fraction of bound cloud by taking *f* into account is also prominent on a mass basis. Figure 13(c) shows the fractional cumulative mass distribution of *f*. About 47% (64%) of the clouds have the observed $\alpha_{\rm vir}$ less than 1 (2), as seen from the cloud numbers with $f = 1$. Allowing a change in *f*, most of the cloud mass (∼90%) is explainable as being bound.

The derived *f*, if they are correct, provide the intrinsic cloud properties. We derive Σ_0 and R_0 from Σ and $R_{\rm eff}$ using Equations (18) and (19). Also, we derive the intrinsic peak brightness temperature of cloud T_0 as

$$T_0 = T_{\rm peak} f^{-1}. \tag{23}$$

Figures 14(a)–(c) show the distributions of Σ_0, R_0, and T_0. In each panel, the solid line indicates the *f*-corrected estimates derived assuming $\alpha_{\rm vir,0} = 1$ (black) and 2 (green), respectively, for the nearly "single-component" clouds with $T_{\rm eq} > 0.5$ K. The uncorrected observed values, namely, Σ, $R_{\rm eff}$, and $T_{\rm peak}$, are also shown for the nearly "single-component" clouds and whole cloud samples with gray dashed and dotted lines, respectively.

Figure 14(a) shows that Σ_0 is in a narrow range. The median Σ_0 is ∼150 (∼90) for $\alpha_{\rm vir,0}$ of 1 (2), with a spread of ∼0.3 dex (1σ). These median and narrow ranges in Σ_0 are similar to the values derived by S87 for the Galactic GMCs. The estimation of the surface density is vastly different before the filling-factor correction: the uncorrected $\Sigma \sim 40\, M_\odot\,{\rm pc}^{-2}$ with a much wider spread.

Figures 14(b)–(c) show R_0 and T_0. The medians are $R_0 \sim 30$ pc (∼40 pc) and $T_0 \sim 3.7$ K (∼2.3 K) and for the assumed $\alpha_{\rm vir,0}$ of 1 (2). These values of R_0 and T_0 are similar to the typical radii and kinetic temperature (peak brightness temperature) of Galactic GMCs (D. B. Sanders et al. 1985), supporting the consistency of the filling-factor estimation.

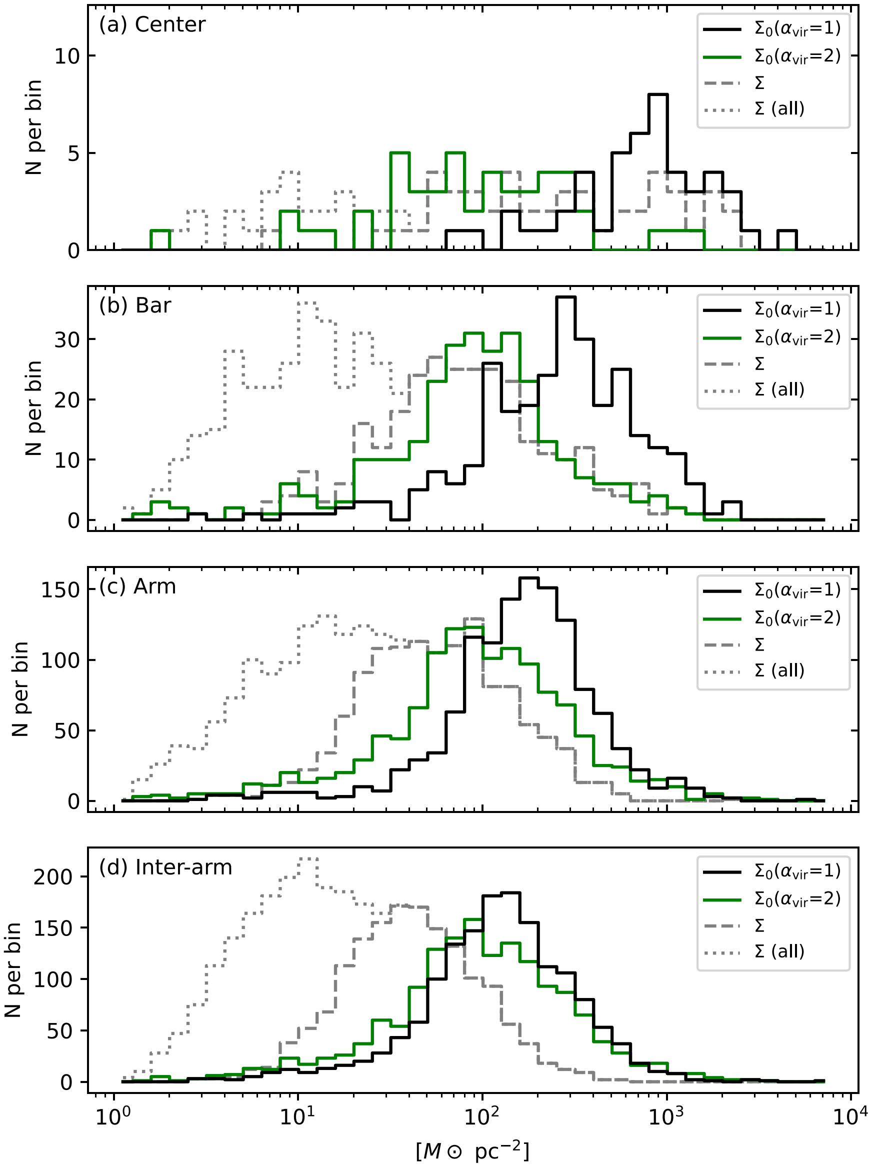

Figure 15. (a)–(d) Same as Figure 14(a), but showing for the central region, bar, arms, and interarm regions, respectively. The regional mask shown in Figure 7(c) is used for the classification.

We also show the environmental variation of Σ_0 in Figure (15). The environmental mask defined in Section 3.3 is used here. The medians in the arm and interarm regions are $\sim$170 ($\sim$96) $M_\odot\,\mathrm{pc}^{-2}$ and $\sim$120 ($\sim$95) $M_\odot\,\mathrm{pc}^{-2}$, respectively, for the assumed $\alpha_{\rm vir,0}$ of 1 (2). The 1σ scatter is only about 0.3 dex for each. In the bar and center regions, Σ_0 is elevated compared to the arm/interarm regions with medians of $\sim$270 $M_\odot\,\mathrm{pc}^{-2}$ and $\sim$770 $M_\odot\,\mathrm{pc}^{-2}$, respectively. Thus, the cloud properties vary depending on the environments; the interarm clouds have lower Σ_0, or higher $\alpha_{\rm vir,0}$, compared to the arm clouds, and the disk clouds have lower Σ_0 than the clouds in the central region.

Finally, we compare the filling-factor corrected intrinsic cloud properties with the uncorrected plain values on Larson's scaling relations. Figure 16(a) compares the corrected relationship, $\sigma_{\rm v}$–R_0, with the uncorrected $\sigma_{\rm v}$–$R_{\rm eff}$, and Figure 16(b) compares $M_{\rm cl}$–R_0 with $M_{\rm cl}$–$R_{\rm eff}$. The clouds with $T_{\rm eq} > 0.5$ K are shown, and we here assumed $\alpha_{\rm vir,0}$ of 1. From the near constancy of Σ_0 obtained by assuming a constant $\alpha_{\rm vir,0}$ (Figure 14), we would expect that the filling-corrected intrinsic cloud properties follow Larson's scaling relations, and both plots show that the expectation is the case. Figure 16 also plots the distribution density of S87's data points. M83's data points have a larger scatter than S87's points, for which the environmental variation of Σ_0 seen in Figure 15 should be at least partly responsible.

6.3. Implications

The observed $\alpha_{\rm vir}$ and Σ vary over wide ranges in the M83 clouds (Section 3.1). The wide range of variations in $\alpha_{\rm vir}$ and Σ agrees with some recent GMC studies (see references at the beginning of this section). However, we saw that the $\alpha_{\rm vir}$ and Σ in the M83 clouds are distributed approximately along the $\alpha_{\rm vir} \propto \Sigma^{-1/2}$ lines on the $\alpha_{\rm vir}$–Σ plane (Figure 11), which are exactly in the direction of the beam dilution (along the change of f). Within the limitations of the current data, it seems conceivable that a significant fraction of the clouds in M83 is

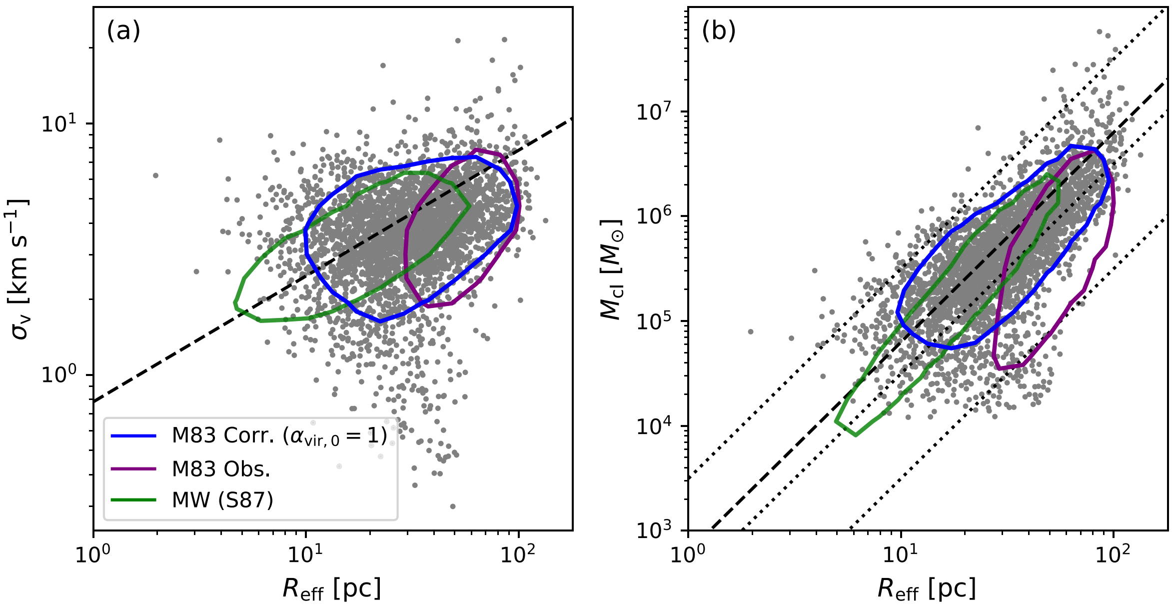

Figure 16. Scaling relations of cloud properties. In each plot, the filling-factor corrected data points for the M83 clouds are shown with the gray markers. The blue and purple contour lines indicate the data densities for the corrected and uncorrected cloud properties in M83 at the level of 20% of the maximum density for each. The green contour is the same for S87's Galactic samples. The correction for f is made by assuming $\alpha_{\rm vir,0}$ of 1, and only the clouds with $T_{\rm eq} > 0.5$ K are shown for M83 clouds. (a) Velocity dispersion to radius relationship. The dashed line indicates the σ_v–$R_{\rm eff}$ relation of S87. (b) Mass to radius relationship. The dashed line indicates $\Sigma = 200\ M_\odot$ pc^{-2}, the constant Σ implied from S87's scaling relations. Also, the dotted lines indicate the lines for Σ of 10, 100, and 1000 $M_\odot$ pc^{-2}, respectively.

consistent with those studied by S87, having $\alpha_{\rm vir} \sim 1$–2 and $\Sigma \sim 200\ M_\odot$ pc^{-2}, but being beam diluted with $f \sim 0.1$–1.0. Specifically, we found that a cloud population of up to ~57% in number and ~90% in mass are potentially in agreement with the intrinsic $\alpha_{\rm vir}$ of 1–2 (Figure 13), and the intrinsic Σ_0 is near-constant around the median of ~150 (~90) $M_\odot$ pc^{-2} with $\alpha_{\rm vir,0} = 1$ (2) for such clouds. Despite relatively large variations in Σ and $\alpha_{\rm vir}$ suggested in some of the recent studies, discrete and bound clouds with a high and near-constant Σ as suggested by Larson's relations might still be the dominant component in molecular disks.

The dependence of $\alpha_{\rm vir}$ and Σ on f gives a caveat when interpreting these observed parameters. The relation between the size-normalized velocity dispersion $\sigma_v/\sqrt{R_{\rm eff}}$ and Σ is often used to visualize the dynamical stabilities of clouds, including the impact of the confinement by external pressure (e.g., M. H. Heyer et al. 2001; G. B. Field et al. 2011; J. Sun et al. 2020a). For clouds with a constant $\alpha_{\rm vir}$, $\sigma_v/\sqrt{R_{\rm eff}}$ should scale as $\propto\Sigma^{1/2}$, but in Section 3.2, we saw that it scaled as with a shallow index, $\propto\Sigma^{\sim 0.3}$. The shallower index is explainable as the variation in f (Appendix B). In addition, some studies note the strong mass dependence of $\alpha_{\rm vir}$, which is mostly $\alpha_{\rm vir} \propto M_{\rm cl}^{-0.5}$ (M. Chevance et al. 2023 and references therein). At least for the M83 clouds presented here, the $\alpha_{\rm vir}$–$M_{\rm cl}$ scaling is also explainable by the beam dilution effect (Appendix C).

The fact that the distribution of the f-corrected Σ_0 has a narrow range around 100–200 $M_\odot$ pc^{-2} by assuming $\alpha_{\rm vir,0}$ of 1 (or 2) (Section 6.2) would imply that, in many, but not all, molecular clouds, the CO luminosity and mass are potentially concentrated at a bound component with high surface densities of around 100 $M_\odot$ pc^{-2}.

We note that the concentration of cloud mass to Σ of around 100 $M_\odot$ pc^{-2} and $\alpha_{\rm vir}$ of <2 is also similarly seen in the distribution of the cloud properties inspected in Section 3.1: despite that the intercloud median of Σ is as low as ~20 $M_\odot$ pc^{-2} and also that median $\alpha_{\rm vir}$ is 2.7, the mass-weighted averages of Σ of $\alpha_{\rm vir}$ are ~130 $M_\odot$ pc^{-2} and ~1.1, respectively (Section 3.1). This similarity would reinforce the implication that molecular gas material with high Σ, which is also strongly influenced by self-gravity, could be the dominant component of the molecular gas disk. It would also be of interest to investigate the internal distribution of Σ and $\alpha_{\rm vir}$ within individual clouds to see whether the concentration of CO luminosity to possibly gravitationally bound and high Σ components is a universal property of molecular clouds not only on intercloud scale scales but also on subcloud scales.

7. Summary

We identified molecular clouds over the whole disk of M83, with the ^{12}CO (1–0) data from ALMA (J. Koda et al. 2023). M83 is one of the closest molecular gas-rich spiral galaxies seen face-on, and it resembles the Milky Way in many aspects, including the existence of the stellar bar, multiple spiral arms, and its solar-like metallicity. At a resolution of ~46 pc and high-mass sensitivity of $\sim 10^4\ M_\odot$, we sampled 5724 clouds. By assuming a uniform CO-to-H$_2$ conversion factor of 2.0×10^{20} cm^{-2} (K km s^{-1})$^{-1}$, the median cloud mass is $\sim 2 \times 10^5\ M_\odot$ (Section 3.1), which is close to the median cloud mass found in the inner Galactic disk found by existing surveys (e.g., $\sim 8 \times 10^4\ M_\odot$; M17) and also close to the lower end of a conventional definition of GMC mass range (around $10^5\ M_\odot$; e.g., D. B. Sanders et al. 1985). This is a significant improvement because, even up to recently, molecular cloud studies that sample clouds in extragalactic disks beyond the Local Group were often made with a spatial resolution of 50–100 pc with a shallower sensitivity, with the median mass of sampled clouds being $\sim 10^6\ M_\odot$ or higher (e.g., D. Colombo et al. 2014; A. Hirota et al. 2018; E. Rosolowsky et al. 2021).

The overall distributions of the cloud properties are examined in Section 3.1.

1. The median cloud mass is $\sim 1.9 \times 10^5\ M_\odot$, and the mass-weighted mean cloud mass is $\sim 1.8 \times 10^6\ M_\odot$. The difference indicates that the CO luminosity and molecular gas mass of M83 are concentrated predominantly in massive clouds, similar to the MW disk's cloud population. Specifically, clouds more massive than $>10^6\ M_\odot$ are only $\sim$13% in cloud number but account for $\sim$65% of the total CO luminosity.
2. For a subset of clouds with a mass threshold of $10^6\ M_\odot$, which roughly corresponds to the ones sampled by the previous clouds studies in extragalactic molecular-rich disks, the median surface mass density Σ and virial parameter $\alpha_{\rm vir}$ are about 130 $M_\odot\ {\rm pc}^{-2}$ and 1.0, respectively.
3. Without any consideration of beam dilution, the observed median Σ and $\alpha_{\rm vir}$ are 22 $M_\odot\ {\rm pc}^{-2}$ and 2.7, respectively, for M83 clouds. The observed median Σ is much lower than that of the clouds of S87 (200 $M_\odot\ {\rm pc}^{-2}$; S87; M. Heyer & T. M. Dame 2015), but is comparable to those found in the recent Galactic studies, which extensively sampled clouds down to low-intensity threshold (M17; C. J. Lada & T. M. Dame 2020). Also, the observed median $\alpha_{\rm vir}$ is similar to the values found in recent extragalactic studies, including PHANGS (J. Sun et al. 2020b; E. Rosolowsky et al. 2021). However, we caution that the observed median values of $\alpha_{\rm vir}$ and Σ in M83 are potentially subject to the beam filling factor as discussed in Section 6.

The scaling relations of cloud properties (Section 3.2), spatial distributions (Section 3.3), mass distributions (Section 4), and cloud-to-cloud velocity dispersion (Section 5) are examined.

1. *Scaling relations*. The observed cloud properties are compared with the scaling relations of S87, namely, the velocity dispersion to size, virial mass to CO luminosity, and mass to size relationships. Although the $M_{\rm vir}$–$L_{\rm CO}$ relationship shows an apparent correlation with a correlation coefficient of 0.78, the signs of a correlation are hardly seen for the other two relations. Still, bright clouds selected with $T_{\rm peak} > 2$ K, which comprise about 20% of the clouds, are more aligned with Larson's relations.
2. *Normalized cloud velocity to surface mass density relation*. We see a correlation between the size-normalized velocity dispersion $\sigma_v/\sqrt{R_{\rm eff}}$ and Σ, which is expected for clouds influenced by self-gravity (M. Heyer et al. 2009; J. Ballesteros-Paredes et al. 2011). However, clouds with low Σ exhibit upward deviations, and the fitting of the data yielded $\sigma_v/\sqrt{R_{\rm eff}} \propto \Sigma^{0.3}$, which is shallower than $\propto\Sigma^{1/2}$ expected for bound clouds with a uniform $\alpha_{\rm vir}$.
3. *Spatial distribution of clouds*. Clouds more massive than $10^6\ M_\odot$ are strongly concentrated around bright galactic structures, such as the spiral arms, bar, and center. Smaller clouds are more prevalent in the interarm regions. We fitted the distributions of the massive clouds as logarithmic arms and produced a regional mask.
4. *Mass function*. Mass distributions of the identified clouds are examined and fitted with two functional forms: the power-law form, widely used in cloud studies, and a modified power law with exponential cutoff (Schechter-like form). The fit with the power-law form yields an index $\gamma_{\rm PL}$ of ~ -1.9, while the fit with the Schechter-like form yields $\gamma_{\rm exp}$ of ~ -1.5. Both forms provide the upper cutoff mass at around $\sim 8.0 \times 10^6\ M_\odot$. Radial variations of the mass distributions are also examined by dividing the galactic disks into five radial bins. Steepening of the slopes of mass functions is implied from the radial variations of $\gamma_{\rm PL}$, but not with $\gamma_{\rm exp}$.
5. *Cloud-to-cloud velocity dispersion*. Taking advantage of the face-on inclination of M83, the vertical cloud-to-cloud velocity dispersion is estimated. Outside of the central 2.2 kpc, the estimated vertical dispersion is $\sim 8.3\ {\rm km\ s^{-1}}$ and $\sim 11\ {\rm km\ s^{-1}}$ for clouds above and below $5 \times 10^5\ M_\odot$, respectively.

In Section 6, we discussed the possible impact of beam dilution on the cloud properties. In particular, the dependence of the observed values of virial parameter and surface density ($\alpha_{\rm vir}$ and Σ) on area-filling factor f was discussed.

1. The observed $\alpha_{\rm vir}$ and Σ are distributed approximately along $\alpha_{\rm vir} \propto \Sigma^{-1/2}$. As a hypothetical consideration, we suggest this tendency is explainable as the effect of beam dilution. If a cloud's beam-convolved emission distribution is simple enough to be approximated as a single component, the relations between the observed and intrinsic values are $\Sigma = f\,\Sigma_0$ and $\alpha_{\rm vir} = \alpha_{\rm vir,0}\, f^{-1/2}$.
2. We devised a temperature criterion to select clouds compatible with the single-component approximation, which is the prerequisite to assume the f-dependence of $\alpha_{\rm vir}$. For the selected clouds with the criterion, we estimated the values of f for each cloud by assuming that they are intrinsically bound with $\alpha_{\rm vir,0}$ of $\leqslant 2$ and found that f of the clouds is mostly between 0.1 and 1. In this way, up to $\sim$57% of the clouds in number, or $\sim$90% of the cloud masses in M83's disk, are compatible with the assumed $\alpha_{\rm vir,0}$. Also, the estimated intrinsic Σ_0 for such clouds is found to concentrate around 150 $M_\odot\ {\rm pc}^{-2}$ if the intrinsic $\alpha_{\rm vir,0}$ of 1 is assumed, or 90 $M_\odot\ {\rm pc}^{-2}$ if the intrinsic $\alpha_{\rm vir,0}$ of 2 is assumed. The combination of $\alpha_{\rm vir,0}$ and Σ_0 resembles the clouds found by S87, suggesting that such bound and discrete clouds are potentially the dominant component in an MW-type disk of M83.

Acknowledgments

We thank the anonymous referee for carefully checking the manuscript. This paper makes use of the following ALMA data: ADS/JAO.ALMA No. 2017.1.00079.S. ALMA is a partnership of ESO (representing its member states), NSF (USA), and NINS (Japan), together with NRC (Canada), MOST and ASIAA (Taiwan), and KASI (Republic of Korea), in cooperation with the Republic of Chile. The Joint ALMA Observatory is operated by ESO, AUI/NRAO, and NAOJ. The National Radio Astronomy Observatory is a facility of the National Science Foundation operated under cooperative agreement by Associated Universities, Inc. This research made use of `astrodendro`, a Python package to compute dendrograms of Astronomical data (http://www.dendrograms.org/). This research made use of APLpy, an open-source plotting package for Python (T. Robitaille & E. Bressert 2012; T. Robitaille 2019). F.E. is supported by JSPS KAKENHI grant No. 20H00172. L.C.H. was supported by the National Science Foundation of China (grant Nos. 11991052, 12011540375, and 12233001), the National Key R&D Program of China (grant No. 2022YFF0503401), and the China Manned

Space Project (grant Nos. CMS-CSST-2021-A04 and CMS-CSST-2021-A06). M.I.N.K. is supported by Grants-in-Aid from the Ministry of Education, Culture, Sports, Science, and Technology of Japan (grant No. JP22K14080).

Facility: ALMA.

Software: `astrodendro` (T. Robitaille et al. 2019), `scikit-image` (S. van der Walt et al. 2014), matplotlib (J. D. Hunter 2007), `emcee` (D. Foreman-Mackey et al. 2013).

Appendix A
Source Injection Test

The observed virial parameter $\alpha_{\rm vir}$ of the clouds in M83 exhibits a trend, which is approximately $\alpha_{\rm vir} \propto \Sigma^{-0.5}$ (Figure 11). In Section 6.1, we argued that this trend possibly owes to a variation in the area-filling factor, driven by the overestimation of cloud radius $R_{\rm eff}$ for clouds smaller than the beam. We assumed there that (1) the resolution effect overestimates $R_{\rm eff}$ but does not affect the velocity dispersion $\sigma_{\rm v}$ and mass $M_{\rm cl}$ of clouds, and that (2) the $R_{\rm eff}$ overestimation is coupled with the decrease of the area-filling factor of the beam (Equation (18)). We test these assumptions with a simulation test, which injects model sources with known properties into a portion of the data cube and samples the injected sources via the same identification procedure utilized in Section 2.

A.1. Procedure

The test is made with two setups. A ∼0.8 kpc^2 segment of M83 is used as the target field in both setups. Within the field, CO emission from M83 mostly resides within the LSR velocity range between 410 and 455 km s^{-1}. The two setups are configured with different velocity ranges as follows.

1. *Noise-only setup*. A CO emission-free velocity range of from 340 to 409 km s^{-1} is used. This setup is used to see the impact of the noise on the cloud property measurements.
2. *Blended setup*. The velocity range between 401 and 470 km s^{-1} is used to assess the combined impact of the noise and blending of CO emission surrounding the input sources.

Input model clouds are generated by assuming a Gaussian profile in both spatial and velocity directions. For each model cloud, $M_{\rm cl}$ is given as a parameter, and $R_{\rm eff}$ and $\sigma_{\rm v}$ are determined by setting $\alpha_{\rm vir}$ as 1.5 and Σ as 100 $M_\odot$ pc^{-2}, respectively. Five model clouds with $M_{\rm cl}$ of 0.5, 1, 2, 4, and 8×10^5 $M_\odot$ are generated and convolved to emulate the spatial resolution of ∼46 pc and velocity channel of 1 km s^{-1}. In each round of the test, the model clouds are injected into the random positions within the data cube with an imposed minimum spacing of 80 pc. For the *noise-only* setup, a constant receding velocity of 375 km s^{-1} is assigned to the clouds. For the *blended* setup, the receding velocity of each cloud is determined such that it is offset by 12 km s^{-1} from the median velocity of the existing CO emission around the cloud. The offset velocity of 12 km s^{-1} is comparable to the rms cloud-to-cloud velocity dispersion in the M83 clouds (Section 5). From the source-added data cube, clouds are identified using the procedure described in Section 2 and crossmatched with the input model clouds with a matching tolerance of half the FWHM cloud size in both spatial and velocity directions. The injection-identification sequence is repeated 40 times for each setup.

A.2. Simulation Results

Figures 17 and 18 show the test results for noise-only and blended setups, respectively. In the noise-only setup, the input sources are detected with high detection rates. The rate is 100%

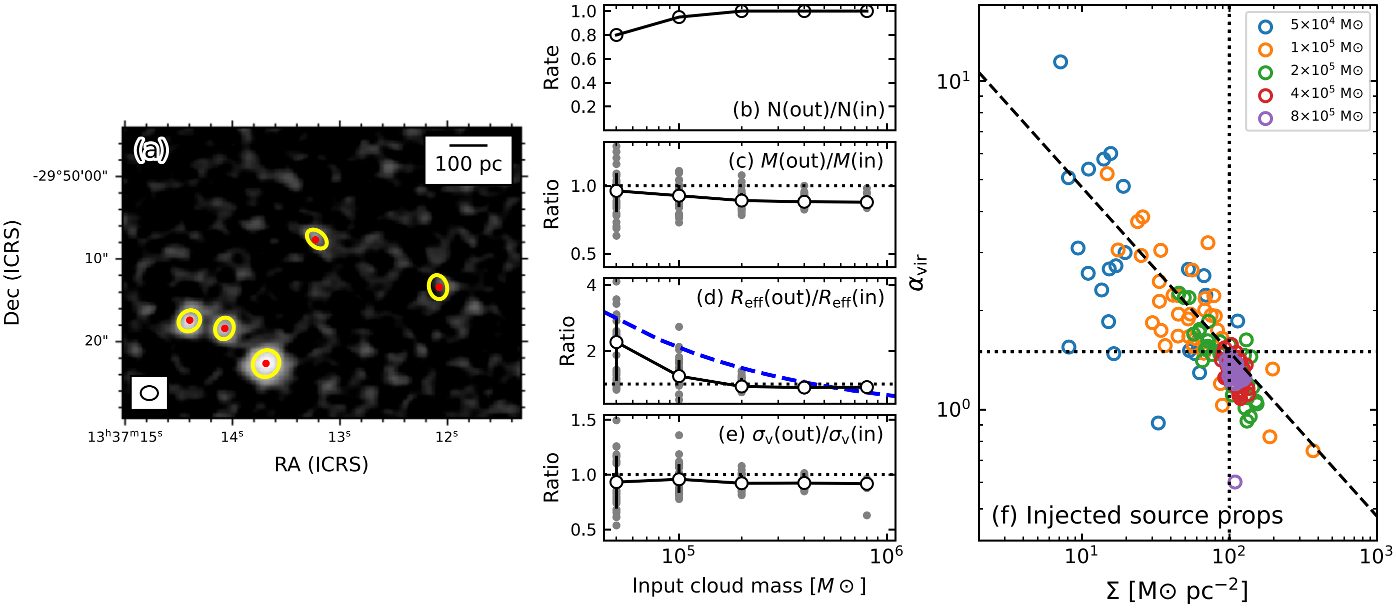

Figure 17. Simulation results of the source injection test made with the noise-only setup, which uses a CO emission-free portion of the data cube. (a) Integrated CO intensity image of the data used in one of the 40 rounds of the test. In the image, five sources with $M_{\rm cl}$ of 0.5, 1, 2, 4, and 8×10^5 $M_\odot$ are injected. The red dotted markers indicate the positions of the input sources. Yellow ellipses indicate the output FWHM sizes of the detected sources. (b) Detection rate as a function of the input $M_{\rm cl}$. (c) Output-to-input ratios of $M_{\rm cl}$ for the detected sources as a function of the input $M_{\rm cl}$. The black dotted horizontal line indicates the output-to-input ratio of 1. Gray dots indicate each of the detected clouds in each round. Open markers indicate the median output-to-input ratios for each input $M_{\rm cl}$ with error bars showing the 16th-to-84th percentiles range. (d) Same as (c), but for $R_{\rm eff}$. The blue dashed line indicates the line of $\theta_{\rm b}/\theta_{\rm source}$, where $\theta_{\rm b}$ and $\theta_{\rm source}$ are the FWHM sizes of the beam (∼46 pc) and the input model sources, respectively. (e) Same as (c), but for $\sigma_{\rm v}$. (f) $\alpha_{\rm vir}$–Σ relationship of the detected sources. The vertical and horizontal dotted lines indicate Σ of 100 $M_\odot$ pc^{-2} and $\alpha_{\rm vir}$ of 1.5 uniformly assigned to all the input sources. The dashed line indicates the relation of $\alpha_{\rm vir} \propto \Sigma^{-0.5}$.

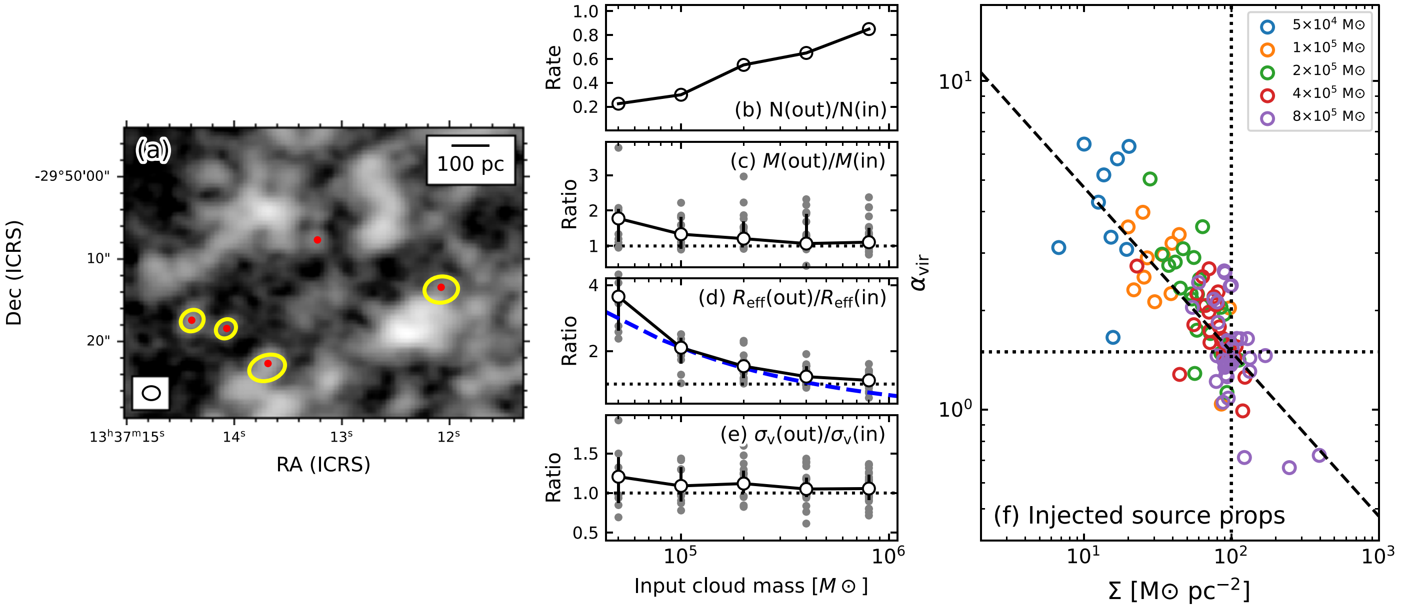

Figure 18. Same as Figure 17, but for the blended setup.

for the input $M_{\rm cl}$ of $>10^5\ M_\odot$ and slightly lowers to ~80% at $5\times10^4\ M_\odot$. These high recovery rates are in accordance with the minimum cloud mass of $\sim3\times10^4\ M_\odot$, estimated for uncrowded regions in Section 2.6. Figures 17(c), (d), and (e) show the ratios between the output-to-input values of $M_{\rm cl}$, $R_{\rm eff}$, and $\sigma_{\rm v}$. At the lower-mass range, $R_{\rm eff}$ shows a significant increase in the output-to-input ratio while the ratios for $M_{\rm cl}$ and $\sigma_{\rm v}$ are more stable around 1. Figure 17(f) shows the $\alpha_{\rm vir}$–Σ plot derived from the output properties of the detected sources. As a consequence of $R_{\rm eff}$ overestimation at lower $M_{\rm cl}$, a trend of $\alpha_{\rm vir}\propto\Sigma^{-0.5}$ appears despite the input sources uniformly having $\alpha_{\rm vir}$ of 1.5 and Σ of 100 $M_\odot$ pc^{-2}.

In the blended setup, the recovery rates are lower than the noise-only setup in all the mass ranges, with larger drops in smaller cloud masses. The rates are above 60% with input $M_{\rm cl}$ of $>2\times10^5\ M_\odot$, roughly in agreement with the effective completeness limit suggested from the cloud mass spectra Section 4. The trend of $R_{\rm eff}$ overestimation is more prominent in the blended setup (Figure 18(d)). In particular, the median output-to-input ratios of $R_{\rm eff}$ approximately follow the line of $\theta_{\rm b}/\theta_{\rm source}$ at lower $M_{\rm cl}$ of $<2\times10^5\ M_\odot$. The $\alpha_{\rm vir}$–Σ plot for the blended setup shown in Figure 18(f) again shows a trend in agreement with $\alpha_{\rm vir}\propto\Sigma^{-0.5}$ as in the noise-only setup.

As the CO emission widely prevails over the disk of M83, the blended setup would be more representative of the uncertainty trends in the M83 catalog than the noise-only setup. The blended setup indicates that the $R_{\rm eff}$ measurement tends to derive the beam size as the cloud size in crowded environments despite the beam size deconvolution. As the overestimated cloud size is comparable to the beam size, the intrinsic and observed cloud radii are associated with each other by the beam filling factor, as in Equation (18). In addition, the trend of $\alpha_{\rm vir}\propto\Sigma^{-0.5}$ seen with the model clouds with a uniform combination of $\alpha_{\rm vir}$ and Σ suggests that, to the first order, the impact of beam dilution on $\sigma_{\rm v}$ and $M_{\rm cl}$ is more moderate compared to $R_{\rm eff}$.

Appendix B

Filling-factor Dependence Seen in Size-normalized Velocity Dispersion to Surface Density Relation

The relation between the size-normalized velocity dispersion C ($\equiv\sigma_{\rm v}/\sqrt{R}$) and surface mass density Σ is often used to gauge the dynamical state of clouds (M. Heyer et al. 2009; J. Ballesteros-Paredes et al. 2011). As $M_{\rm vir}(\propto R\sigma_{\rm v}^2)=\alpha_{\rm vir}M_{\rm cl}$ is mathematically equivalent to $\sigma_{\rm v}^2/R\propto\alpha_{\rm vir}\Sigma$, clouds with a constant $\alpha_{\rm vir}$ should follow a line on the $\sigma_{\rm v}/\sqrt{R}$ - Σ plane following Equation (10).

We saw in Section 3.2 that a majority of the M83 clouds are located upward of the line expected for $\alpha_{\rm vir}=1$ on the $\sigma_{\rm v}/\sqrt{R}$–Σ plot. The clouds with such upward deviations are often considered to be confined by external pressure (M. Heyer et al. 2009; G. B. Field et al. 2011; J. Sun et al. 2020a), but we also saw that the deviations are rather systematic; the fitted relation indicated that $\sigma_{\rm v}/\sqrt{R}$ varies as $\propto\Sigma^{\sim0.3}$ (Equation (12)), although $\Sigma^{1/2}$ is expected for a constant value of $\alpha_{\rm vir}$ (Equation (10)).

The observed index of ~0.3 for the $\sigma_{\rm v}/\sqrt{R}$–Σ relation is explainable with the beam dilution effect if a significant fraction of the clouds share a similar set of combinations of the intrinsic virial parameter and surface mass density. Consider a cloud with intrinsic radius R_0, surface mass density Σ_0, virial parameter $\alpha_{\rm vir,0}$, and velocity dispersion $\sigma_{\rm v}$. As we assume the beam dilution does not affect the velocity dispersion, $\sigma_{\rm v}$ does not have a subscription. If the cloud follows Larson's relations, the following applies to the cloud:

$$\sigma_{\rm v}/\sqrt{R_0}=\left(\frac{2}{9}\alpha_{\rm vir,0}G\pi\Sigma_0\right)^{1/2}. \tag{B1}$$

The observed cloud radius $R_{\rm eff}$ and surface mass density Σ are related to R_0 and Σ_0 with Equations (18) and (19), respectively. Substituting them into Equation (B1), we obtain

$$\sigma_{\rm v}/\sqrt{R_{\rm eff}}=\left(\frac{2}{9}\alpha_{\rm vir,0}G\pi\right)^{1/2}(\Sigma_0\Sigma)^{1/4}. \tag{B2}$$

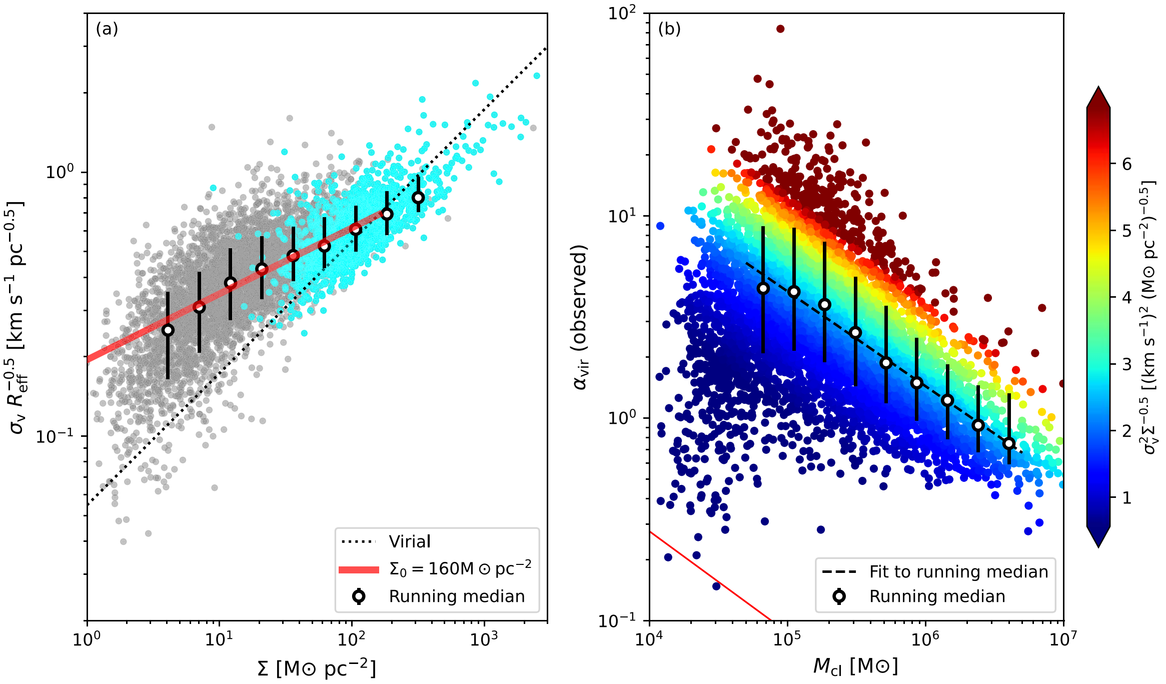

Figure 19. (a) $\sigma_v/\sqrt{R_{\rm eff}}$–$\Sigma$ relationship for clouds in M83. Cyan and gray markers indicate the clouds with $T_{\rm peak}$ above and below 2 K, respectively. White circle markers with black outline indicate the running median of $\sigma_v/\sqrt{R_{\rm eff}}$–$\Sigma$. The dotted line indicates a state of virial equilibrium, $\alpha_{\rm vir} = 1$. The red thick line shows the expected range of variation for clouds that have $\alpha_{\rm vir} = 1$ and a constant intrinsic surface density Σ_0 of 160 $M_\odot$ pc^{-2} but are affected by the beam dilution with f of <1. (b) $\alpha_{\rm vir}$–$M_{\rm cl}$ relationship for clouds in M83. The running median of $\alpha_{\rm vir}$ and fitted to the median values are displayed similarly to (a). The red line indicates the minimum $\alpha_{\rm vir}$ expected from Equation (C1) by setting $\sigma_{\rm v}$ to be $1\ /\ \sqrt{12}$ km s^{-1}, which is the instrumental limit of the data, and $T_{\rm peak}$ of 0.5 K, which is the near the detection limit of the clouds. Most clouds are located well above the line, indicating that the velocity resolution is not driving the observed $M_{\rm cl}$-dependence of $\alpha_{\rm vir}$. The marker colors are coded to express the variation in $\sigma_{\rm v}^2/\Sigma^{1/2}$.

The equation postulates that, if $\alpha_{\rm vir,0}$ and Σ_0 are constant, the scaling between the observed coefficient, $\sigma_v/\sqrt{R_{\rm eff}}$, is proportional to $\Sigma^{1/4}$, which is similar to the observed relation of $\sigma_v/\sqrt{R_{\rm eff}} \propto \Sigma^{\sim 0.3}$.

Figure 19(a) shows the $\sigma_v/\sqrt{R_{\rm eff}}$–$\Sigma$ relation for the M83 clouds. The red line on the plot is the expected behavior of Equation (B1) in the case of $\alpha_{\rm vir,0}$ of 1 and Σ_0 of 160 $M_\odot$ pc^{-2} for a range of filling factor between 0.1 and 1, showing an alignment with the running median of the observed $\sigma_{\rm v}/R_{\rm eff}$.

Appendix C
Filling-factor Dependence Seen in Virial Parameter to Mass Relation

Some studies of molecular clouds, including this one, noted that $\alpha_{\rm vir}$ varies as $\propto M_{\rm cl}^{\sim -0.5}$ in their samples (M. H. Heyer et al. 2001; M17; also see references in M. Chevance et al. 2023). Figure 19(b) shows the $\alpha_{\rm vir}$–$M_{\rm cl}$ relation for the M83 clouds. The running-median values of $\alpha_{\rm vir}$ derived within the binned $M_{\rm cl}$ values are also shown, and fit the running-median values yield that $\alpha_{\rm vir} \propto M_{\rm cl}^{-0.45}$, which is close to the $\alpha_{\rm vir} \propto M_{\rm cl}^{\sim -0.5}$ seen in other studies quoted here.

M. H. Heyer et al. (2001) pointed out that a relation of $\alpha_{\rm vir} \propto M_{\rm cl}^{-0.5}$ could arise due to a limited velocity resolution; the argument of M. H. Heyer et al. (2001) is as follows. From Equations (7) and (8), $\alpha_{\rm vir} = (9/2) R_{\rm eff}\,\sigma_{\rm v}^2 (G\,\alpha_{\rm CO} L_{\rm CO})^{-1}$, where $\alpha_{\rm CO}$ is the mass-to-luminosity conversion factor for the CO line. Combining this with $L_{\rm CO} \simeq \sqrt{2\pi}\,T_{\rm peak}\,\sigma_{\rm v}\,R_{\rm eff}^2$ to eliminate $R_{\rm eff}$, one obtains

$$\alpha_{\rm vir} = 178\left(\frac{\alpha_{\rm CO}}{4.4M_\odot/({\rm K\ km\ s^{-1}pc^2})}\right)^{-1/2} \times \left(\frac{\sigma_{\rm v}}{\rm km\ s^{-1}}\right)^{3/2}\left(\frac{T_{\rm peak}}{\rm K}\right)^{-1/2}\left(\frac{M_{\rm cl}}{M_\odot}\right)^{-1/2}. \quad ({\rm C1})$$

Many clouds in the samples of M. H. Heyer et al. (2001) have $\sigma_{\rm v}$ close to the instrumental resolution limit. Substituting the instrumental limit of $\sigma_{\rm v}$ and the typical temperature of the clouds observed, M. H. Heyer et al. (2001) demonstrated that the above relation explains the lower envelope of their samples on the $\alpha_{\rm vir}$–$M_{\rm cl}$ plot.

An argument similar to M. H. Heyer et al. (2001) would hold for the M83 cloud samples, but not in exactly the same way because $\sigma_{\rm v}$ of the clouds is well above the velocity resolution of the data (Section 3.1). The red line in Figure 19(b) shows that the minimum $\alpha_{\rm vir}$ expected by Equation (C1) is far below the observed data points. In turn, we consider that the $\alpha_{\rm vir} \propto M_{\rm cl}^{-1/2}$ relation is related to the limitation in the spatial resolution.

The marker colors in Figure 19(b) are coded to represent the value of $\sigma_{\rm v}^2/\sqrt{\Sigma}$, which is dimensionally equal to $\sigma_{\rm v}^{3/2} T_{\rm peak}^{-1/2}$ as $\Sigma \propto T_{\rm peak}\sigma_{\rm v}$. From the distribution of the data points, it is apparent $\sigma_{\rm v}^2/\Sigma^{1/2}$ is almost constant along the direction of $\alpha_{\rm vir} \propto M_{\rm cl}^{-1/2}$. We may rewrite Equation (B2) as

$$\sigma_{\rm v}^2/\sqrt{\Sigma} \propto \sqrt{\Sigma_0}\,R_{\rm eff}. \quad ({\rm C2})$$

As seen in Section 3.1, the observed $R_{\rm eff}$ indeed has a limited range of variation, with 16th and 84th percentiles of 40 and 80 pc, respectively. We argued in Section 6 that, once the beam dilution is taken into account, a majority of the clouds agree with $\alpha_{\rm vir}$ of 1 (or 2) with near uniform Σ_0. Therefore, when we assume that near-virial clouds with almost constant Σ_0 account for the dominant fraction of the M83 clouds as suggested in Section 6, Equation (C2) leads that $\sigma_{\rm v}^2/\sqrt{\Sigma}$, which has the same dimension as $\sigma_{\rm v}^{3/2} T_{\rm peak}^{-1/2}$, would also be constant, and thus, $M_{\rm vir} \propto M_{\rm cl}^{\sim 0.5}$ emerges from Equation (C1).

Appendix D
Comparison of Galactic Cloud Catalogs

In Section 3.2, the clouds in M83 are compared with the scaling relations of S87, which have been used as the reference lines up to now. The scaling relations of S87 are determined from 273 clouds sampled from the inner Galactic disk with relatively high-intensity thresholds of a few to several Kelvin, but subsequent studies made a more extensive sampling of clouds down to lower-intensity levels. In particular, R16 and M17 sampled clouds from the Galactic plane data of T. M. Dame et al. (2001), which observed most part of the thin Galactic molecular disk in ^{12}CO (1–0) with the 1.2 m telescopes. Here, we extend the examination made in Section 3.2 by including clouds in the R16 and M17 catalogs.

D.1. Catalogs for Comparison

The R16 catalog contains 1064 clouds with a total cloud mass of $2.5 \times 10^8\ M_\odot$, and the M17 catalog lists 8107 clouds with a total mass of $1.2 \times 10^9\ M_\odot$. The M17 catalog sampled 98% of the total CO luminosity within the mapped area. To compare the M83 clouds with the Galactic clouds at similar environmental conditions, we use the clouds with the Galactocentric radius within 8.5 kpc for the Galactic catalogs. Both M83 and the Milky Way have radially decreasing trends of the molecular fraction $f_{\rm mol}$ ($\equiv \Sigma_{\rm mol}$ / ($\Sigma_{\rm mol}$ + $\Sigma_{\rm atom}$)). In M83, $f_{\rm mol}$ is about 0.5 at the edge of the mapped area (L. P. Crosthwaite et al. 2002; A. M. Lee et al. 2024). In the Milky Way, it is about 0.1 at $R_{\rm gal}$ of 8.5 kpc (H. Nakanishi & Y. Sofue 2016).

For the R16 catalog, we take the radius R, velocity dispersion $\sigma_{\rm v}$, and cloud mass $M_{\rm cl}$ from the catalog. The cloud radius in R16 follows the same definition as S87. Therefore, R in the R16 catalog can be directly compared with $R_{\rm eff}$ of the M83 clouds and S87 clouds. CO luminosity $L_{\rm CO}$ of the R16 clouds is computed from $M_{\rm cl}$ assuming the same conversion factor as in Section 2.6. The surface density Σ and virial parameter $\alpha_{\rm vir}$ are derived following Equations (6) and (8).

For the M17 catalog, the velocity dispersion σ_v, surface density Σ, and cloud mass $M_{\rm cl}$ are taken from the catalog. We compute the effective radius of M17 clouds as $R_{\rm eff}$= $[M(\pi\Sigma)^{-1}]^{1/2}$. For $L_{\rm CO}$ and $\alpha_{\rm vir}$, they are derived in the same way as the R16 clouds.

D.2. Comparison

Figure 20 compares the scaling relations of cloud properties among the M83 catalog and the Galactic cloud catalogs of S87, R16, and M17. For the MW catalogs, we divide the clouds into two groups with a kinematic distance $D_{\rm kin}$ threshold of 8.5 kpc. The upper and bottom rows of Figure 20 show the Galactic clouds at $D_{\rm kin} < 8.5$ kpc and >8.5 kpc, respectively. In both rows, the MW clouds with $R_{\rm gal} > 8.5$ kpc are excluded, as mentioned above. In addition, we excluded the clouds with Galactic longitude l within $|l| < 5°$ to exclude the clouds located in the directions close to the GC because the GC clouds have properties distinct from the disk clouds (e.g., T. Oka et al. 2001), and such clouds are contained only in the M17 catalog among the three catalogs. Table 5 lists the 16, 50, and 84 percentiles of the cloud properties for the three Galactic catalogs classified with the same criteria as Figure 20. We note that the R16 and M17 catalogs contain clouds in the outer Galactic disk, which have lower Σ and higher $\alpha_{\rm vir}$ than the inner Galactic clouds (M. H. Heyer et al. 2001). The last three rows in Table 5 list the cloud properties in the three catalogs without any filtering.

D.2.1. R16 Catalog

Comparing the R16 and S87 clouds, the R16 clouds mostly follow scaling relations similar to that of S87, with a slight modification in coefficients. The coefficients of the cloud scaling relations are determined by Σ and $\alpha_{\rm vir}$. As can be seen from Table 5, the R16 clouds have a median Σ, a factor of 3 lower than that of S87, but the median $\alpha_{\rm vir}$ is comparable. Because of the comparable $\alpha_{\rm vir}$, clouds in both catalogs show a similar scaling on the $M_{\rm vir}$–$L_{\rm CO}$ plot and $\sigma_{\rm v}/\sqrt{R_{\rm eff}}$–$\Sigma$ plots. On the $\sigma_{\rm v}$–$R_{\rm eff}$ plot, the R16 clouds indicate a smaller $\sigma_{\rm v}$ at given $R_{\rm eff}$ compared to S87. R16 determined the $\sigma_{\rm v}$–$R_{\rm eff}$ scaling in the inner Galactic disk to be $\sigma_{\rm v} = 0.50\ R_{\rm eff}^{0.52}$. The coefficient value of 0.50 km s^{-1} pc$^{-1/2}$ is slightly smaller than for S87, 0.72 km s^{-1} pc$^{-1/2}$ (S87; M. Heyer et al. 2009). Considering the factor of 2 differences in the median Σ, this difference in the $\sigma_{\rm v}$–$R_{\rm eff}$ coefficient value agrees with the Σ-dependence of the $\sigma_{\rm v}$–$R_{\rm eff}$ coefficient for bound clouds (Equation (10)).

In Section 3.2, the M83 clouds with $T_{\rm peak} > 2$ K mostly follow the scaling relations of S87. As R16 and S87 clouds follow similar scaling relationships, the argument in Section 3.2 would not change if the R16 clouds were taken as reference samples instead of the S87 clouds.

D.2.2. M17 Catalog

At $D_{\rm kin} > 8.5$ kpc, the M17 clouds cover a range of $R_{\rm eff}$ similar to that of the M83 clouds as median $R_{\rm eff}$ is similarly around 50 pc. However, despite the similar radii, there is quite a small overlap with that of M83 clouds on the $\sigma_{\rm v}$–$R_{\rm eff}$, $M_{\rm vir}$–$L_{\rm CO}$, and $\sigma_{\rm v}/\sqrt{R_{\rm eff}}$–$\Sigma$ plots (Figures 20(e), (f), (h)). The small overlap in these plots suggests that the M83 clouds cannot be deemed as the simple counterparts of the M17 clouds sampled in another galactic disk.

The small overlap between the M17 and M83 clouds owes to higher $\alpha_{\rm vir}$ in the M17 clouds compared to other Galactic catalogs. In particular, even though M17 and R16 sampled clouds from similar data sets of T. M. Dame et al. (2001), M17 clouds have about a factor 4 higher $\alpha_{\rm vir}$ compared to the R16 clouds. The high $\alpha_{\rm vir}$ in the M17 clouds is linked to the higher $\sigma_{\rm v}$ at a given $R_{\rm eff}$ compared to the R16 clouds, seen on the $\sigma_{\rm v}$–$R_{\rm eff}$ relation (Figures 20(a), (e)). The reason for this systematically higher $\sigma_{\rm v}$ in the M17 clouds compared to the R16 clouds is not completely clear, but it might reflect the difference in the ways clouds are identified , as also was suggested by N. J. Evans et al. (2021). M17 identified clouds by decomposing each spectrum of the data cube into a set of

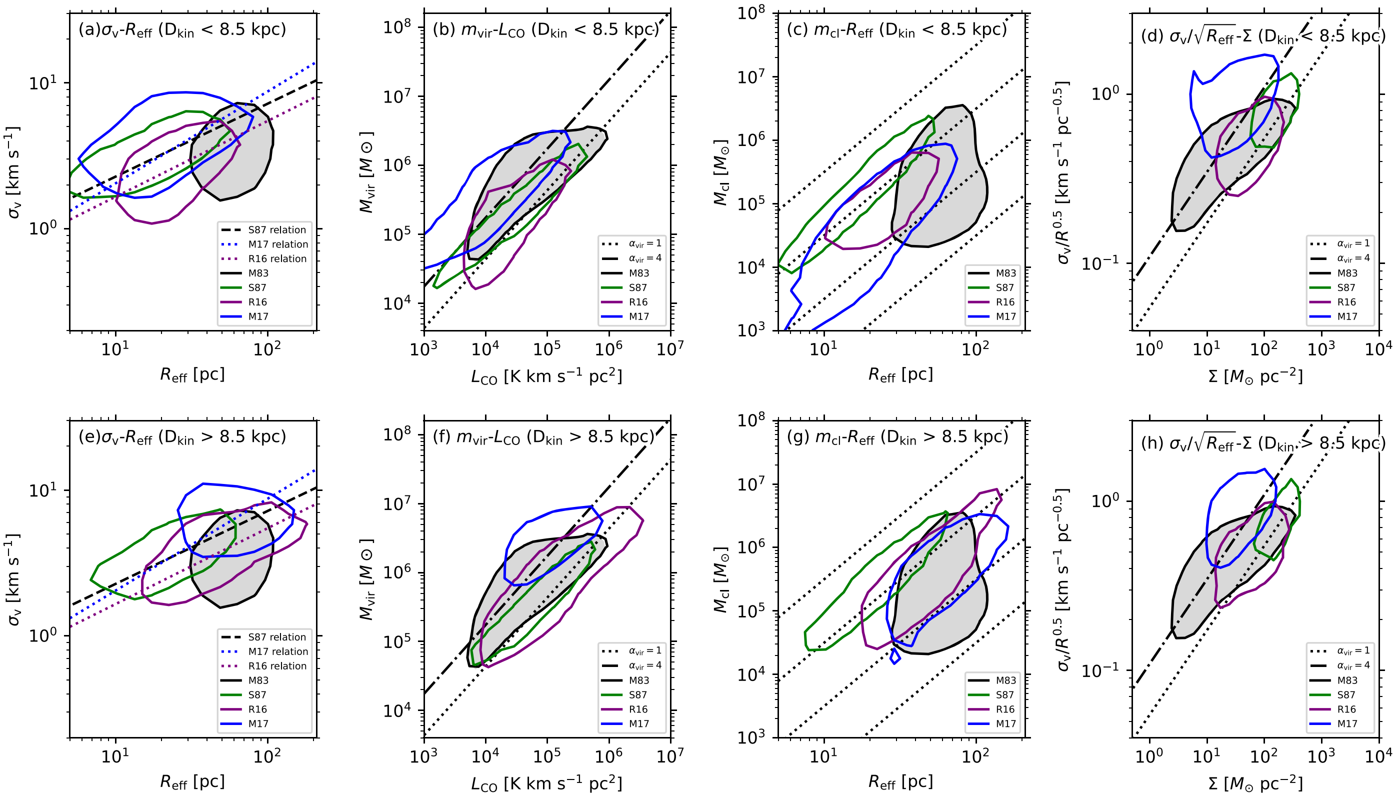

Figure 20. Scaling relations of cloud properties. In each plot, the density distribution of the clouds at the 20% level of the maximum density is shown for M83 clouds with the black contour and for the Galactic clouds of S87, R16, and M17 with green, purple, and blue contours, respectively. For the Galactic catalogs of S87, R16, and M17, we excluded the clouds with the Galactocentric of $R_{\rm gal} > 8.5$ kpc and the Galactic longitude l within $|l| < 5°$. The former filtering is made to compare clouds among molecular-dominated environments, as in the disk of M83. The latter is to exclude the Galactic Center clouds. In the top and bottom rows, the Galactic clouds with the kinematic distance at $D_{\rm kin} < 8.5$ kpc and $D_{\rm kin} > 8.5$ kpc are shown, respectively. (a), (e) σ_v–$R_{\rm eff}$ relationship. The black dashed line indicates the σ_v–$R_{\rm eff}$ relation of S87, which is Equation (9) with $C = 0.72$ km s^{-1} pc$^{-1/2}$. The purple and blue dotted lines indicate the relations reported in R16 and M17, respectively. (b), (f) $M_{\rm vir}$–$L_{\rm CO}$ relationship. The dotted and dashed–dotted lines indicate $\alpha_{\rm vir}$ of 1 and 4, respectively. (c), (g) $M_{\rm cl}$–$R_{\rm eff}$ relationship. The dotted lines indicate the lines for Σ of 1, 10, 100, and 1000 $M_\odot$ pc^{-2}, respectively. (d), (h) $\sigma_v/R_{\rm eff}^{1/2}$–Σ relationship. The dotted and dashed–dotted lines indicate $\alpha_{\rm vir}$ of 1 and 4, respectively.

Table 5
Median Cloud Properties in the MW Catalogs

Catalog Name (1)	$R_{\rm eff}$ (pc) (2)	$M_{\rm cl}$ (10^5 $M_\odot$) (3)	Σ ($M_\odot$ pc^{-2}) (4)	σ_v (km s^{-1}) (5)	$\alpha_{\rm vir}$ (6)	N (7)
S87 ($D < 8.5$ kpc, $R_{\rm gal} < 8.5$ kpc, $\|l\| > 5°$)	$14.3_{8.2}^{27.9}$	$1.0_{0.2}^{4.7}$	$152.2_{100.2}^{236.8}$	$3.1_{2.3}^{4.3}$	$1.4_{0.9}^{2.1}$	166
S87 ($D > 8.5$ kpc, $R_{\rm gal} < 8.5$ kpc, $\|l\| > 5°$)	$26.8_{17.3}^{45.0}$	$4.8_{1.9}^{11.1}$	$194.5_{142.6}^{288.2}$	$3.9_{3.0}^{5.0}$	$1.0_{0.7}^{1.4}$	62
R16 ($D < 8.5$ kpc, $R_{\rm gal} < 8.5$ kpc, $\|l\| > 5°$)	$24.0_{15.5}^{40.6}$	$0.8_{0.4}^{3.0}$	$53.8_{25.9}^{102.9}$	$2.5_{1.7}^{3.7}$	$1.5_{0.8}^{3.0}$	324
R16 ($D > 8.5$ kpc, $R_{\rm gal} < 8.5$ kpc, $\|l\| > 5°$)	$47.4_{26.5}^{78.8}$	$4.2_{1.0}^{13.1}$	$67.8_{25.8}^{120.4}$	$3.3_{2.3}^{5.1}$	$1.3_{0.7}^{2.9}$	118
M17 ($D < 8.5$ kpc, $R_{\rm gal} < 8.5$ kpc, $\|l\| > 5°$)	$19.8_{9.4}^{37.0}$	$0.4_{0.0}^{1.9}$	$28.8_{7.6}^{75.2}$	$4.0_{2.3}^{5.9}$	$6.8_{3.2}^{35.0}$	2893
M17 ($D > 8.5$ kpc, $R_{\rm gal} < 8.5$ kpc, $\|l\| > 5°$)	$60.3_{36.7}^{95.7}$	$4.1_{1.3}^{12.4}$	$32.7_{15.4}^{75.9}$	$6.4_{4.5}^{8.2}$	$5.4_{2.9}^{14.9}$	1177
S87 (Full)	$17.0_{8.0}^{31.9}$	$1.3_{0.2}^{6.3}$	$152.6_{92.8}^{250.5}$	$3.1_{2.2}^{4.4}$	$1.3_{0.8}^{2.1}$	273
R16 (Full)	$27.6_{15.4}^{53.6}$	$0.5_{0.1}^{3.0}$	$22.1_{8.6}^{76.7}$	$2.1_{1.3}^{3.5}$	$2.3_{1.1}^{5.2}$	1064
M17 (Full)	$26.4_{9.0}^{60.4}$	$0.4_{0.0}^{3.2}$	$16.5_{4.9}^{60.0}$	$3.6_{1.8}^{6.5}$	$8.0_{3.2}^{34.0}$	8107

Note. Median and 16th-to-84th percentile range of the cloud properties for the Galactic cloud catalogs of P. M. Solomon et al. (1987), T. S. Rice et al. (2016), and M.-A. Miville-Deschênes et al. (2017). In the first six rows, the clouds with the Galactocentric of $R_{\rm gal} > 8.5$ kpc and the Galactic longitude l within $|l| < 5°$ are excluded, and the remaining clouds are classified by the line-of-sight distance threshold of 8.5 kpc. In the last three rows, the full sample summaries for the catalogs are listed. Column (1): catalog name and $D_{\rm kin}$ range. Column (2): effective radius. Column (3): cloud mass. Column (4): surface density. Column (5): velocity dispersion. Column (6): virial parameter. Column (7): number of clouds.

Gaussian components and then clustering the Gaussian components into clouds, while the methods used by S87, R16, and here in M83 are similar in that cloud peaks are identified by setting intensity thresholds. The clustering process of M17 accepts the joining of two clusters of Gaussian components at different velocities if the velocity difference between the two clusters is less than twice the velocity dispersion of individual clusters.

ORCID iDs

Akihiko Hirota https://orcid.org/0000-0002-0465-5421
Jin Koda https://orcid.org/0000-0002-8762-7863
Fumi Egusa https://orcid.org/0000-0002-1639-1515
Tsuyoshi Sawada https://orcid.org/0000-0002-0588-5595
Kazushi Sakamoto https://orcid.org/0000-0001-5187-2288
Mark Heyer https://orcid.org/0000-0002-3871-010X
Amanda M Lee https://orcid.org/0000-0001-8254-6768
Fumiya Maeda https://orcid.org/0000-0002-8868-1255
Samuel Boissier https://orcid.org/0000-0002-9091-2366
Daniela Calzetti https://orcid.org/0000-0002-5189-8004
Bruce G. Elmegreen https://orcid.org/0000-0002-1723-6330
Nanase Harada https://orcid.org/0000-0002-6824-6627
Luis C. Ho https://orcid.org/0000-0001-6947-5846
Masato I. N. Kobayashi https://orcid.org/0000-0003-3990-1204
Nario Kuno https://orcid.org/0000-0002-1234-8229
Barry F. Madore https://orcid.org/0000-0002-1576-1676
Sergio Martín https://orcid.org/0000-0001-9281-2919
Jennifer Donovan Meyer https://orcid.org/0000-0002-3106-7676
Kazuyuki Muraoka https://orcid.org/0000-0002-3373-6538
Yoshimasa Watanabe https://orcid.org/0000-0002-9668-3592

References

Adamo, A., Kruijssen, J. M. D., Bastian, N., Silva-Villa, E., & Ryon, J. 2015, MNRAS, 452, 246

Arimoto, N., Sofue, Y., & Tsujimoto, T. 1996, PASJ, 48, 275

Ballesteros-Paredes, J., Hartmann, L. W., Vazquez-Semadeni, E., Heitsch, F., & Zamora-Avilés, M. A. 2011, MNRAS, 411, 65

Ballesteros-Paredes, J., Vázquez-Semadeni, E., Palau, A., et al. 2018, MNRAS, 479, 2112

Bertoldi, F., & McKee, C. F. 1992, ApJ, 395, 140

Bolatto, A. D., Leroy, A. K., Rosolowsky, E., et al. 2008, ApJ, 686, 948

Bolatto, A. D., Wolfire, M., & Leroy, A. K. 2013, ARA&A, 51, 207

Bresolin, F., Kudritzki, R.-P., Urbaneja, M. A., et al. 2016, ApJ, 830, 64

Caldú-Primo, A., & Schruba, A. 2016, AJ, 151, 34

Caldú-Primo, A., Schruba, A., Walter, F., et al. 2013, AJ, 146, 150

Chevance, M., Krumholz, M. R., McLeod, A. F., et al. 2023, in ASP Conf. Ser. 534, Protostars and Planets VII, ed. S. Inutsuka et al. (San Francisco, CA: ASP), 1

Colombo, D., Hughes, A., Schinnerer, E., et al. 2014, ApJ, 784, 3

Colombo, D., Rosolowsky, E., Duarte-Cabral, A., et al. 2019, MNRAS, 483, 4291

Combes, F., & Becquaert, J.-F. 1997, A&A, 326, 554

Crosthwaite, L. P., Turner, J. L., Buchholz, L., Ho, P. T. P., & Martin, R. N. 2002, AJ, 123, 1892

Dame, T. M., Hartmann, D., & Thaddeus, P. 2001, ApJ, 547, 792

Dobbs, C. L., Burkert, A., & Pringle, J. E. 2011, MNRAS, 413, 2935

Dobbs, C. L., & Pringle, J. E. 2013, MNRAS, 432, 653

Donovan Meyer, J., Koda, J., Momose, R., et al. 2013, ApJ, 772, 107

Elmegreen, B. G. 1989, ApJ, 338, 178

Elmegreen, B. G., & Elmegreen, D. M. 1987, ApJ, 320, 182

Engargiola, G., Plambeck, R. L., Rosolowsky, E., et al. 2003, ApJS, 149, 343

Evans, N. J., Heyer, M., Miville-Deschênes, M.-A., et al. 2021, ApJ, 920, 126

Field, G. B., Blackman, E. G., & Keto, E. R. 2011, MNRAS, 416, 710

Foreman-Mackey, D., Hogg, D. W., Lang, D., et al. 2013, PASP, 125, 306

Freeman, P., Rosolowsky, E., Kruijssen, J. M. D., Bastian, N., & Adamo, A. 2017, MNRAS, 468, 1769

Fukui, Y., Kawamura, A., Minamidani, T., et al. 2008, ApJS, 178, 56

Goldsmith, P. F., Heyer, M., Narayanan, G., et al. 2008, ApJ, 680, 428

Hernandez, S., Larsen, S., Aloisi, A., et al. 2019, ApJ, 872, 116

Heyer, M., & Dame, T. M. 2015, ARA&A, 53, 583

Heyer, M., Krawczyk, C., Duval, J., & Jackson, J. M. 2009, ApJ, 699, 1092

Heyer, M. H., Carpenter, J. M., & Snell, R. L. 2001, ApJ, 551, 852

Hirota, A., Egusa, F., Baba, J., et al. 2018, PASJ, 70, 73

Hirota, A., Kuno, N., Baba, J., et al. 2014, PASJ, 66, 46

Hughes, A., Meidt, S. E., Colombo, D., et al. 2013, ApJ, 779, 46

Hunter, J. D. 2007, CSE, 9, 90

Inutsuka, S.-i., Inoue, T., Iwasaki, K., & Hosokawa, T. 2015, A&A, 580, A49

Jarrett, T. H., Chester, T., Cutri, R., Schneider, S. E., & Huchra, J. P. 2003, AJ, 125, 525

Kauffmann, J., Pillai, T., Shetty, R., et al. 2010, ApJ, 716, 433

Kobayashi, M. I. N., Inutsuka, S.-i., Kobayashi, H., & Hasegawa, K. 2017, ApJ, 836, 175

Koda, J., Hirota, A., Egusa, F., et al. 2023, ApJ, 949, 108K

Koda, J., Scoville, N., Sawada, T., et al. 2009, ApJL, 700, L132

Koda, J., Teuben, P., Sawada, T., et al. 2019, PASP, 131, 054505

Kruijssen, J. M. D. 2014, CQGra, 31, 244006

Lada, C. J., & Dame, T. M. 2020, ApJ, 898, 3

Lada, C. J., Lombardi, M., & Alves, J. F. 2010, ApJ, 724, 687

Larson, R. B. 1981, MNRAS, 194, 809

Lee, A. M., Koda, J., Hirota, A., et al. 2024, ApJ, 968, 97L

Leroy, A. K., Bolatto, A. D., Ostriker, E. C., et al. 2015, ApJ, 801, 25

Lombardi, M., Alves, J., & Lada, C. J. 2010, A&A, 519, L7

Maeda, F., Ohta, K., Fujimoto, Y., & Habe, A. 2020, MNRAS, 493, 5045

Mao, S. A., Ostriker, E. C., & Kim, C.-G. 2020, ApJ, 898, 52

Miville-Deschênes, M.-A., Murray, N., & Lee, E. J. 2017, ApJ, 834, 57

Mogotsi, K. M., de Blok, W. J. G., Caldú-Primo, A., et al. 2016, AJ, 151, 15

Muraoka, K., Konishi, A., Tokuda, K., et al. 2023, ApJ, 953, 164

Nakanishi, H., & Sofue, Y. 2016, PASJ, 68, 5

Oka, T., Hasegawa, T., Sato, F., et al. 2001, ApJ, 562, 348

Ramírez-Galeano, L., Ballesteros-Paredes, J., Smith, R. J., Camacho, V., & Zamora-Aviles, M. 2022, MNRAS, 515, 2822

Rand, R. J., Lord, S. D., & Higdon, J. L. 1999, ApJ, 513, 720

Rice, T. S., Goodman, A. A., Bergin, E. A., et al. 2016, ApJ, 822, 52

Robitaille, T., & Bressert, E., 2012 APLpy, Astrophysics Source Code Library, ascl:1208.017

Robitaille, T., 2019 APLpy v2.0: The Astronomical Plotting Library in Python v2.0, Zenodo, doi:10.5281/zenodo.2567476

Robitaille, T., Rice, T., Beaumont, C., et al., 2019 astrodendro, Astrophysics Source Code Library, ascl:1907.016

Roman-Duval, J., Jackson, J. M., Heyer, M., et al. 2010, ApJ, 723, 492

Rosolowsky, E. 2005, PASP, 117, 1403

Rosolowsky, E., & Blitz, L. 2005, ApJ, 623, 826

Rosolowsky, E., Hughes, A., Leroy, A. K., et al. 2021, MNRAS, 502, 1218

Rosolowsky, E., & Leroy, A. 2006, PASP, 118, 590

Sanders, D. B., Scoville, N. Z., & Solomon, P. M. 1985, ApJ, 289, 373

Sault, R. J., Teuben, P. J., & Wright, M. C. H. 1995, ASP Conf. Ser. 77, Astronomical Data Analysis Software and Systems IV, ed. R. A. Shaw, H. E. Payne, & J. J. E. Hayes, (CA, San Francisco: ASP), 433

Scoville, N. Z., & Sanders, D. B. 1987, in Interstellar Processes, ed. D. J. Hollenbach & H. A. Thronson (Dordrecht: Reidel), 21

Smith, R. J., Treß, R. G., & Sormani, M. C. 2020, MNRAS, 492, 1594

Solomon, P. M., Rivolo, A. R., Barrett, J., & Yahil, A. 1987, ApJ, 319, 730

Stark, A. A. 1984, ApJ, 281, 624

Stark, A. A., & Lee, Y. 2005, ApJL, 619, L159

Sun, J., Leroy, A. K., Ostriker, E. C., et al. 2020a, ApJ, 892, 148

Sun, J., Leroy, A. K., Schinnerer, E., et al. 2020b, ApJL, 901, L8

Thim, F., Tammann, G. A., Saha, A., et al. 2003, ApJ, 590, 256

Tilanus, R. P. J., & Allen, R. J. 1993, A&A, 274, 707

van der Walt, S., Schönberger, J. L., Nunez-Iglesias, J., et al. 2014, PeerJ, 2, e453

Verschuur, G. L. 1993, AJ, 106, 2580

Williams, J. P., & McKee, C. F. 1997, ApJ, 476, 166

Wilson, C. D. 1995, ApJL, 448, L97

Wilson, C. D., Warren, B. E., Irwin, J., et al. 2011, MNRAS, 410, 1409